Modeling and Analysis of High-Speed Mobile Robots Operating on Rough Terrain

by

Dariusz Golda

B.S. with Honors, Mechanical Engineering
Rutgers, The State University of New Jersey, 2001

Submitted to the Department of Mechanical Engineering
in Partial Fulfillment of the Requirements for the Degree of
Master of Science in Mechanical Engineering

at the

Massachusetts Institute of Technology

June 2003

Signature of Author..
Department of Mechanical Engineering
May 12, 2003

Certified by.......................................
Steven Dubowsky
Professor of Mechanical Engineering
Thesis Supervisor

Accepted by..
Ain A. Sonin
Chairman, Department Committee on Graduate Students

Modeling and Analysis of High-Speed Mobile Robots Operating on Rough Terrain

by

Dariusz Golda

Submitted to the Department of Mechanical Engineering
on May 12, 2003 in Partial Fulfillment of the
Requirements for the Degree of
Master of Science in Mechanical Engineering

ABSTRACT

A fundamental problem associated with mobile robots is planning and control while moving at high speeds over rough, unstructured terrain. Given a desired path through rough terrain, a robotic vehicle should be able to autonomously traverse the path at maximum dynamically-feasible speeds. Wheel slip and ballistic motion should be considered to attain the desired speeds, resulting in very complex dynamics. The robot should also have the capacity to quickly detect and handle unforeseen situations through intelligent actions. At high speeds, this ability is crucial because of limited sensor information. Uncertainty in vehicle and terrain properties makes it difficult to implement safe, intelligent control actions.

An important part of control and planning is model-based analysis. Model-based analysis enables the prediction of robot performance. This thesis develops an approach to modeling high speed mobile robots in rough terrain, as well as an analysis of sensitivity to several dynamic parameters. The modeling approach considers complex dynamics and system uncertainty to develop a comprehensive description of mobile robot motion in rough terrain.

The first part of the thesis develops a high-order system model of mobile robots operating in rough terrain. The model is implemented in simulation and validated with an experimental system. The validation methodology and results are discussed.

The second part of this thesis presents an initial simulation-based investigation of the system parameter sensitivity and model prediction uncertainty of high-speed motion of mobile robots operating in rough terrain. The analysis methods and results are discussed.

Thesis Supervisor: Steven Dubowsky
Title: Professor of Mechanical Engineering

ACKNOWLEDGEMENTS

I'd like to thank all those who have helped and supported me through the course of my master's thesis research. My utmost gratitude goes to Professor Dubowsky, for his gracious support of my research and his first-class advising. In addition, thanks to DARPA and TACOM for providing the support for this project.

Thanks to Dr. Karl Iagnemma for his help, guidance, wisdom, and patience on the high-speed mobile robot project. I am also grateful all my colleagues in the Field and Space Robot for their outstanding support and kindness – they are truly the strength of the lab. Large thanks to Matthew Spenko, who has suffered through my barrage of questions and worked closely with me throughout the project.

I'd like to pay special thanks to my family and friends for being there along each step of this journey. Without them, none of this would be possible. Thank you to my Mom, Dad, Jeff, and my wonderful girlfriend Renata.

CONTENTS

FIGURES

TABLES

CHAPTER 1

INTRODUCTION

1.1 Introduction

This thesis presents an approach to modeling and analysis of high-speed mobile robots operating in rough terrain. The work serves as a foundation for developing autonomous control and planning algorithms for these vehicles. It embodies the author's contribution to an ongoing research program at the MIT Field and Space Robotics Laboratory. The program is jointly funded by the Defense Advanced Research Projects Agency (DARPA) and the US Army Tank-Automotive and Armaments Command (TACOM). The DARPA focus is to sponsor "revolutionary, high-payoff research that bridges the gap between fundamental discoveries and their military use" [DARPA, 2003]. TACOM's focus is to provide "ground combat, automotive, marine, and armaments technologies and systems, and to generate, provide and sustain mobility, lethality, and survivability" [TACOM, 2003]. The MIT research program fits squarely within both frameworks, contributing to the fundamental problems of modeling, control, and planning, and to the practical problem of developing an autonomous military ground vehicle system.

A fundamental problem associated with mobile robots is planning and control while moving at high speeds over rough, unstructured terrain (see Figure 1.1). Given a desired path through rough terrain, a robotic vehicle should be able to autonomously traverse the path at maximum dynamically-feasible speeds. Wheel slip and ballistic motion should be considered to attain the desired speeds, resulting in complex dynamics. One control method might be to quickly detect and handle unforeseen situations through an intelligent reaction scheme. At high speeds, this ability is crucial because of limited sensor information. Uncertainty in vehicle and terrain properties makes it difficult to implement safe, intelligent reactive behaviors

A physics-based control and planning strategy would consider information uncertainty, and slip and ballistic motion at high speeds. In a physics-based strategy, the system has knowledge of its dynamics through a physics-based model. Vehicle and terrain models would be used to predict robot motion offline, and the results would be employed in a fast, online reactive control scheme.

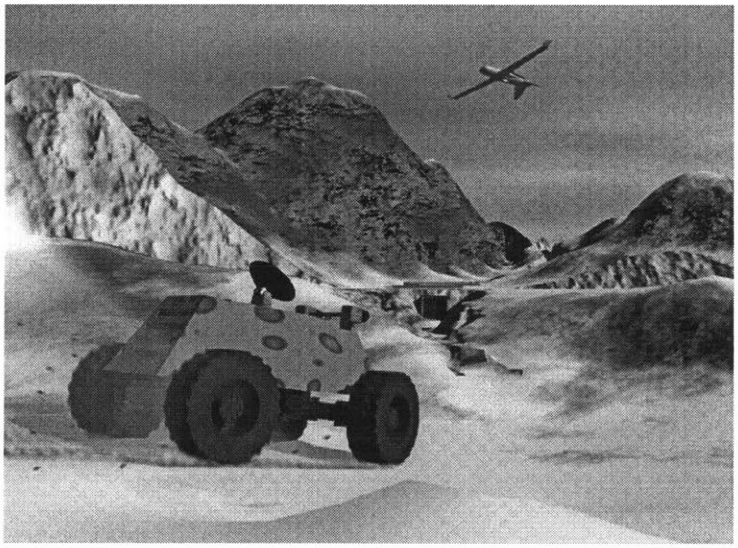

Figure 1.1. Image of a high-speed rough-terrain mobile robot.

Model-based analysis could play an important role in control and planning. It enables the prediction of robot performance. The goal of this thesis is to present an approach to modeling high speed mobile robots in rough terrain, as well as an analysis of sensitivity to several dynamic parameters. The modeling approach considers complex dynamics and system uncertainty to develop a comprehensive description of mobile robot motion in rough terrain.

1.2 Motivation

Mobile robots can perform difficult tasks in hostile environments, and are therefore becoming increasingly important in a variety of fields. Exploration, mining, forestry, and hazardous site inspection are a few applications of mobile robot systems [Cunningham, et al, 1998; Golombek, 1998; Gonthier, et al, 1998; Osborn, 1989]. In addition to civilian applications, mobile robots, or autonomous ground vehicles (AGVs), are becoming extremely important in military applications [Eicker, 2001; Gerhart, et al, 1999]. Potential missions include logistics, surveillance, fire missions, and soldier assistance. In order to operate effectively in the field, mobile robots must be able to traverse rough unstructured terrain (see Figure 1.2).

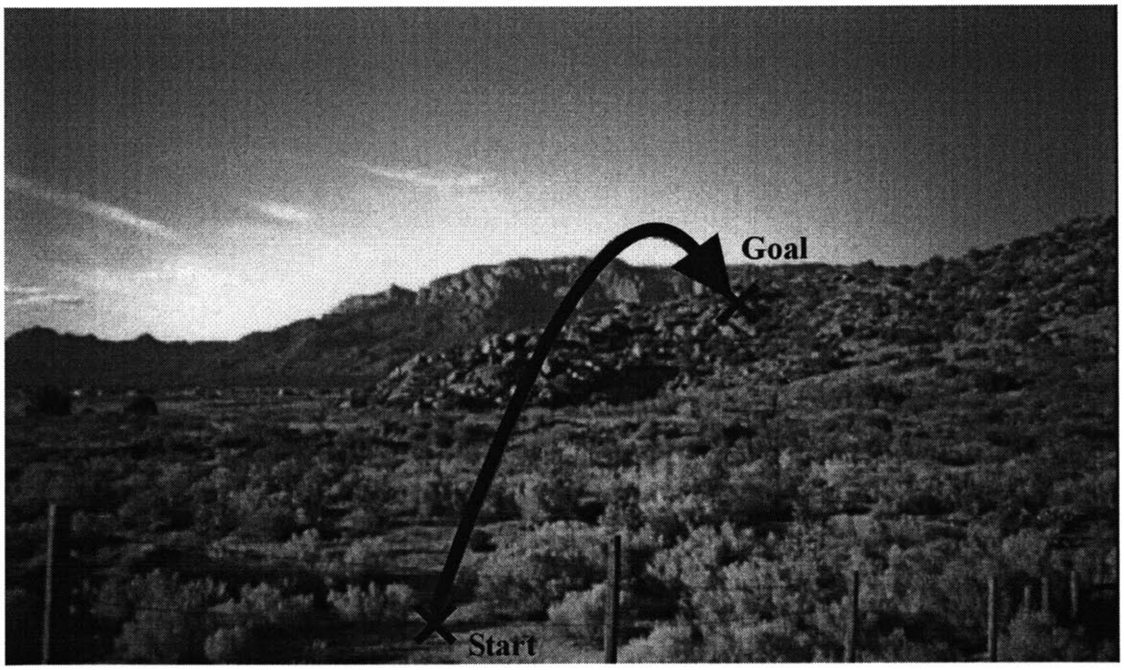

Figure 1.2. Typical military AGV mission environment (Eicker, 2001).

Current autonomous ground vehicle technology is limited to relatively slow speeds on rough terrain. Rough terrain is defined here as containing spatial frequencies less than the wheelbase of the vehicle. On the other hand, smooth terrain has spatial frequencies much greater than the wheelbase of the vehicle. Autonomous high speed motion has been achieved on hard, smooth surfaces such as pavement [Peng, et al, 1993]. Fully-autonomous motion at moderate speeds on moderately rough terrain was demonstrated by the Demo III vehicle, which is depicted in Figure 1.3 [Shoemaker, et al, 2000].

Figure 1.3. Testing of the Demo III UGV (National Institute of Standards and Technology, 2003).

In many military missions, it would be desirable for the mobile robot to move quickly through rough terrain [Gerhart, et al, 1999]. High speed motion would reduce the chance of detection and targeting during missions, and would decrease overall mission time. In addition, it could allow the mobile robot to travel longer distances, which is also advantageous for exploration missions. Algorithms for autonomous planning and control would free users from the burden of supervisory control, allowing them to focus on more important or difficult tasks.

Substantial work has been done in the control of high speed robotic vehicles on nearly flat terrain [Ben Amar, 1997; Desantis, 1995; Peng, et al, 1993; Pham, et al, 1996]. However, the modeling and control simplifications made are not valid in rough terrain. Researchers have also investigated control of mobile robots in rough terrain at moderate speeds [Kelly, et al, 1997; Langer, et al, 1994; Olin, et al 1991]. This body of work assumes that no wheel slip and no loss of ground contact, which is not true in general at high speeds. In summary, few researchers have studied the modeling, analysis, and control of high-speed, rough-terrain robotic vehicles.

The direction taken in this research program is to develop robust, physics-based control and planning algorithms for real-time navigation of high-speed mobile robots operating in rough terrain. These algorithms would accommodate wheel slip and ballistic motion of the mobile robot. At high speeds, the performance of rough-terrain mobile robots is heavily dependent on the system dynamics and terrain interactions. The algorithms will therefore consider vehicle and terrain models. In addition, it will consider model uncertainty, and the uncertainty in sensory information. A schematic of a multi-layered approach is presented in Figure 1.4.

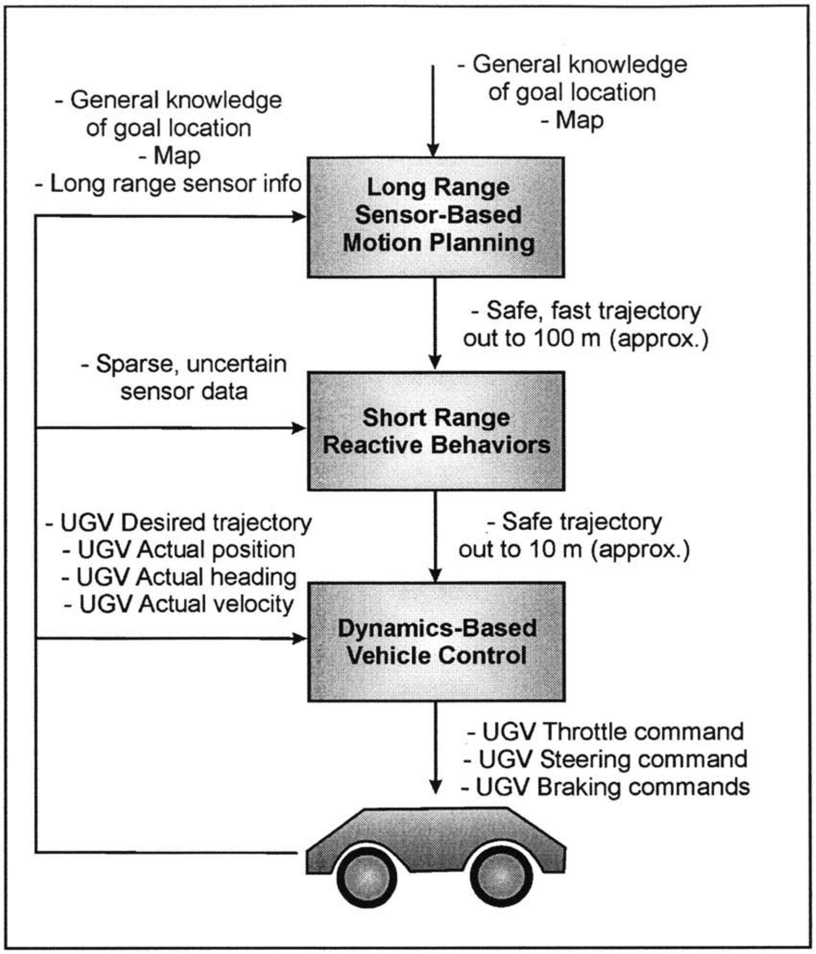

Figure 1.4. Schematic of the multi-layered control architecture (Spenko, 2003).

The control scheme is composed of three layers: 1) a high-level, long range motion planning layer, 2) a mid-level reactive behavior layer, 3) and a low level vehicle control layer. The three layers work together to form a unified motion planning and control scheme for high speed mobile robot navigation through rough terrain [Spenko, 2003].

The high-level motion planning layer plans a safe and dynamically feasible high-speed path toward a destination point through a given terrain. Inputs to this layer include a goal location, vehicle and terrain model, digital elevation map, and long-range sensor information. The output from this layer is a safe, dynamically feasible, high-speed trajectory "band." The variable trajectory band thickness will be defined by the model and sensor uncertainty. Therefore, it is desirable to quantify the uncertainty in system response as a function of uncertainty in the system model. This thesis addresses this issue.

A mid-level reactive control layer will quickly choose an emergency maneuver, or reactive behavior, to avoid short-range obstacles and circumstances not accounted for in high-level motion planning [Iagnemma, et al, 2002]. The primary goal of this layer is to maintain safety of the mobile robot despite terrain, vehicle, and motion uncertainty. The input to this layer is sparse, short-range sensor data. A safe, short-range trajectory is the output from this control layer. Reactive behavior selection algorithms will be developed from extensive off-line modeling techniques. These techniques are the focus of this thesis. The vehicle model, including uncertainty, will be used to generate safe and feasible reactive behaviors.

Path-following control is implemented in the lowest-level layer of the control scheme. The purpose of this layer is to control the robot motion along the desired trajectory, as prescribed by the two higher layers. Inputs of this layer include the vehicle state and the current desired trajectory. The layer outputs commands to the robot's actuators, such as the steering and throttle servos. The control techniques used in this layer will incorporate a system model, albeit simplified.

This thesis focuses on modeling. The work forms the basis for development of robust control and planning algorithms described above. The modeling approach considers complex dynamics, tire interactions, slip, and ballistic motion, and system uncertainty. In addition to model analysis for control and planning, it would be desirable to quantify the sensitivity of the system responses to errors in parameter estimates. A ranking of the sensitivity of dynamic model parameters would enable a user to appropriately focus modeling effort, so as to minimize expected uncertainty in the predicted system response. Such results would be useful in studying the modeling or model-based control of vehicles operating at high speeds in rough terrain.

1.3 Background and Literature Review

Dynamic vehicle modeling has been studied for many years. Varying levels of modeling detail have been examined, from simple mass-spring-damper systems to high degree-of-freedom passenger automobiles on nearly smooth roads with complex tire-terrain interactions. However, complex vehicle models incorporating uneven terrain, out of plane and ballistic motion, and wheel slip have not been examined. It has been shown that highly-detailed models can accurately predict the dynamics of mobile robots operating at high speeds in rough terrain [Iagnemma, et al, 2002], and improve the performance of AGV navigation systems [Julier, et al, 2003]. The following sections provide a review of the literature relevant to the modeling of ground vehicles, tire-terrain interaction, and terrain geometry.

1.3.1 Wheeled-Vehicle Models

Several dynamic lumped-parameter vehicle models have been studied. The most basic and earliest model is known as the quarter-car model, a schematic of which is presented in Figure 1.5 [Gillespie, 1992].

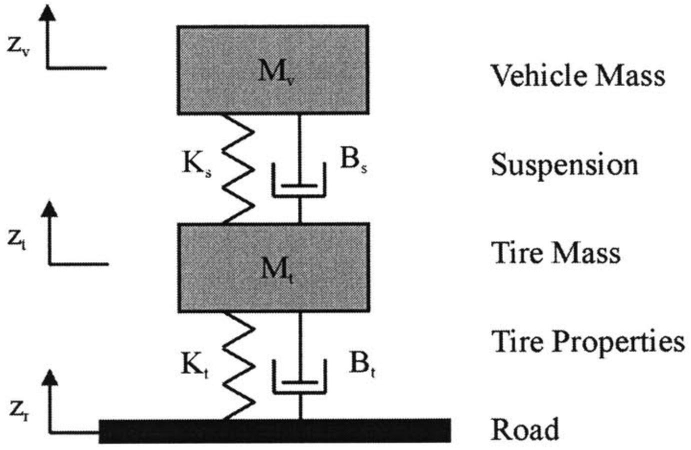

Figure 1.5. Schematic of the quarter-car model.

The planar, two-degree-of-freedom (DOF) quarter-car model represents the vehicle chassis as a sprung mass affixed to a spring-damper representing the suspension of all four wheels. The wheels are lumped together as a single mass sprung by the cumulative tire stiffness and damping. Both body and tire masses are constrained to move vertically. Ground forces due to tire-terrain interactions are neglected and replaced by kinematic rolling, and the terrain geometry is modeled as a vertical displacement input to the system. This model grossly approximates the vertical dynamics of a four-wheeled vehicle, neglecting any in-plane angular motion of the vehicle and all out-of-plane motion. This model has been recently used for developing active suspension control systems [Chalasani, 1986; Fischer, et al, 2000; Gordon, et al, 1998; Mucka, 2000;

Sloyom, et al, 2002]. An extension of the simple model has been implemented for slow-speed control of mobile robotic vehicles operating in a flat, obstacle-laden terrain [Talukder, et al, 2002]. In that work, the vehicle-suspension model is combined with a compliant obstacle model to yield an estimate of the maximum safe traversable velocity. An advantage of the quarter-car model is that a closed form solution exists and is well documented [Shabana, 1996].

A more complex four DOF model has been developed that describes both vertical and angular in-plane motion. Known as the half-car model, it consists of a vehicle body mass sprung by independent suspension and tire sets. The front and rear suspension and tire properties are lumped separately. Figure 1.6 shows a schematic diagram of the model.

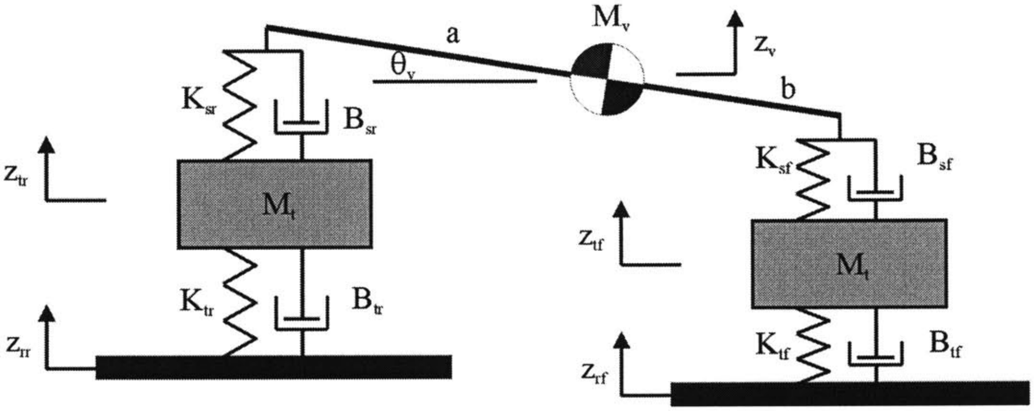

Figure 1.6. Schematic of the half-car model.

The half-car model has been used recently in active suspensions system design and analysis, with the ability to study heave and pitch of the vehicle [Campos, et al, 1999]. Restrictions of this model include the assumption of in-plane motion, small angle approximations, and kinematic rolling with no slip. A more advanced, nine DOF half-car model was developed for planar motion of mobile robots in uneven terrain that incorporates tire-terrain friction forces [Rzepniewski, 2001]. Used for motion planning of high speed rough terrain vehicles, the model ignores out-of-plane motion and assumes point contact and simple tractive friction forces. Its utility in predicting general motion of high speed mobile robots with complex tire-terrain interactions is therefore limited.

The progression from half-car to a full-car vehicle model is natural, yet complex. Full-car models limited to small angle approximations that assume kinematic wheel rolling have been developed for the analysis and control of active suspensions [Chalasani, 1986; Elbeheiry, et al, 1996; and Ikenaga, et al, 2000]. The kinematic rolling constraint limits the vehicle motion to a straight path, since lateral ground forces are required for steering. A schematic of the full-car model is presented in Figure 1.7.

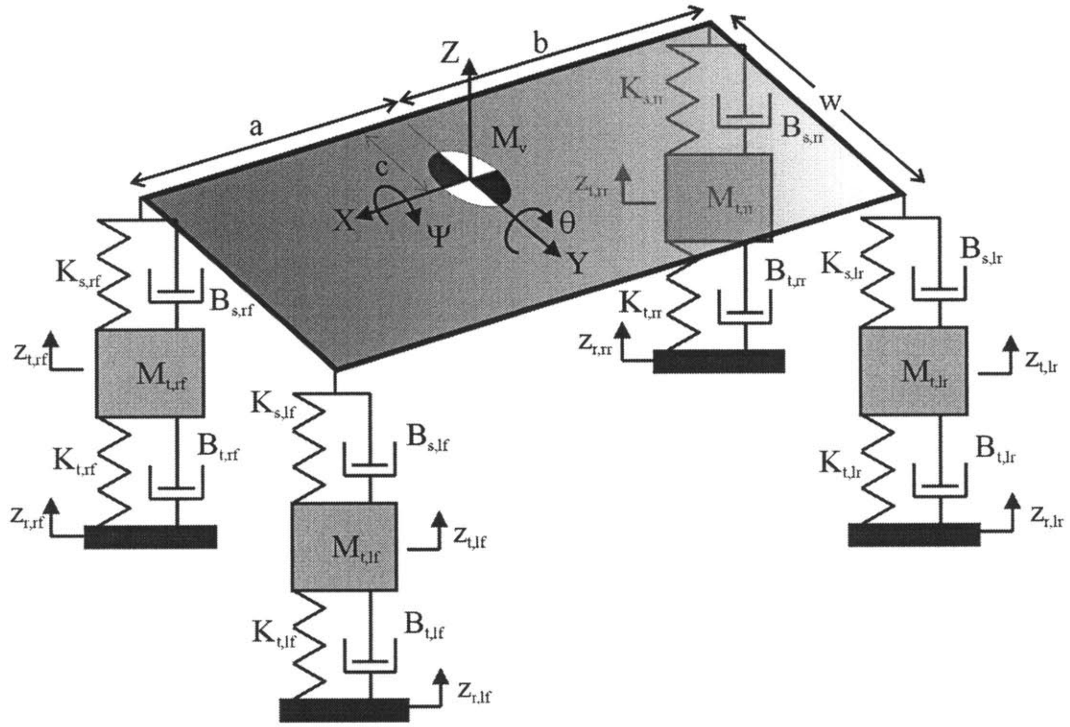

Figure 1.7. Schematic of the full-car model.

Although this is the most sophisticated vehicle model to date, it suffers in generality from the small angle approximation and kinematic rolling constraints. The small angle assumption is generally invalid for high-speed motion of mobile robots on uneven surfaces. In addition, wheel slip commonly occurs during high-speed motion, warranting the use of tire-terrain interaction models. Finally, none of these models allow ballistic motion.

Many researchers have used simplified models to study vehicle turning, the most common of which is the bicycle model [Gillespie, 1992]. The schematic of this model is shown in Figure 1.8.

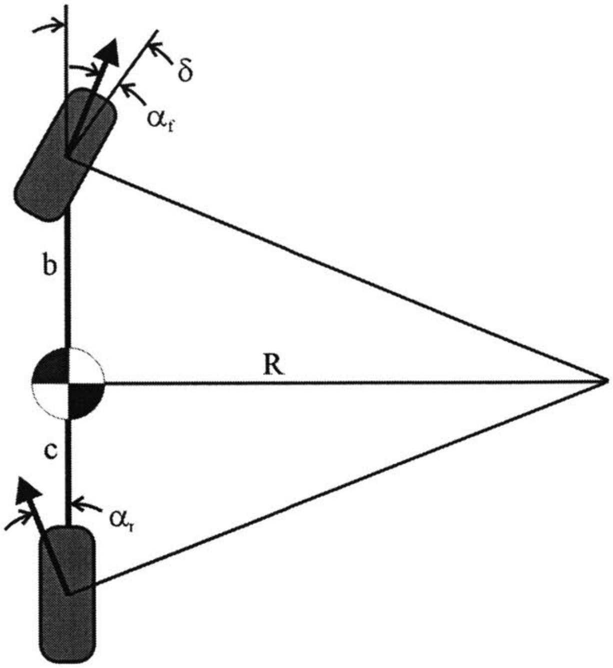

Figure 1.8. Schematic of the bicycle cornering model.

For large turn radii, the difference in steer angle of the front wheels is negligible, and thus the two front wheels are represented by one wheel. The same assumption is made for the rear wheels. In this model, wheel slip is ignored. This model assumes smooth surfaces, and does not consider wheel or suspension compliancy, vertical motion, or pitch and roll dynamics. The vehicle can be considered a point mass moving on a semi-planar surface subject to kinematic constraints.

Although simple, the bicycle model has been used to develop motion planning algorithms for autonomous ground vehicles [Shiller, et al, 1991]. Lateral vehicle control schemes were developed for smooth terrain using this model [Peng, et al, 1993, Pham, et al 1996]. It has also been implemented successfully in large-scale outdoor vehicles operating on smooth surfaces [Durrant-Whyte, 1996]. An extension of the bicycle model with slip and tire forces was used for controlling handling stability directly from the tire tractive forces [Shino, et al, 2000]. A similar bicycle model that considers slip as an estimated state has been adopted for modeling the motion of mining equipment [Scheding, et al, 1999]. In addition to modeling and control, researchers have recently studied the role of the bicycle model and its impact on performance of autonomous navigation systems [Julier, et al, 2003]. The results indicate that higher-order models can lead to substantial improvements in navigation performance.

It should be noted that all the models presented thus far, with the exceptions of [Rzepniewski, 2001], assume continuous ground contact of the tires. Hard turning and ballistic motion at high speeds during obstacle traversal are not captured by these models. A general model that considers motion in three dimensions, as well as suspension, slip, tire forces, and ballistic motion is necessary to adequately represent the dynamics of high-speed motion of mobile robots in rough terrain.

1.3.2 Tire-Terrain Interaction Models

Tire-ground interaction models can be grouped into four categories: a) rigid ground and deformable tire, b) deformable ground and rigid tire, c) deformable ground and deformable tire, and d) rigid ground and rigid tire. Rigid ground – deformable tire models have been studied for several years, originally for passenger automobiles and trucks operating on paved roads. Originally introduced in 1987, the Magic Formula tire model (MF-Tire) is one of the most widely used of these formulations [Bakker, et al, 1987]. This early version used trigonometric functions to describe slip conditions. For a recent version of the MF-tire model, refer to [Pacejka, 1996]. Two revised versions of the MF-tire were also introduced. One version, called the MF-MCTire, was developed to handle large wheel camber angles in maneuvers such as rollover [De Vries, 1997]. Another form known as the SWIFT-Tire Model combines the MF-tire slip model with a rigid ring model of the wheel, handling tire excitation frequencies up to 120 Hz [Maurice, 1999; Zegelaar, 1998].

In addition to rigid-terrain, compliant tire models, researchers have investigated the interaction of rigid wheels in deformable terrain [Wong, et al, 1967]. This mode of tire interaction is suitable for rigid-wheel mobile robots such as planetary rovers operating in soft sand or soil. It would also be suited for high speed vehicles with pneumatic tires that are firm relative to the soil. Depending on terrain conditions, a model describing the dynamic interaction between compliant tires and rigid terrain or compliant tires and compliant terrain would be most appropriate. The case selected for this study

1.3.3 Geometric Terrain Models

The control and planning algorithm proposed in Section 1.2 will need to make use of a sparse digital elevation map of natural terrain. The sparse data is interpolated to create a dense map suitable for use in the algorithm. Several methods for modeling natural terrain have been proposed, the simplest of which uses smooth three-dimensional B-spline patches [Mortenson, 1985]. This method is suitable for modeling smooth, curved surfaces, such as grassy rolling hills. It has been implemented for dynamic motion planning of autonomous ground vehicles [Shiller, et al, 1991].

Another technique for modeling naturally occurring terrain employs fractal geometry. Fractal techniques were selected to model natural-type terrain in this work because they apply to a range of terrain types. Fractals were originally proposed as a family of mathematical functions for describing natural phenomena such as coastlines [Mandelbrot, 1977]. An artificial coastline with fractal geometry is shown in Figure 1.9.

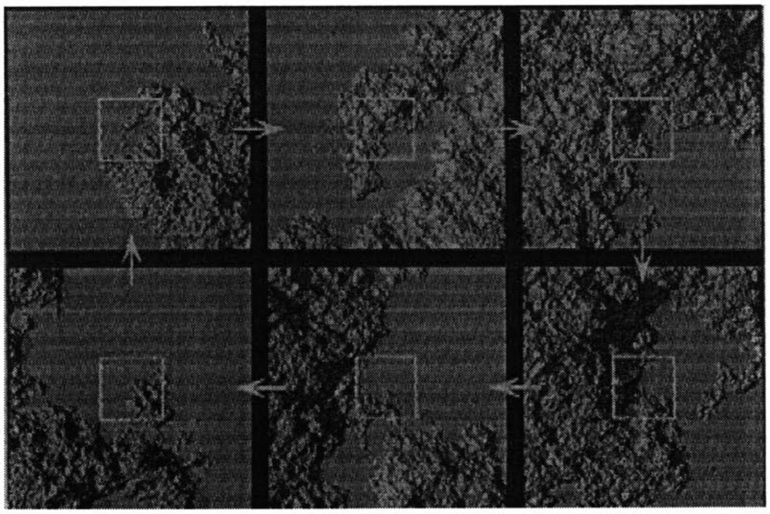

Figure 1.9. Self-similarity of an artificial fractal coastline (Voss, 1989).

Computer graphics researchers have applied fractal theory to generate natural objects such as trees, mountain ranges, and cloudy skies, with high levels of realism [Voss, 1985]. More recently, it has been shown that fractal modeling techniques could apply to a wide range of natural terrain profiles [Ohmiya, 1990]. In parallel, several researchers have developed methods for estimating the fractal dimension of natural terrain for reconstructive purposes [Arakawa, et al, 1991 and 1993; Keller, et al, 1987;

Pentland, 1984]. Natural terrain was then reconstructed from sparse data using fractal dimension estimates. For a review of several reconstruction methods, see [Arakawa, et al, 1993].

Researchers have also used wavelets to describe natural terrain for motion planning algorithms, but no evidence exists to suggest this method is more accurate than fractal methods [Pai, et al 1998]. In addition, stochastic techniques have been recently used represent three-dimensional unstructured surfaces and environments considering sensor uncertainty [Leal, et al, 2002].

1.4 Research Overview

The proposed planning and control algorithms for high-speed mobile robots operating in rough terrain would use detailed dynamic models of the vehicle, terrain, and tire-ground interactions. Although a large body of literature exists for various aspects of the modeling problem, a general model for high-speed motion of vehicles operating in rough terrain has not been studied. The goal of this research is to develop suitable, experimentally-validated models for such a dynamic system, and to investigate model sensitivity and the effect of uncertainty on high-speed motion prediction. It is desired to show that a high-speed mobile robot system can be modeled with sufficient accuracy. The sensitivity study could direct modelers and designers to efficiently place modeling effort in mobile robot systems. This study is limited to robotic vehicles with four wheels. The model is implemented in simulation using the ADAMS software package. This work seeks to form a fundamental basis for developing model-based control and planning schemes for high-speed mobile robots operating in rough terrain.

1.5 Thesis Outline

This thesis is divided into three main chapters: a description of a general high-speed mobile robot and terrain model (Chapter 2), experimental model validation (Chapter 3), and a sensitivity and uncertainty analysis (Chapter 4). Chapter 5 presents conclusions and suggestions for future work. The appendices present analytical and experimental details.

CHAPTER

2

HIGH SPEED MOBILE ROBOT MODEL

2.1 Introduction

A basic challenge in developing algorithms for planning and control of high speed mobile robots operating in rough terrain is to adequately model the system. The complexity of typical high-speed mobile robotic ground vehicles, and their interaction with natural, unstructured terrain, makes modeling of these systems inherently difficult. In addition, the system dynamics are fundamentally different than that of a mobile robot operating at slow speeds on rough terrain, which can often be solved in closed form. In general, the equations of motion of this problem are complex and nonlinear, and the systems cannot be solved analytically.

This chapter describes vehicle and terrain models developed for prediction and analysis of high-speed mobile robots operating in rough terrain. A high-order lumped-parameter vehicle model is presented that captures the dynamics of the system, and a tire-terrain interaction model for hard surfaces and compliant tires is described. In addition, a method for modeling natural terrain from sparse terrain data is discussed. These models can then be implemented in simulation for the purposes of motion prediction and analysis.

2.2 High Speed Mobile Robot Dynamic Model

A fifteen degree-of-freedom (DOF) model of a high-speed rough-terrain mobile robot was developed. In order to capture the dynamics of general high-speed motion in rough terrain, the high-order model considers vehicle roll, pitch, and yaw, suspension dynamics, tire dynamics, and ground forces. The model will be used for predicting and evaluating mobile robot dynamics. This model is a lumped parameter representation of the robot dynamics, including mass and inertial properties of the robot body and wheels, and compliance and damping of the suspension and tires. A schematic of the lumped-parameter model is presented in Figure 2.1 and Figure 2.2.

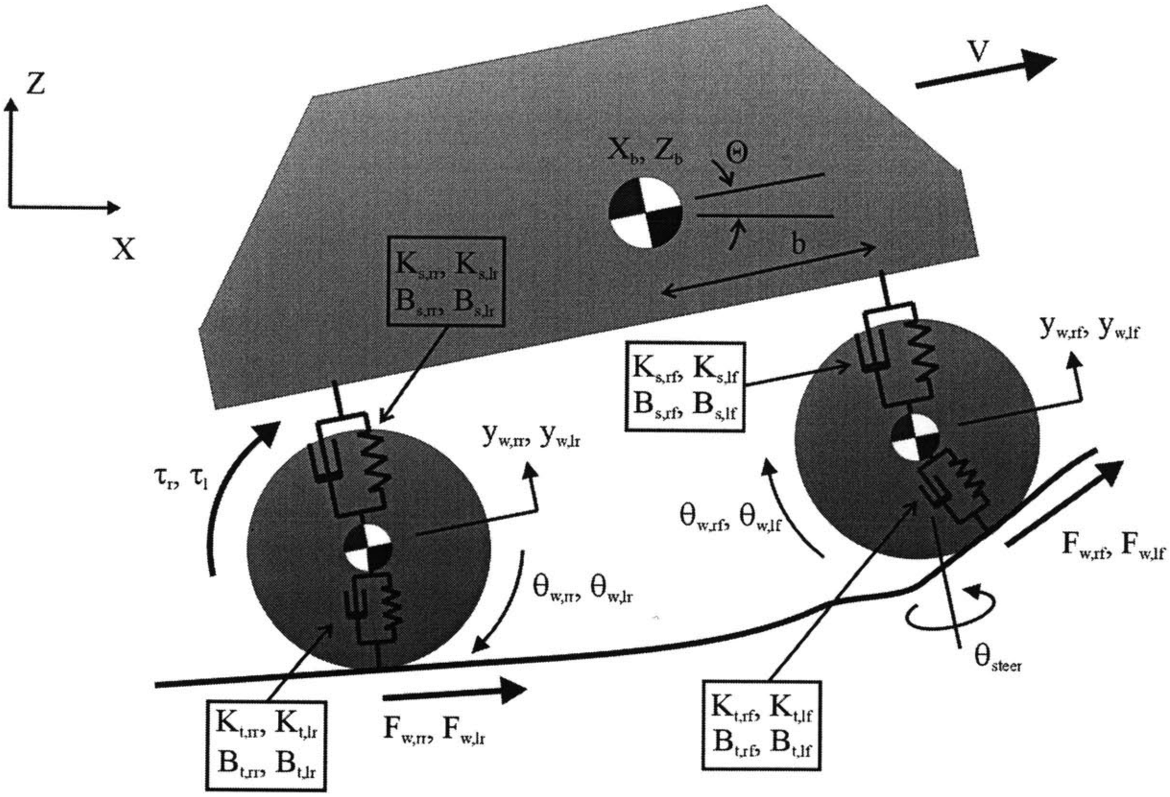

Figure 2.1. Schematic of the high-speed mobile-robot model (side view).

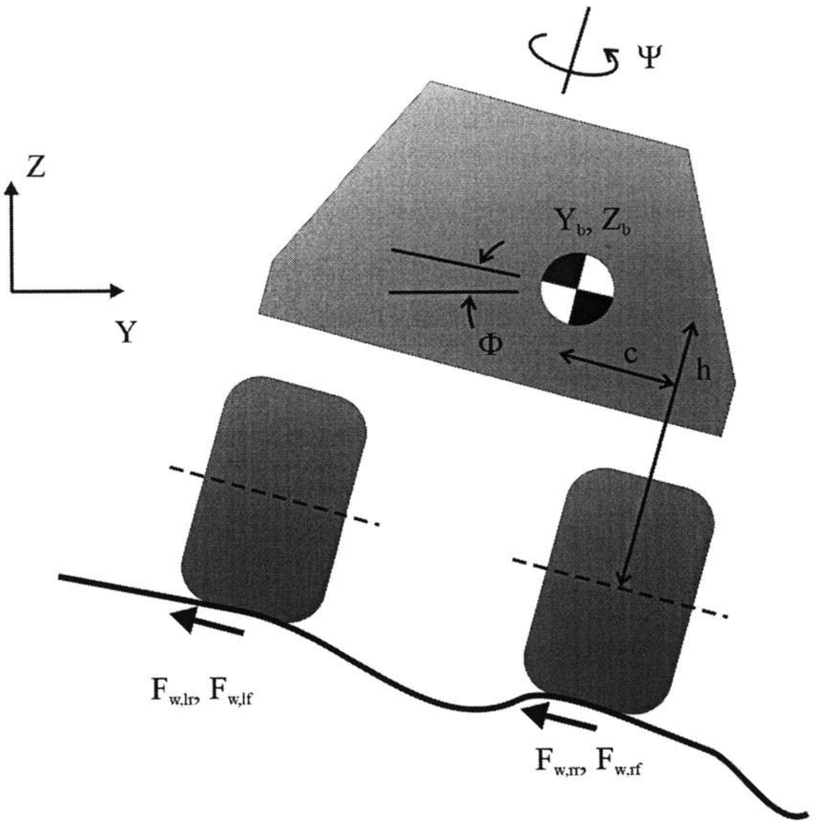

Figure 2.2. Schematic of the high-speed mobile-robot model (rear view).

Three translational and three rotational degrees-of-freedom are assigned to the robot body, which is a lumped mass at the point CG_b. The lumped body mass properties include all suspension components. The robot's wheels are mounted to the body through independent spring-damper suspensions. This is a general suspension representation. Unified or linked suspension assemblies can be modeled by adding appropriate kinematic constraints. Suspension spring and damper elements are assumed to be nonlinear functions of displacement and velocity, respectively.

Each of the four wheels has a rotational degree-of-freedom for rolling, and a translational degree-of-freedom for motion relative to the body along the suspension travel direction. Tire compliance and damping are modeled as a parallel nonlinear spring-damper acting normal to the local ground contact patch. Rolling resistance of the tires is neglected for simplicity. Tractive and braking ground forces generated by the tire are modeled using the Magic Formula tire model, as explained in Section 2.3.1.

The vehicle command inputs are the torque applied to the rear wheels, τ_r and τ_l, and the steering angle of the front wheels, θ_{steer}. Figure 2.1 shows the control inputs to the model. Although commands are modeled independently for each wheel, it is often the case in a real mobile robotic system to control torque to the rear wheels through a differential with a motor or engine. Heading is often controlled by setting the steering angle of the front wheels with a mechanism. The mechanism can kinematically constrain the steering wheels to enable geometries such as Ackerman steering [Gillespie, 1992].

2.3 Rigid Terrain Model

Typical high-speed rough-terrain robotic systems have pneumatic tires and operate on a wide range of surfaces. It is important to model both terrain geometry and ground forces generated by terrain-tire interaction. Because of the wide scope of terrain types, this thesis is limited to dry, hard terrain as in Figure 1.3. Fractal-based geometry has been shown to accurately depict some natural terrains (see Chapter 1). Also, rigid-terrain, flexible-tire models can represent the ground forces generated by such systems, including the system presented in Section 3.2.1. Both of these model types are employed in this work, as explained below.

2.3.1 Magic Formula Tire Model

The compliant tire, rigid-terrain interaction model used to compute ground forces in this work was first introduced in 1987 and is known as the Magic Formula Tire Model [Bakker, et al, 1987]. Several versions of this model have appeared over the years, a recent version of which is used here [Pacejka, 1996]. The Magic Formula (MF Tire) model was chosen for its accuracy and its capacity to handle zero and near-zero angular wheel velocities. Although the MF Tire was implemented here, any appropriate tire force model can be used.

The Magic Formula model computes the forces exerted on the tire by the ground as a function of the tire's mechanical properties, friction at the tire-road interface, road structure, and relative motion between the tire and the road, or tire slip. The MF Tire model computes the steady-state ground forces acting on the tire using semi-empirical mathematical formulas. The tire forces (F_x, F_y) and moments (M_x, M_y, M_z) due to ground interaction are computed using the longitudinal and lateral slip (κ, α), wheel camber (γ), and vertical tire force (F_z) as inputs. A block diagram of the model inputs and outputs is shown in Figure 2.3.

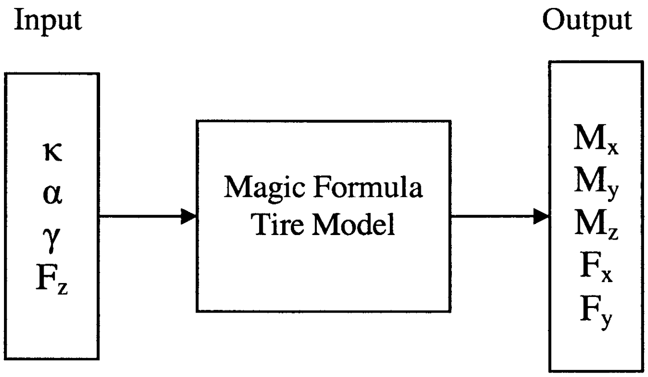

Figure 2.3. Block diagram of the Magic Formula tire model.

The MF-Tire model can compute the steady state and the transient dynamics of the tire up to 8 Hz. For the purposes of this work, the MF-tire tractive force parameters were taken to be those of an automobile tire. See [Pacejka, 1996] for more information regarding this tire model. The vertical stiffness and damping of the tires is modeled as a linear spring-damper.

2.3.2 Modeling Rough Terrain Geometry

In this work, a technique called the midpoint displacement method (MPD) is used to model the geometry of natural terrain over a regular grid. For details of this method, see [Mandelbrot, 1977]. Fractal-based terrain models interpolate between sparse data points using fractal geometry [Arakawa, et al, 1993]. The key feature of methods such as the MPD is that fractals are self similar at any length scale, and thus the grid spacing can be made arbitrarily small while preserving the basic geometric structure for some terrains. An example of terrain generated using the MPD technique is presented in Figure 2.4.

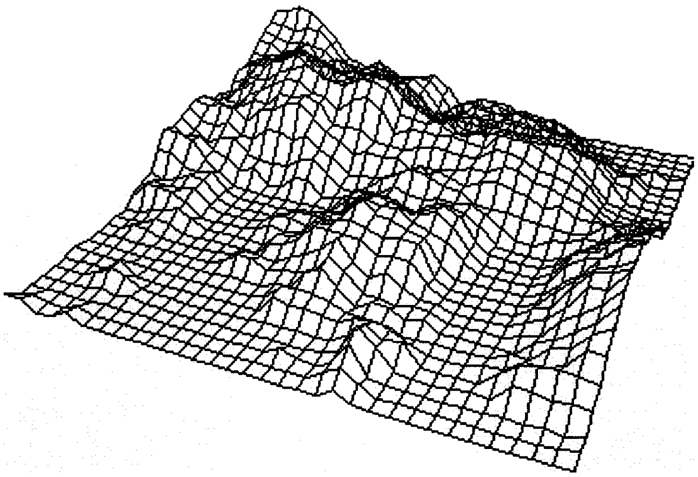

Figure 2.4. Example terrain using fractal MPD method.

The midpoint displacement method is a recursive interpolation technique. The method begins with a square grid of points with prescribed heights, as shown in Figure 2.5.

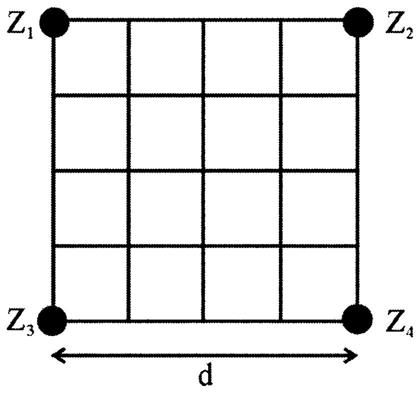

Figure 2.5. Initial midpoint displacement grid.

The height of the grid midpoint Z_m is computed by averaging the corner points and adding a scaled random number:

$$Z_m = \frac{1}{4}(Z_1 + Z_2 + Z_3 + Z_4) + X_n \tag{2.1}$$

The midpoint heights on the edges of the original grid are computed by averaging the four closest points, and adding random noise. During the first iteration, only the three closest points are used to compute the average. For example, the midpoint height between points 1 and 2 is

$$Z_{m,12} = \frac{1}{3}(Z_1 + Z_2 + Z_m) + X_n \tag{2.2}$$

Figure 2.6 shows these two steps. New points are black, while previously computed points are white.

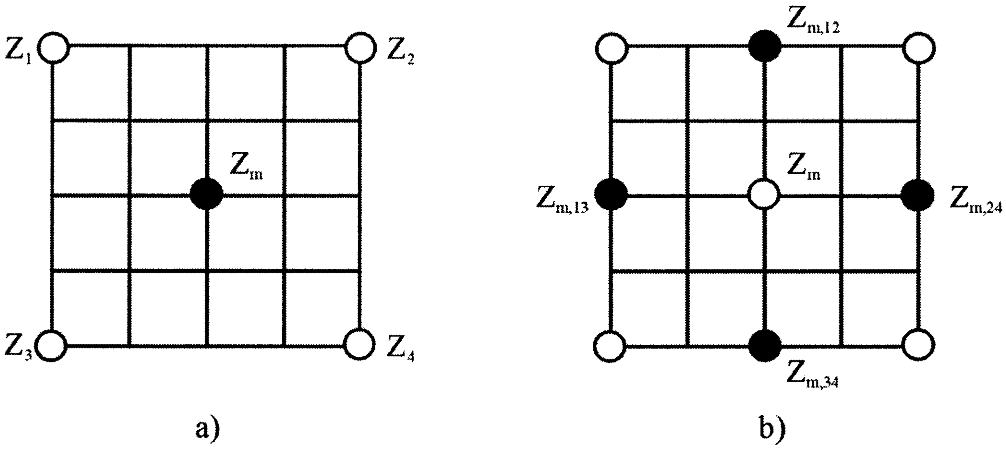

Figure 2.6. First iteration to compute the a) grid and b) segment midpoints.

A second iteration of this process would result in the grids shown in Figure 2.7.

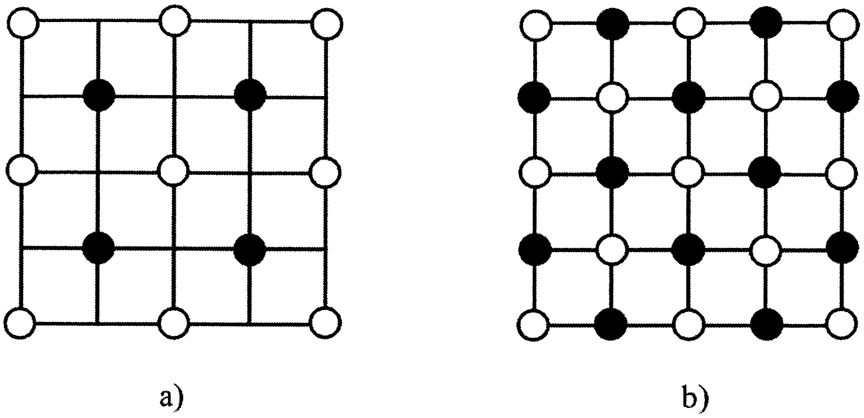
a) b)

Figure 2.7. Second iteration to compute the a) grid and b) segment midpoints.

This process is iterated N times to generate a mesh with $d/(N+1)$ grid spacing. The random number X_n added to the averaged heights is computed from a uniform distribution centered at zero with range of

$$u_n = \frac{1}{2^{(n-1)H}} \quad 0 < H < 1 \tag{2.3}$$

where n denotes the n^{th} iteration. The range is scaled so that the added random noise decreases with the grid spacing. The parameter H characterizes the randomness of the geometry. For a three dimensional surface, the fractal dimension D is defined as

$$D = 3 - H \tag{2.4}$$

The fractal dimension can be thought of as a measure of the roughness of the terrain. For fractal dimensions approaching 2.0, the terrain does not exhibit fractal properties, while terrain with a fractal dimension near 3.0 is extremely rough and physically unrealistic. A fractal dimension of 2.5 represents unbiased Brownian motion of the midpoint displacements. Figure 2.8 illustrates several artificial terrain profiles of different fractal dimensions.

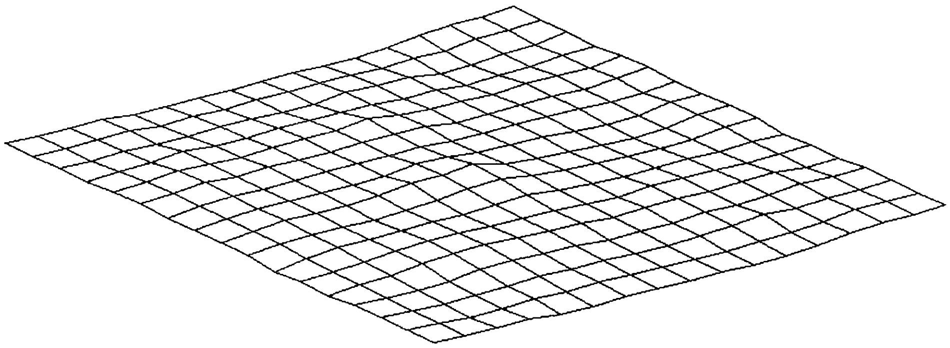

(a) D = 2.1

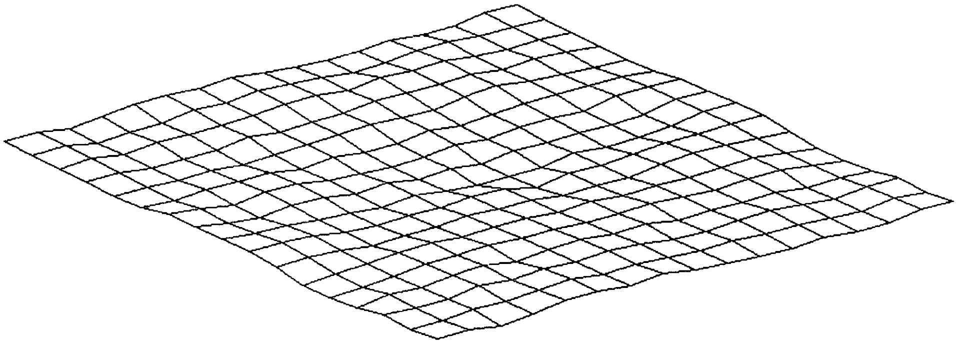

(b) D = 2.3

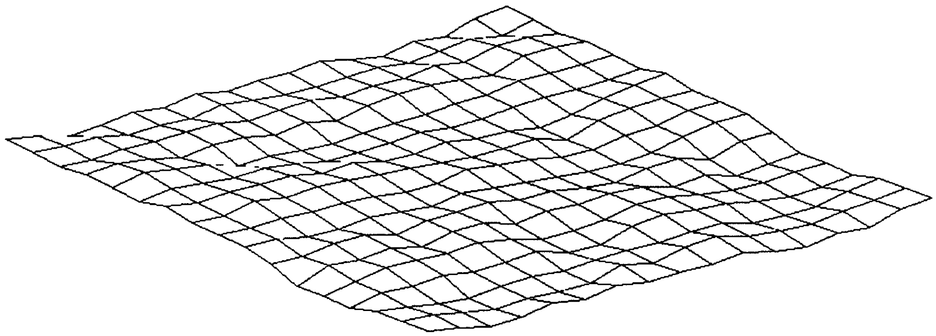

(c) D = 2.5

Figure 2.8. Images of flat terrains with varying fractal dimension D.

The terrains given in the above figure were generated in MATLAB with 289 grid points. The heights of the corner points are prescribed to be zero, and the MPD method is used to interpolate between the corner points. The terrains above are representations of what would be described as a flat terrain patch given a sparse digital elevation map. The representations vary greatly with the fractal dimension. Methods have been proposed to estimate the fractal dimension of natural terrain from sparse data (refer to Section 1.3.3). If knowledge of the fractal dimension is available, dense representations of natural terrain can be generated from sparse data using this method. This type of terrain geometry model is used to represent rough terrain in predictive simulation of high speed maneuvers for sensitivity and uncertainty analysis as explained in Chapter 4. In addition, primitive geometric terrains are used for the validation simulations as explained in Chapter 3.

2.4 Model Simulation Environment

The complexity of the equations of motion for the models presented in this chapter precludes a closed form or analytic solution. Thus, instead of writing the equations of motion explicitly, the vehicle and terrain models were implemented in the commercial dynamic analysis software package, ADAMS 12.0. ADAMS was originally developed at the University of Michigan, and is now marketed by MSC Software. It enables the dynamic simulation of complex mechanical systems by integrating sets of nonlinear differential equations. The software has a graphical CAD-style interface for creating system components such as bodies, links, springs, and dampers, and for applying forces and constraints. Mass properties can be defined by part geometry and material, or can be user-specified.

A key feature used extensively in this study is the ability to model complicated vehicle systems and tire interactions in the ADAMS-Car software package. ADAMS-Car, or A/Car, is an ADAMS interface designed specifically to model and simulate the dynamics of wheeled vehicles. All computer simulations presented in this work were developed and run in A/Car. In this interface, subsystems consisting of basic system elements are used to modularize the vehicle model. These subsystems are then assembled in a complete vehicle model consisting of a body, drive system, brake system, suspensions, and wheels. Uneven terrains are defined as three-dimensional meshes for the analyses presented in this work. Also, the software contains a library of tire models, including the Magic Formula introduced in Section 2.3.1. Figure 2.9 and Figure 2.10

show views of the A/Car simulation model of the physical system described in Section 3.2.1.

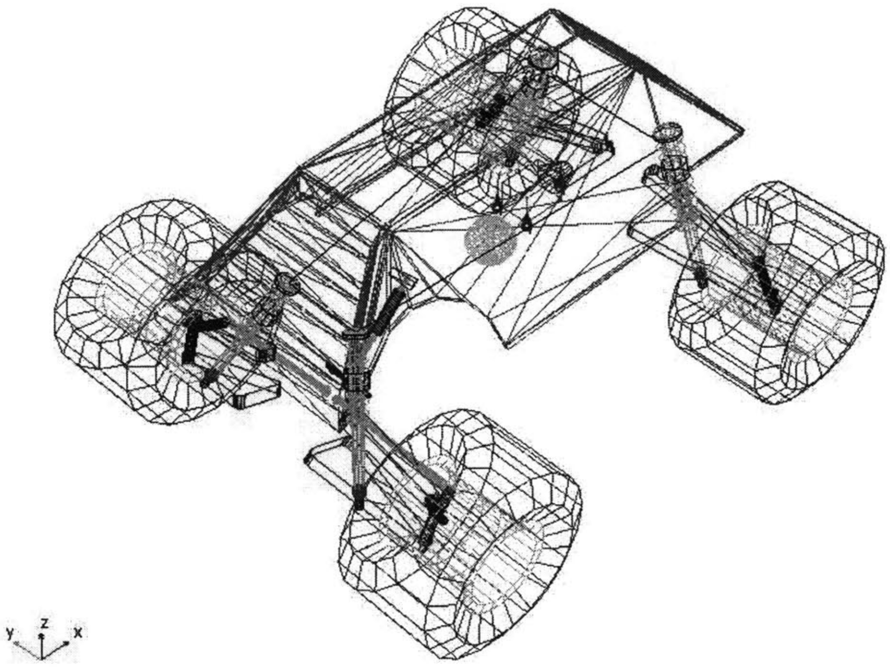

Figure 2.9. ADAMS high-speed model wire frame.

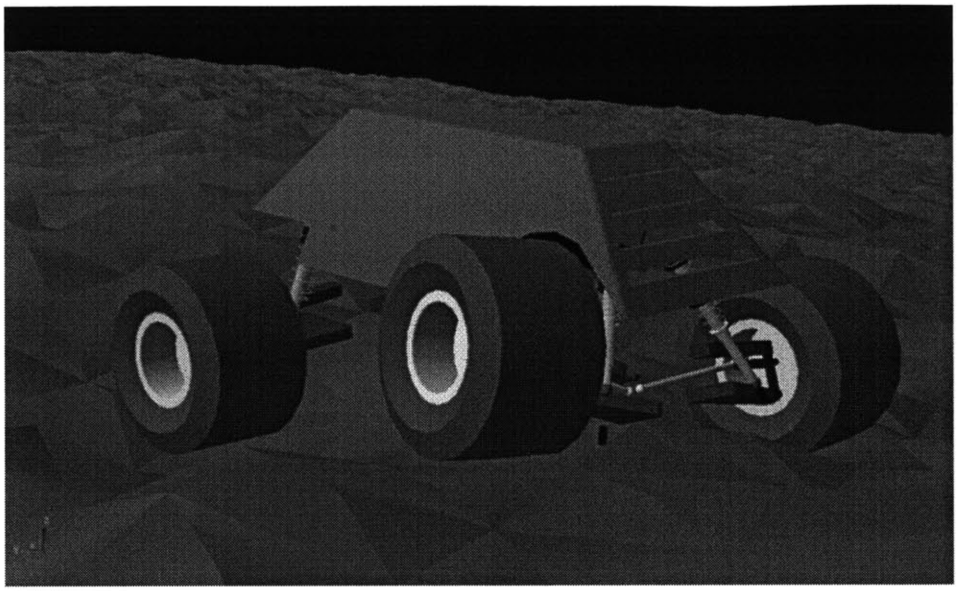

Figure 2.10. View of the high-speed mobile robot model in ADAMS.

During a dynamic simulation, ADAMS solves the set of nonlinear differential and algebraic equations defined by the model. The software provides several numerical integration techniques, including both stiff and non-stiff integrators. A system is said to be numerically stiff when it has widely separated eigenvalues, with the high frequency eigenvalues being over damped. See [Wielenga, 1986] for a discussion of numerical stiffness. Stiff integrators can handle numerically stiff problems, as opposed to non-stiff integrators. Many mechanical systems can be considered numerically stiff, so it is reasonable to select a stiff integrator for simulation of the model given above. The G-Stiff Integrator was chosen for the simulations in this work because of its high-speed, accuracy, and robust ability to handle a variety of analysis problems. For details on stiff integrators, see [Brayton, et al, 1972; Brenan, et al, 1996; Gear, 1971; Van Bokhoven, et al, 1975]. In all simulations, the integration time step was set to 0.005, and the allowable displacement error was set to 0.01 mm.

For more detailed information about the ADAMS software package and its capabilities refer to [ADAMS, 2002].

2.5 Summary

This chapter presented a set of models to describe the motion of high-speed mobile robots operating in rough terrain. The mechanical components of the mobile robot are modeled with a fifteen-degree-of-freedom lumped-parameter model. A model for computing the ground forces on the tires is presented. This model assumes a rigid terrain and compliant tire. An established method for modeling the geometry of natural terrain is also discussed. The method, called midpoint displacement, uses fractals to interpolate sparse digital elevation data and preserve the geometry of natural terrain at all length scales. Finally, the simulation environment used to implement the high-speed mobile robot model is described.

CHAPTER

3

EXPERIMENTAL VEHICLE MODEL VALIDATION

3.1 Introduction

Physics-based models for high-speed mobile robots operating in rough terrain are generally complex and of high order. Such models do not lend themselves to closed form solutions. Instead, simulations are used to numerically solve the model. It is important to experimentally validate these simulation models. A particularly suitable validation method is to model a physical system, apply similar input commands in experiment and simulation, and compare the dynamic response. In this way, one can measure accuracy and develop confidence in the model.

This chapter discusses the experimental validation of the high-speed mobile robot model introduced in Chapter 2. A small, high-speed, experimental mobile robot was built for validation purposes and is described. Parameter identification was performed on the system and the results are presented. The experimental setup used for capturing model validation data is discussed. Simulations of the model validation experiments are discussed, and the results are compared to experimental data.

3.2 Experimental System

The following sections discuss the physical mobile robot and the experimental system and procedures for capturing model validation data for comparison with the simulation model.

3.2.1 High-Speed Tele-Operated Mobile Robot

A 1/10 scale, DC motor-driven mobile robot was built for model validation experiments. The system was based on inexpensive, off-the-shelf components, including chassis, suspension, drivetrain, and wheels. Figure 3.1 depicts the mobile robot.

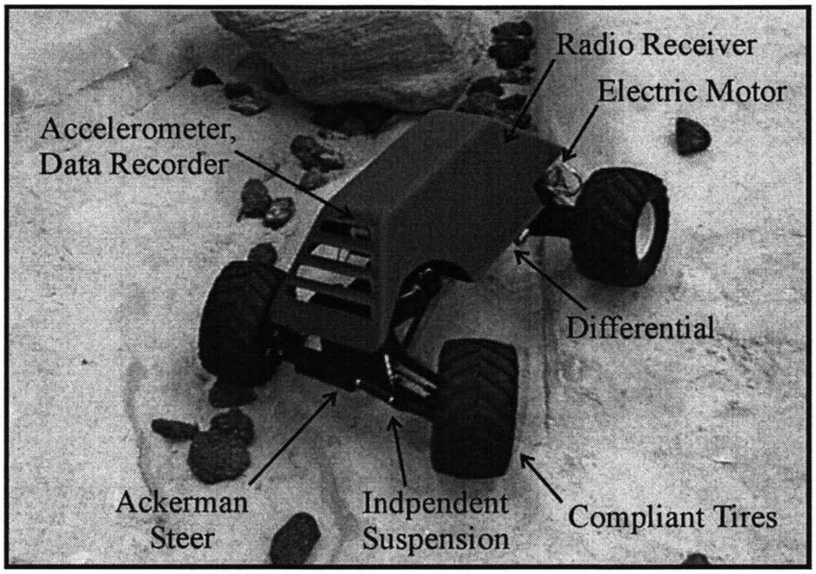

Figure 3.1. Picture of the high-speed tele-operated mobile robot.

The robot is tele-operated and has two control inputs: a rear-wheel drive input, and a front wheel steering servo. The rear wheels are coupled through a differential, and driven by an electric DC motor. The motor is controlled by an electric speed control that responds to inputs from the radio transmitter. An Ackerman linkage couples the front wheels to a steering control servo. The steering control is also commanded by the radio transmitter. The transmitter fixes a desired servo angle, and the servo attains that position.

The robot has a tunable, independent spring-damper suspension. Each of the rear suspensions is a four-bar linkage, while the front suspensions are five-bar linkages. The spring-dampers consist of coil-over springs and oil-bath dashpots. The mobile-robot also has deformable rubber tires mounted on stiff, plastic rims. The vehicle chassis houses a large quad D-size battery pack, electronic speed controller, radio signal receiver, three-axis accelerometer, portable data recorder, and sensor battery pack. A frame was devised to mount the sensor equipment, and mounted to main vehicle chassis. In addition, a tough, ABS plastic shell was built to house and protect the onboard electronics.

Experimental identification of the mobile robot's dynamic parameters was performed for use as an input to the simulation model. The lumped parameters include mass properties of the vehicle body and wheels, and stiffness and damping of the suspension and tires. The suspension stiffness and damping are assumed to be nonlinear functions, while the tire stiffness and damping are taken to be linear. See Appendix A for further discussion about the identification methods used, and for a presentation of the resulting data. Figure 3.2 shows the axis conventions and Table 3.1 summarizes the physical parameters.

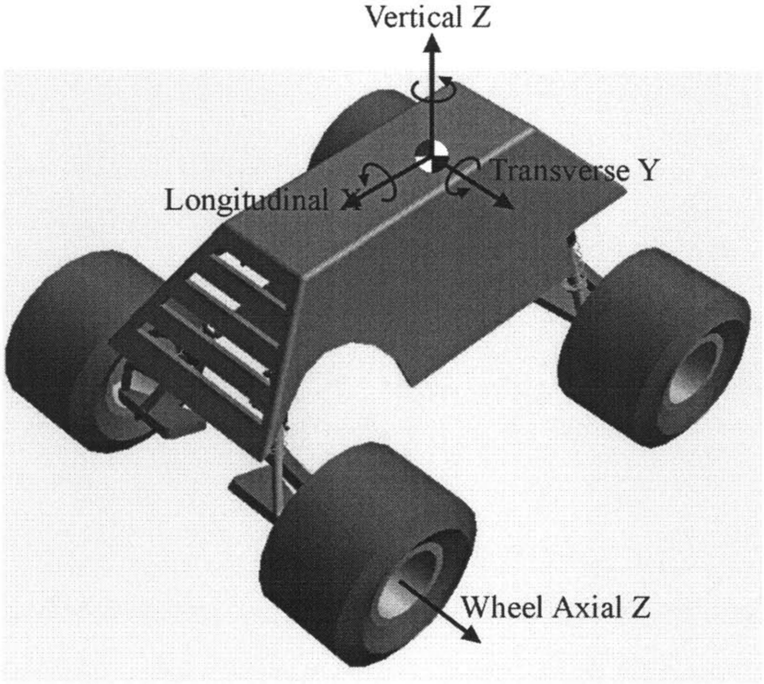

Figure 3.2. Diagram of the mobile robot axis conventions.

Table 3.1. Physical parameters of the high-speed, tele-operated mobile robot

Parameter	Value	Units
Mass	3.1	kg
Dimensions	0.30 x 0.30	m
Longitudinal Axis Moment of Inertia	0.0065	kg·m^2
Transverse Axis Moment of Inertia	0.022	kg·m^2
Vertical Axis Moment of Inertia	0.023	kg·m^2
Wheel Radius, Width	0.061, 0.066	m
Wheel Axial Moment of Inertia	0.0004	kg·m^2
Wheel Transverse Moment of Inertia	0.0003	kg·m^2
Wheel Stiffness	6000	N/m
Wheel Damping	18	N·s/m
Suspension Stiffness	500	N/m
Suspension Damping (v is compression rate)	$74.1v^2 + 41v$	N·s/m

3.2.2 Validation Experiments

Experiments were conducted to validate the high-speed mobile robot simulation models. In these experiments, the mobile robot discussed in the previous section was commanded to traverse a positive obstacle while a portable data recorder logged measurements from an onboard three-axis accelerometer. A positive obstacle is defined as an object that protrudes above the surrounding terrain surface. Figure 3.3 presents a diagram of the experimental system and procedure.

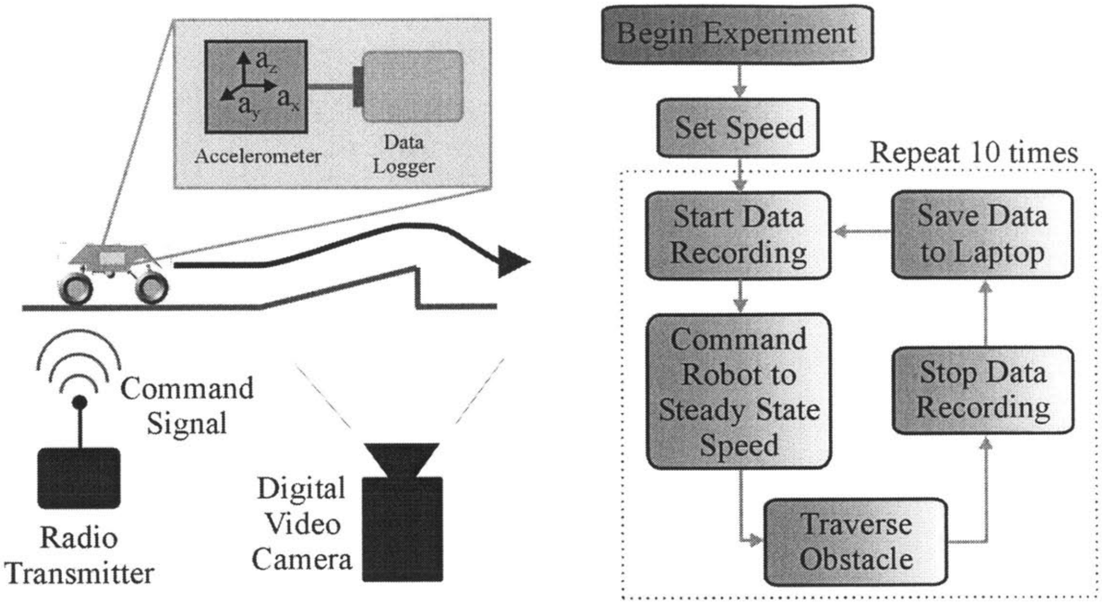

Figure 3.3. Model validation experimental setup and procedure.

Ten experiments were completed at three different speeds for each obstacle (ramp and impulse bump) to mitigate the effects of variation in control input. Thus, the total number of experiments per obstacle is thirty.

The vehicle approach speed was set by maintaining a set control level. The vehicle was driven on a flat surface for several meters so as to attain a steady-state velocity prior to traversing the obstacle.

A digital video camera recorded the robot's motion to measure the approach velocity. Markers were placed along the approach path at a measured distance in the field-of-view of the camera. By measuring the video frame times that the vehicle passes the final marker and contacts the obstacle, the approach speed is estimated by

$$V_{approach} = \frac{d}{t_{obs} - t_{marker}} \tag{3.1}$$

where d is the distance between the last marker and the obstacle, t_{obs} is the time at the obstacle, and t_{marker} is the time at the marker. The frame rate of the camera is 30 Hz. A sample image from the digital camera showing the mobile robot traversing the ramp obstacle is shown in Figure 3.4.

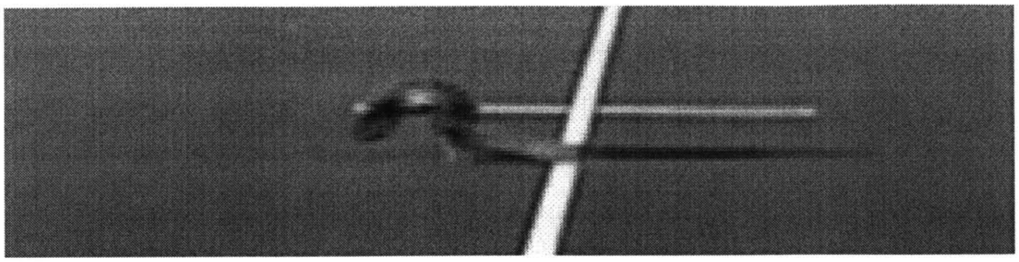

Figure 3.4. Image of the tele-operated mobile robot traversing ramp obstacle.

The surface chosen for validation experiments was MIT's Astroturf practice field. The turf is flat, and rigid relative to the mobile robot's tires, so it can easily be modeled in simulation as a rigid, flat surface. Also, the friction coefficient between the tires and the turf is sufficiently high to prevent wheel slip. Complex tire-terrain interaction models are therefore unnecessary, simplifying the model parameter identification process. In simulation, the friction coefficient was set sufficiently high to prevent wheel slip. Two rigid, physical obstacles were constructed. The bump obstacle is made of wood, while the ramp surface is made of fiber board with wooden supports.

A three-axis accelerometer was used in conjunction with a portable data logger to record the dynamic response of the mobile robot during obstacle traversal. The accelerometer is the Crossbow CXL04M3 three-axis model. The accelerometer specs are given in Appendix A. Accelerometer output voltages were recorded with a Pace Scientific XR440-M Pocket Logger. The pocket Logger is a small programmable flash memory module that can simultaneously measure and store four channels of voltages at prescribed intervals. Appendix A provides a summary of the pocket logger specifications.

3.3 Validation Methodology

The high-speed, rough-terrain mobile robot model presented in Chapter 2 has been experimentally validated with a small experimental system described in Section 3.2. The validation method consists of three phases: 1) execution of experiments to measure the dynamic response of a high-speed mobile robot on simplified terrain; 2) computer simulation of the mobile robot model executing the same motion in 1) on a modeled terrain; and 3) comparison of the results. A diagram of this scheme is presented in Figure 3.5.

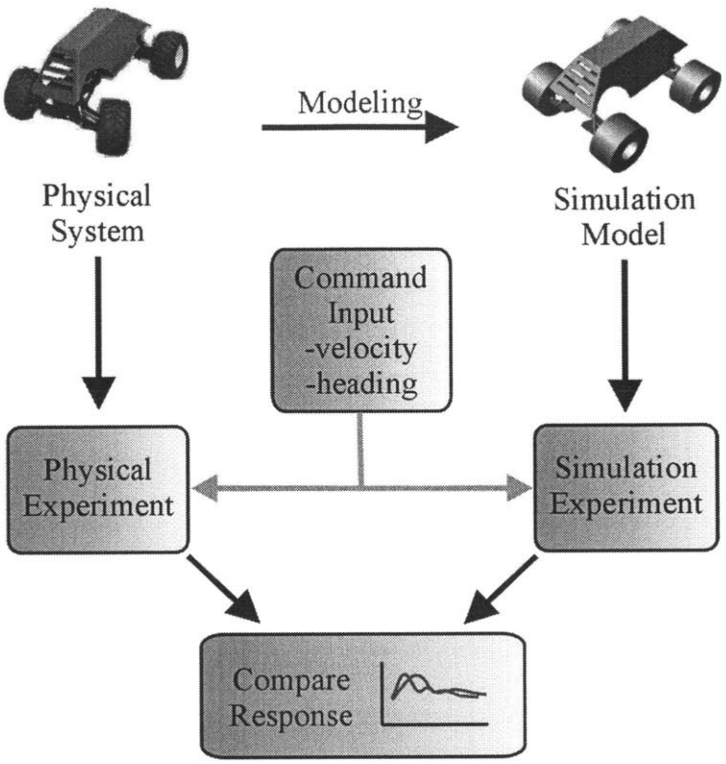

Figure 3.5. Model validation block diagram.

In this method, the dynamic parameters of the physical system are identified experimentally, and a model of the system (see Chapter 2) is created in simulation software. Similar torque and steering commands are input into the experimental system and simulation model. The dynamic motion of the system is recorded in both cases and compared.

Flat terrain with simple geometric features was used for validation experiments, since geometric terrains are easily modeled in simulation. This allows us to study the accuracy of the dynamic system model irrespective of the terrain model. For this analysis, two geometric obstacles were used - a ramp and impulse bump, shown in Figure 3.6. These terrain geometries were chosen to excite the in-plane pitch dynamics of the vehicle, and for ease of implementation.

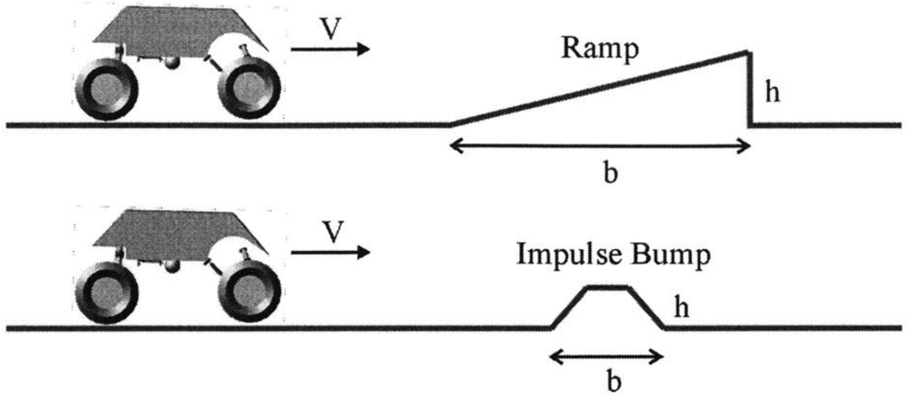

Figure 3.6. Model validation experiment positive obstacle geometries.

In this analysis, the mobile robot is commanded to approach the obstacles at a constant speed. In experiment, the tele-operated mobile robot is commanded a fixed drive torque through the experiment by maintaining a set position of the control trigger on the radio transmitter. The experimental obstacle approach velocity is measured and used as the desired velocity for the simulation model. A simple proportional controller is used to control the simulated robot's speed before and during positive obstacle traversal. Linear accelerations in three axes are recorded for the duration of the experiment and compared to simulation.

3.4 Computer Simulations

A simulation model of the mobile robot and terrains presented in Section 3.2 was created using the ADAMS/Car software package (see Chapter 2). The positive-obstacle validation experiments described in Section 3.2.2 were then simulated. Images of the positive obstacle simulations are provided in Figure 3.7.

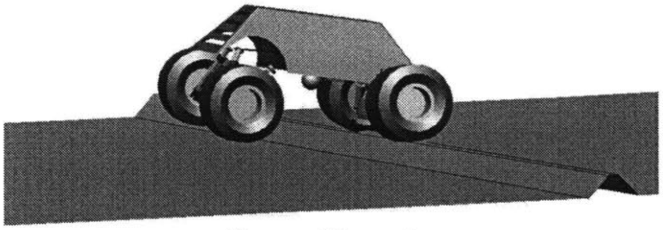

Bump Obstacle

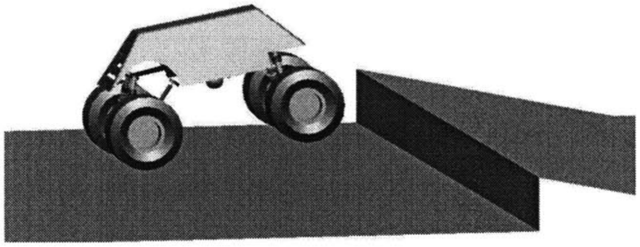

Ramp Obstacle

Figure 3.7. Images of bump and ramp simulation experiments.

The obstacle and surface geometry were modeled using measurements of the physical system. The simulated terrain was defined to be rigid relative to the tires, and the friction coefficient between the tires and the terrain was set to $\mu = 1.0$. This high value sufficiently constrained the tires to little or no slip, as is the case in the experimental system. The Magic Formula tire model discussed in Section 2.3.1 was used. See Appendix B for a list of the MF-Tire model parameters.

A proportional controller regulated the velocity of the simulated mobile robot. The controller set the robot velocity equal to that measured during experiments. The control law applies equal torque to both wheels, and is given as follows:

$$\tau = \begin{cases} K\left(V_{des} - V_{act}\right) & \tau < \tau_{\max} \\ \tau_{\max} & \tau \geq \tau_{\max} \end{cases} \tag{3.2}$$

where K is the proportional gain, V_{des} and V_{act} are the desired and actual vehicle speeds, respectively, and τ_{max} is the saturation limit. Torque is limited by the maximum output of the mobile robot's electric motor. In the simulations, the vehicle starts from rest and accelerates to a constant velocity before contacting the obstacle.

The simulated vehicle maneuvers described above are defined using Driver Control Files (DCF) in ADAMS/Car. Appendix C contains example of the DCF files used in these simulations.

3.5 Results

The following sections present simulation and experiment data of the tele-operated vehicle traversing both the bump and ramp obstacles at three different speeds. Linear acceleration in three axes was recorded for each trial, and compared to accelerations computed in simulation. In addition, visual data is presented from experiment and simulation of the vehicle traversing a negative obstacle at various speeds. Because the physical and numerical experiments in this chapter are effectively planar (i.e. no out-of-plane dynamics were excited), only the accelerations in the plane are presented and compared.

3.5.1 Negative Obstacle

In these experiments, the mobile robot was commanded to approach a negative obstacle along a straight path at three different speeds. A negative obstacle is defined to be a depression in the local terrain surface, such as a ditch. The vehicle was commanded to traverse the obstacle at 1.4 m/s, 3.2 m/s, and 7.4 m/s. A simulation was then performed at each of these speeds. Figure 3.8 shows a photo series of the experimental and simulated robot traversing the obstacle at 7.4 m/s.

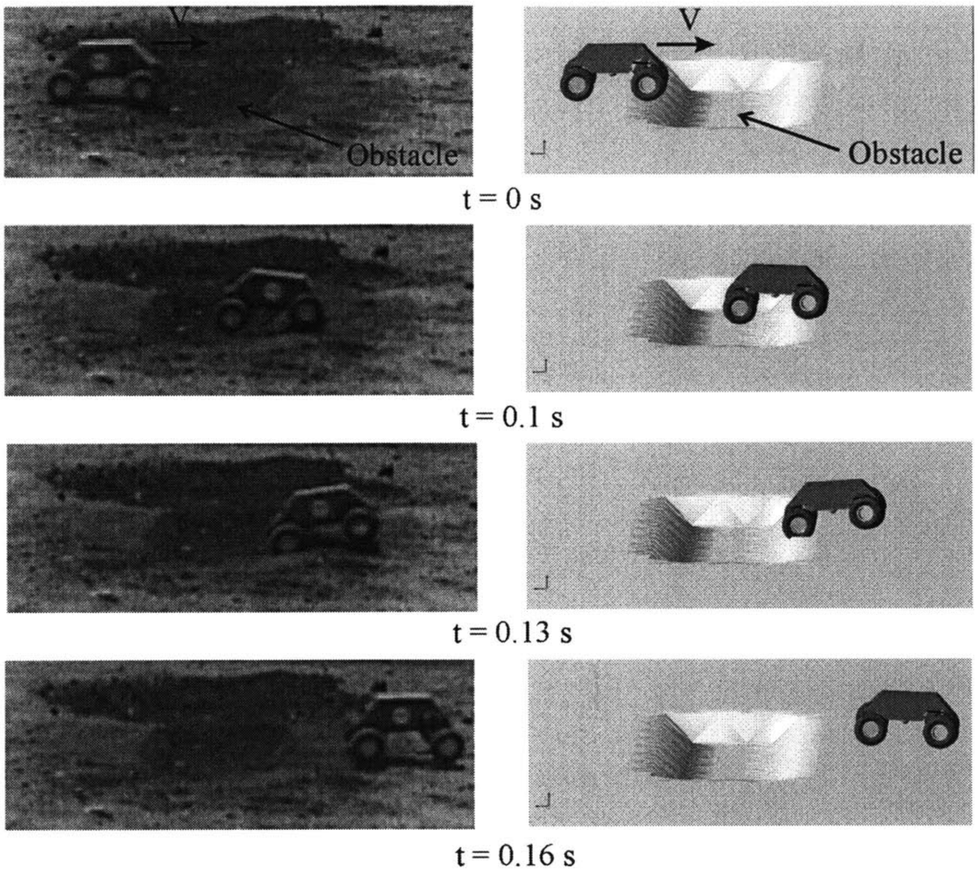

Figure 3.8. Photo series of the experimental and simulated vehicle traversing a negative obstacle, V=7.4 m/s.

The experiment and simulation correspond well. At this speed, the experimental robot successfully traversed the obstacle. The simulation correctly predicted the traversability at this speed. Table 3.2 presents the traversability results at each speed for both simulation and experiment.

Table 3.2. Negative obstacle traversability results.

Speed (m/s)	Experiment	Simulation
1.4	Success	Success
3.2	Failure	Failure
7.4	Success	Success

At the intermediate speed, the physical and simulated robots collide with the far edge of the obstacle, and the traverse fails. The simulation model correctly predicted traversability at each of the speeds. However, the model-based analysis was found to be highly sensitive to the terrain model. This would suggest that modeling effort should focus on an accurate representation of wheel-terrain interaction.

3.5.2 Impulse Bump Obstacle

In these experiments, the mobile robot was commanded to approach the bump obstacle along a straight path ten times at three different speeds. A simulation was then performed with the approach speed equal to the mean value of each set of the three speeds. Table 3.3 summarizes the approach velocity data for experiment and simulation.

Table 3.3. Impulse bump experiment speeds.

Experiment Trial	Low Speed (m/s)	Mid Speed (m/s)	High Speed (m/s)
1	1.7	2.7	4.2
2	1.8	3.0	4.6
3	1.8	2.6	3.7
4	1.8	3.0	3.9
5	1.8	3.0	3.4
6	1.8	2.9	3.4
7	1.8	2.6	3.7
8	1.7	3.0	3.2
9	1.8	3.0	3.4
10	1.8	2.9	3.7
Experiment Mean	1.8	2.9	3.7
Simulation	1.8	2.9	3.7

For illustration, Figure 3.9 shows a comparison of the experimental and simulated trajectories during bump traversal at an approach speed of 3.0 m/s.

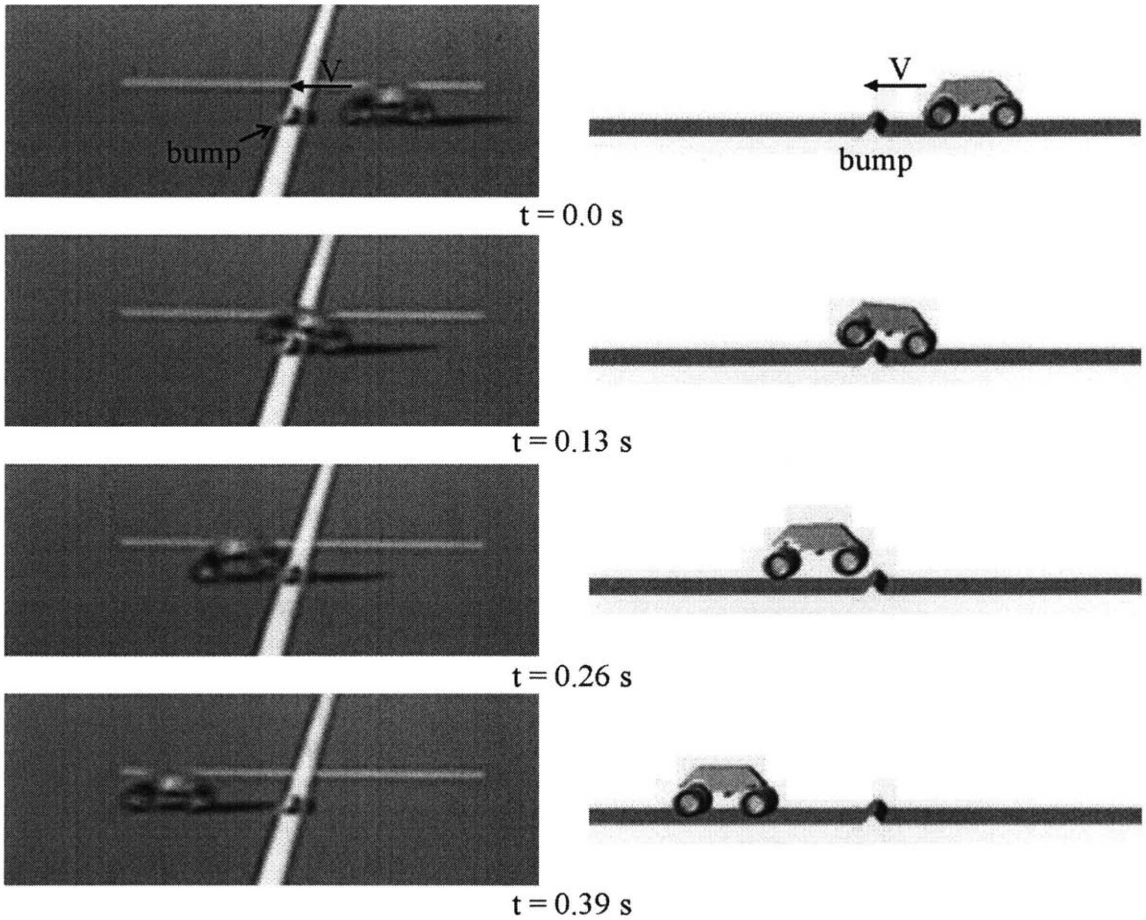

Figure 3.9. Impulse bump experiment and simulation image sequence; V = 3.0 m/s.

Acceleration data in two axes was compared for each experiment and simulation trial. The longitudinal acceleration along the length of the vehicle, and the vertical acceleration normal to the length of the vehicle (see Figure 3.2) are plotted for various speeds in Figure 3.10, Figure 3.11, and Figure 3.12. All acceleration data are aligned so that initial obstacle contact occurs at 0.5 seconds. The average experimental acceleration at each time step is plotted with the simulated acceleration. The simulation approach speed was set to the average of the ten experimental trials. The simulation data was saturated to replicate experiment sensor saturation at 40 m/s^2.

Figure 3.10 shows the experimental and simulated acceleration for an average approach speed of 1.8 m/s.

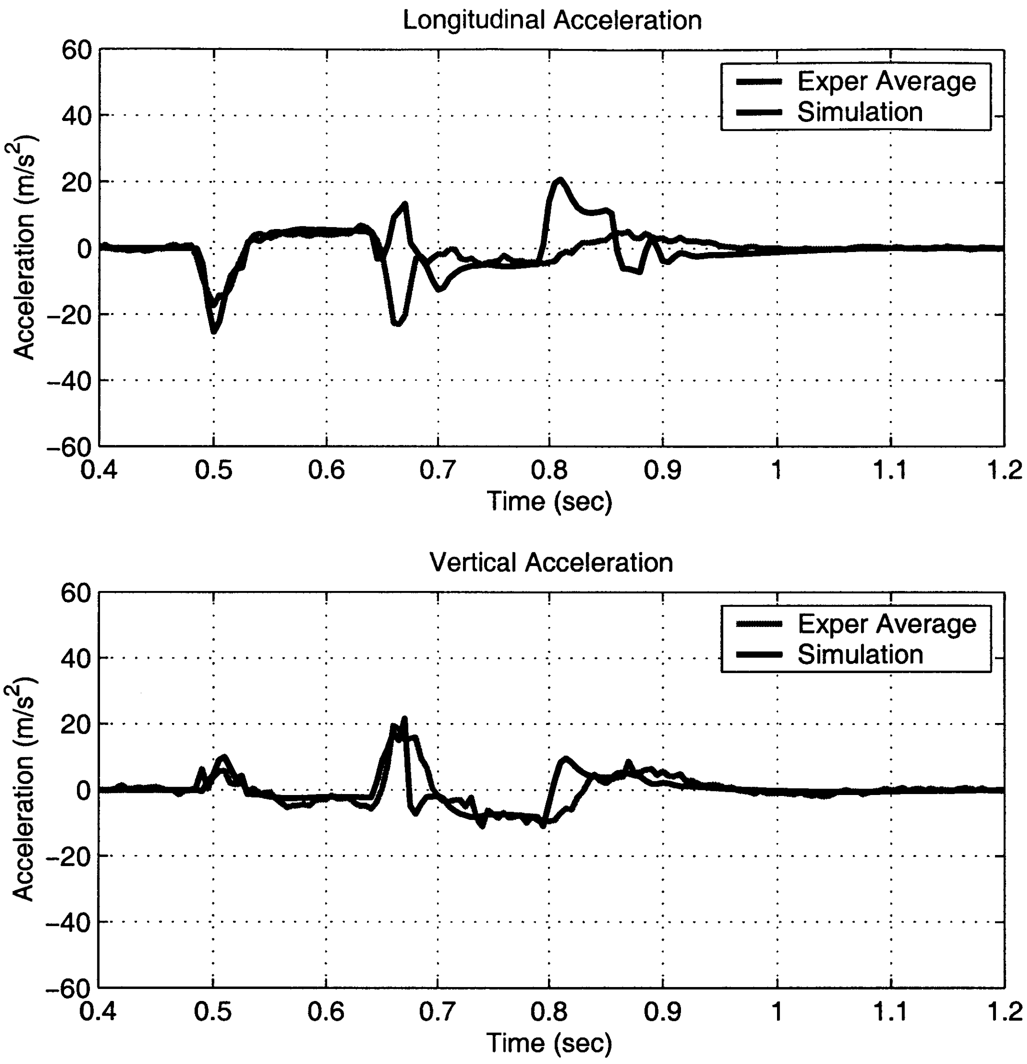

Figure 3.10. Bump obstacle longitudinal and vertical acceleration; 1.8 m/s approach speed.

Deviations are apparent in the longitudinal acceleration at t = 0.65, 0.8 seconds. This is due largely to the difference in velocity control schemes. Proportional control in simulation attempts to counter the obstacle-induced deceleration by applying more torque to the rear wheels, causing the vehicle to accelerate at two instances: after the front wheels pass the obstacle (t = 0.65), and after the rear wheels pass the obstacle and regain contact with the ground. The constant torque drive in the experimental system does not exhibit this behavior. The experimental and simulated vertical acceleration data show good correspondence over most of the maneuver. Aside from the controller-induced differences, the simulated data follows the experimental data quite well.

Figure 3.11 shows the acceleration data for an approach velocity of 2.9 m/s.

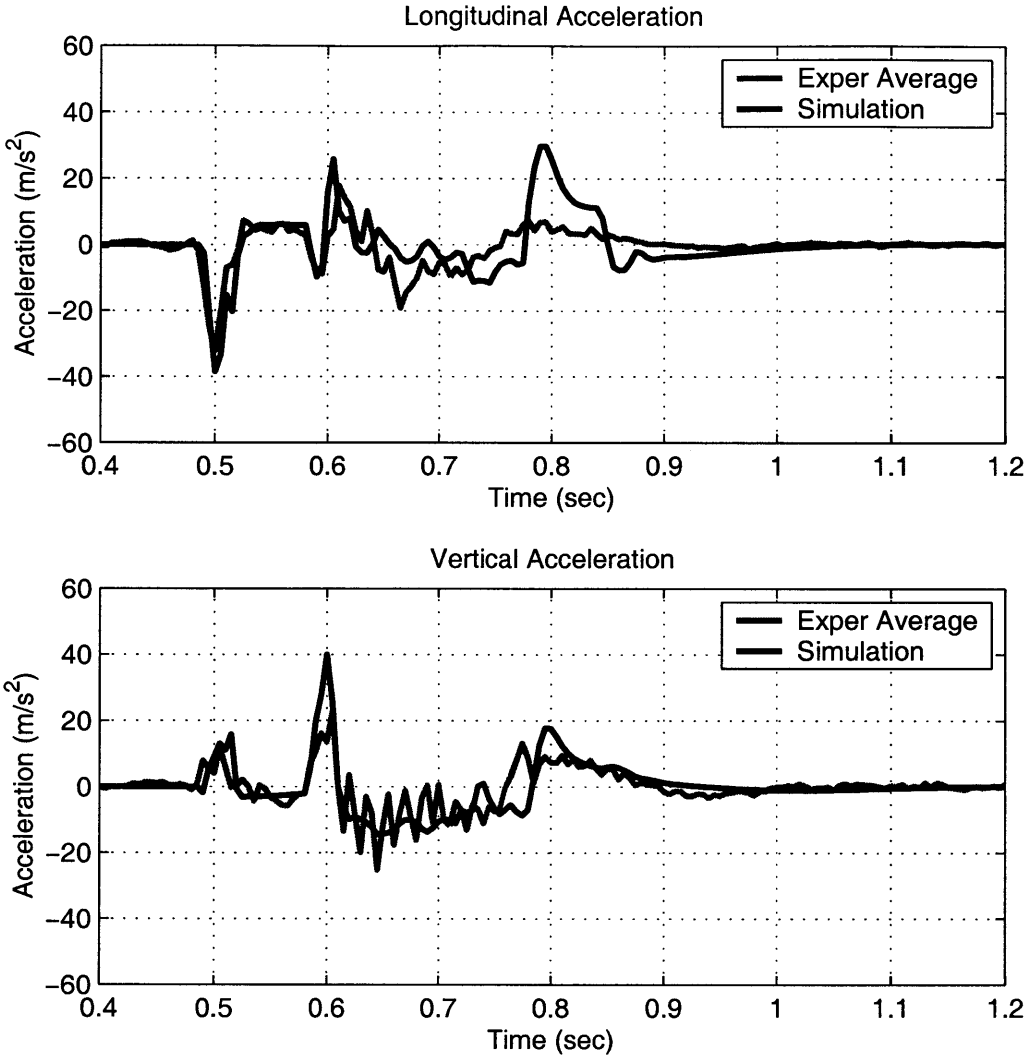

Figure 3.11. Bump obstacle longitudinal and vertical acceleration; 2.9 m/s approach speed.

As in the previous case, proportional control causes a large peak in the simulated longitudinal acceleration at t = 0.8 seconds. The vertical acceleration data correlates well, except for the large spike in simulation data at t = 0.6 seconds. This is due to the averaging of temporally-spaced peaks. Accelerometer saturation occurs at about 40 m/s^2. The simulation data was artificially saturated to replicate the experiment conditions. The simulation and experiment acceleration data compare favorably in light of the proportional control errors.

The acceleration data for the final approach velocity of 3.7 m/s is presented in Figure 3.12. This is a very high speed with respect to the size of the vehicle.

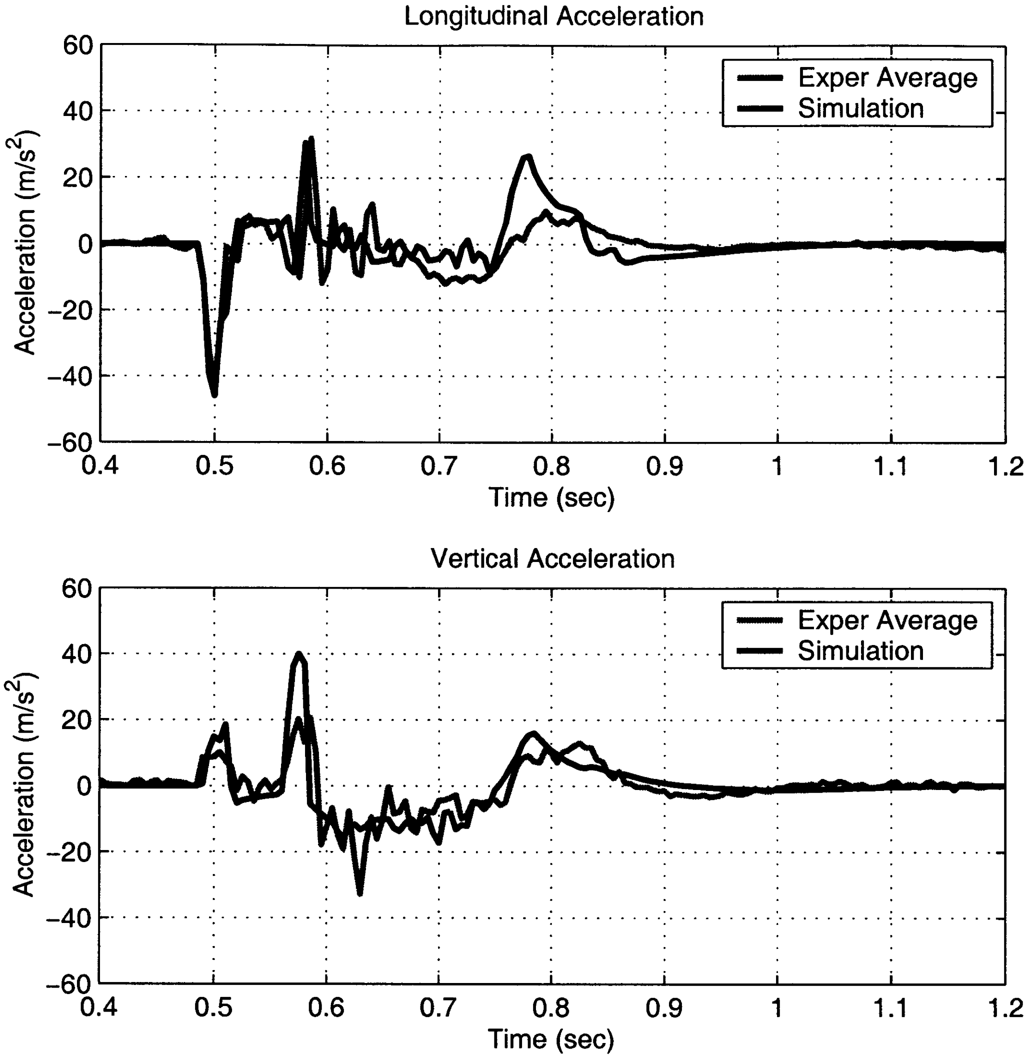

Figure 3.12. Bump obstacle longitudinal and vertical acceleration; 3.7 m/s approach speed.

From the figure, it can be seen that the simulated acceleration data closely follows the average experiment acceleration data. The relatively large longitudinal acceleration peak in the simulated data at t = 0.8 seconds can be attributed to the proportional controller, as in the previous cases. The large discrepancy in vertical acceleration peak heights at about t = 0.57 seconds is due to averaging of temporally-spaced peaks over the experiment trials. Overall, the simulation and experimental data compare very favorably at this speed.

3.5.3 Ramp Obstacle

In these experiments, the mobile robot was commanded to approach the ramp obstacle along a straight path ten times at three different speeds. A simulation was then performed with the approach speed equal to the mean value of each set of the three speeds. Table 3.4 summarizes the approach velocity data for both experiment and simulation.

Table 3.4. Ramp experiment speeds.

Experiment Trial	**Low Speed (m/s)**	**Mid Speed (m/s)**	**High Speed (m/s)**
1	2.0	2.9	3.7
2	2.6	3.0	3.4
3	3.0	3.0	3.7
4	2.7	2.7	3.4
5	2.7	2.9	3.4
6	2.4	2.9	3.7
7	2.3	2.5	3.2
8	2.3	2.9	3.4
9	2.2	2.6	3.4
10	2.2	2.9	3.4
Experiment Mean	2.5	2.8	3.5
Simulation	2.5	2.8	3.5

For illustration, Figure 3.13 shows a comparison of the experimental and simulated trajectories of the mobile robot during ramp traversal at approach speeds of 2.9 m/s, and 2.8 m/s, respectively.

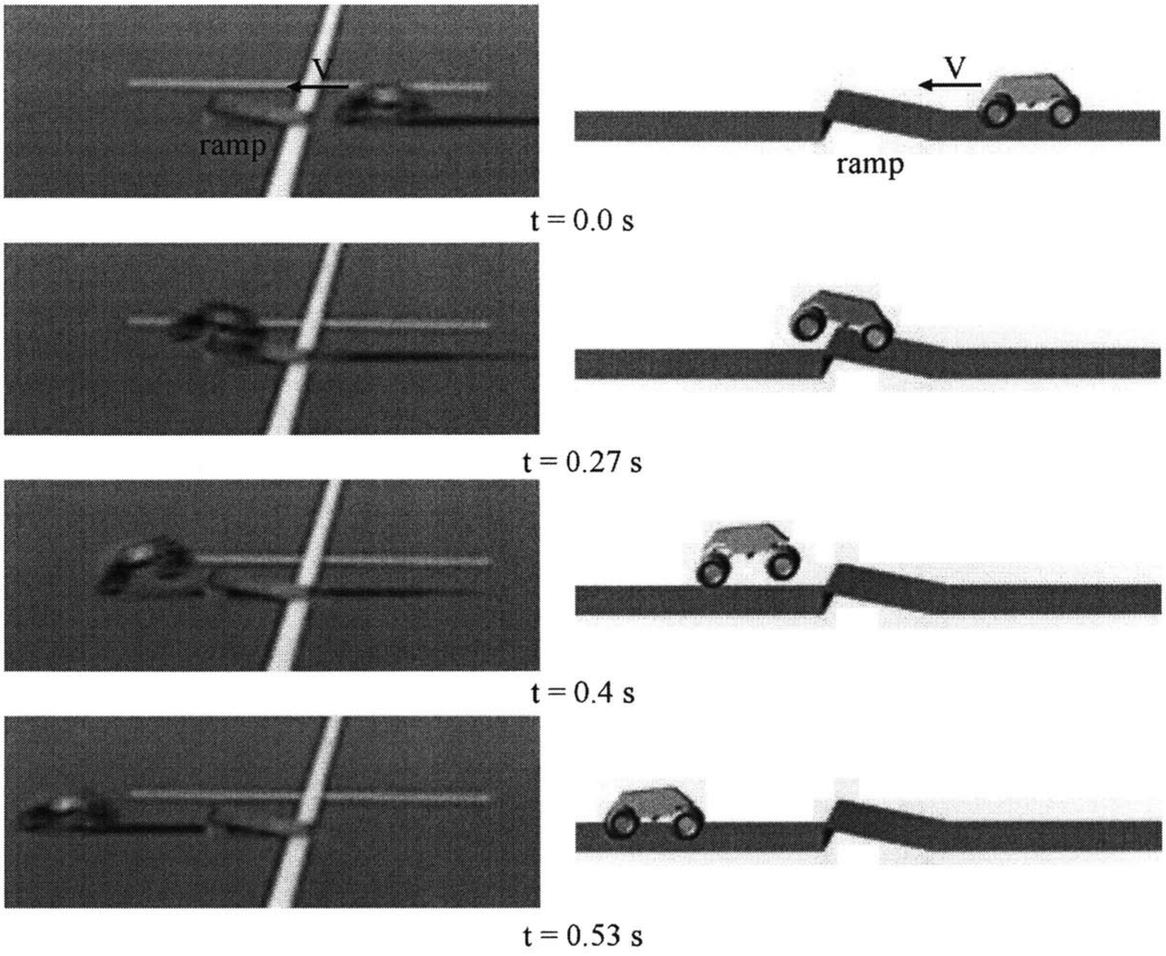

Figure 3.13. Images of ramp experiment and simulation image sequence; V = 3.0 m/s.

As in the previous section, acceleration data in two axes was captured for each experiment and simulation trial. The longitudinal acceleration and the vertical acceleration (see Figure 3.2) are plotted in Figure 3.14, Figure 3.15, and Figure 3.16. This acceleration data is aligned so that initial obstacle contact occurs at 0.5 seconds. The average experimental acceleration at each time step is plotted with the simulated acceleration. The simulation approach speed was set to the average of the ten experimental trials.

Figure 3.14 shows the experiment and simulation acceleration for an average approach speed of 2.5 m/s.

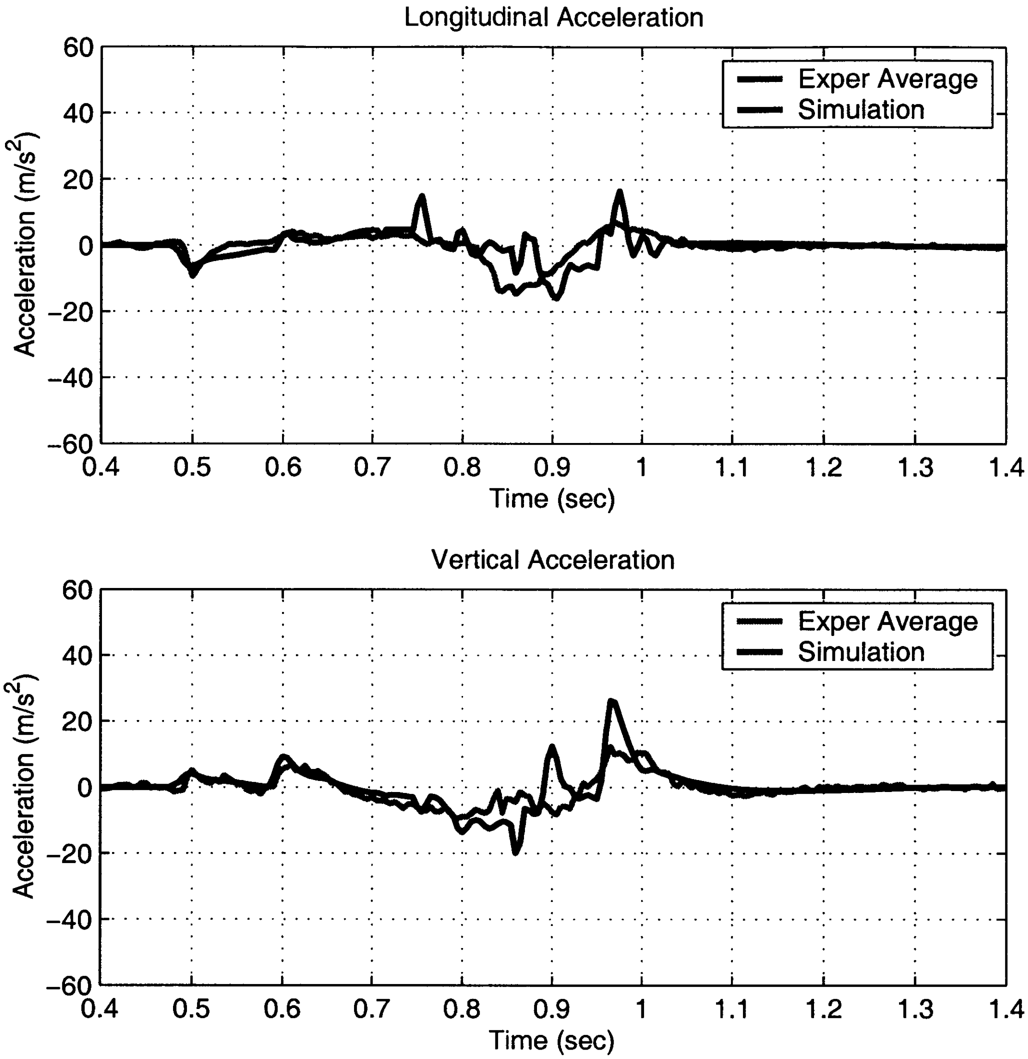

Figure 3.14. Ramp obstacle longitudinal and vertical acceleration; 2.5 m/s approach speed.

The data shows good correlation between simulation and experiment over most of the maneuver. However, moderate peaks occur in the simulated data between 0.8 seconds and 0.1 seconds that are not evident in the experiment data. At this slow approach speed, the electric motor of the experimental system has a low power output, and therefore the speed maintained during obstacle traversal varies significantly from one trial to the next. Therefore, the experiment peaks from each trial are temporally spaced, and when averaged, form a single broad peak. On the whole, the simulation data closely correlates to the experimental data.

Figure 3.15 presents the simulated and experiment data for an approach velocity of 2.8 m/s.

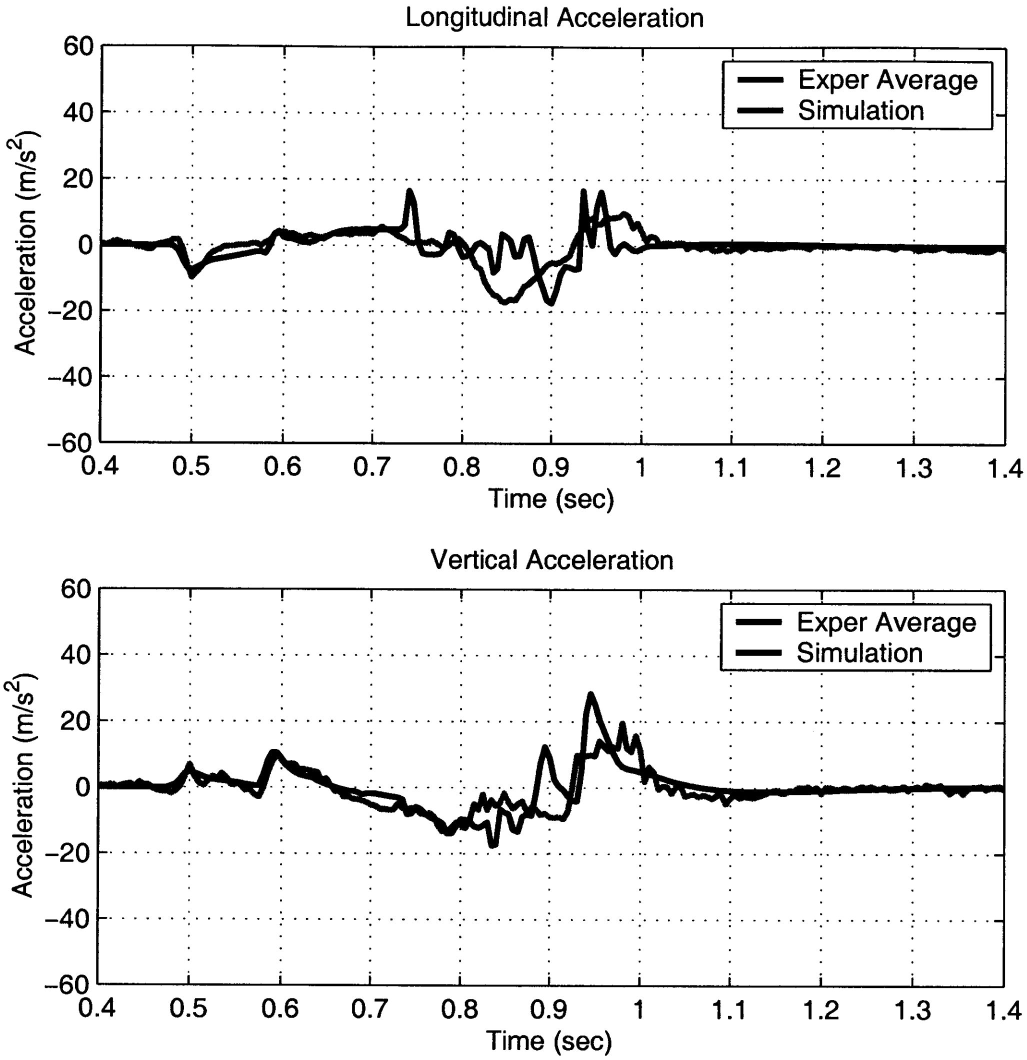

Figure 3.15. Ramp obstacle longitudinal and vertical acceleration; 2.8 m/s approach speed.

Again, the simulation and experiment data correlate well over most of the maneuver at this moderate speed. The simulated and experimental longitudinal acceleration vary because of the differences in the velocity control schemes, as in the bump experiments. Overall, the acceleration from simulation and experiment agree well at moderate speed.

Figure 3.16 shows the data for the high speed case, where the average approach speed was measured to be 3.5 m/s.

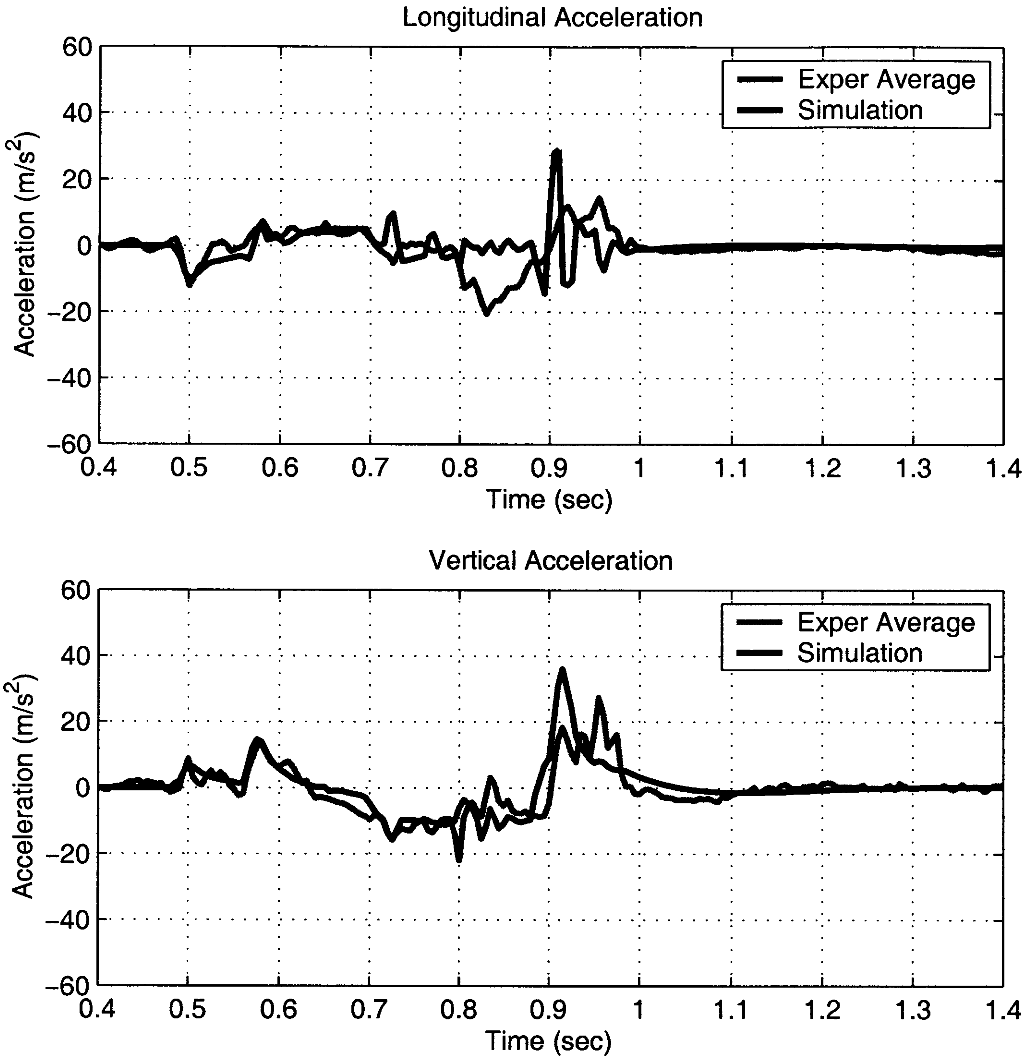

Figure 3.16. Ramp obstacle longitudinal and vertical acceleration; 3.5 m/s approach speed.

At high speed, the data suggests good agreement between simulation and experiment. The large acceleration peak at 0.9 seconds in the simulated longitudinal acceleration is again due to the proportional control scheme.

3.6 Summary and Conclusions

This chapter presented the methodology and results of a series of experiments and simulations designed to validate a model of a high-speed mobile robot operating in rough terrain. A small, tele-operated experimental vehicle was introduced and discussed. The experimentally-determined model parameters were also presented. Simulation and experimental methodology were discussed, and resulting data from both experiment and simulation were presented.

Good agreement was observed between the simulation model and the physical system. This implies that model order is sufficient, and that important system dynamics are captured. Discrepancies in the simulation and experiment data have been attributed to disparity in the velocity control schemes and averaging of temporally-spaced peaks in the experiment data. Overall, the results indicate that the simulation model accurately predicts complex motion of high-speed mobile robots on uneven terrain if the system parameters are known. Therefore, it is important to accurately determine system parameters for modeling complex, high-order dynamic systems.

CHAPTER

4

SENSITIVITY AND UNCERTAINTY ANALYSIS

4.1 Introduction

The dynamics of high-speed mobile robots operating in rough terrain are complex and inherently uncertain. Uncertainty arises from practical limits of physical measurements, changing parameters, and unknown environment conditions. From a practical perspective, it would be desirable to quantify the sensitivity of the robot dynamic response to uncertainty in individual system parameters. The end user of a physics-based control and planning algorithm (see Chapter 1) could use the sensitivity results to shift modeling effort to the most sensitive system parameters.

The algorithms presented in Chapter 1 use off-line simulations to predict the dynamics of mobile robots during high-speed maneuvers. Uncertainty in mobile robot model parameters results in uncertainty in the predicted motion. It would be desirable to quantify the relationship between parameter uncertainty and behavior uncertainty. This could lead to the development of an algorithm that is robust to modeling uncertainty. Knowledge of the prediction uncertainty would also enable a control and planning algorithm to set performance bounds on the predicted motion, and adjust the trajectory and control accordingly.

This chapter presents an initial simulation-based investigation of the system parameter sensitivity and model prediction uncertainty of high-speed motion of mobile robots operating in rough terrain. Two representative maneuvers were chosen for these studies: high-speed turning, and emergency braking. These maneuvers were chosen because they are aggressive, dynamic behaviors that could be used in a high-speed reactive control architecture to avoid unforeseen obstacles. The sensitivity of these maneuvers to various system parameters is investigated using a statistical technique developed for nonlinear models. The method is validated against a simplified analytical model. Results are presented for the representative maneuvers. The relationship between system parameter uncertainty and output response uncertainty is also studied for both the braking and turning maneuvers.

4.2 Simulated Maneuvers

Mobile robot motion can be decomposed into combinations of a set of fundamental maneuvers: turning, acceleration, and braking. In this composition, straight motion is classified as a turn with infinite radius of curvature. When linked together, these basic maneuvers can form an arbitrarily complex trajectory. It is desired to study the sensitivity of these fundamental maneuvers. If the sensitivity of these fundamental maneuvers can be understood, the analysis could be extended to more complex motions.

Two basic maneuvers were studied in this work. These are emergency braking and constant-speed, constant radius turning. Emergency braking was chosen because of its importance as an emergency maneuver. It represents an aggressive, dynamic, reactive-type behavior that would be employed in high-speed mobile robot control and planning. Turning is also fundamental to mobile robot motion on rough terrain. In the analysis presented here, the high-speed turn is studied as an open-loop maneuver, similar to a reactive “hard turn” for avoiding a short-range obstacle. The maneuvers are simulated on rough, level terrain generated using the fractal techniques described in Section 2.3.2. A more thorough description of these maneuvers is presented below.

4.2.1 Emergency Braking

Emergency braking, or skid stopping, would be used to bring the mobile robot to a sudden stop on rough terrain. This maneuver might be executed if a robot cannot sufficiently re-plan and execute a path to avoid an obstacle. This is a very important maneuver necessary to insure the safety of the vehicle. The robot must be able to safely stop within range of the obstacle. Due to system and environment uncertainty, the actual stopping distance would deviate from the desired stopping distance. Therefore the sensitivity and uncertainty of stopping distance to system parameters is studied. Figure 4.1 presents a schematic of the behavior.

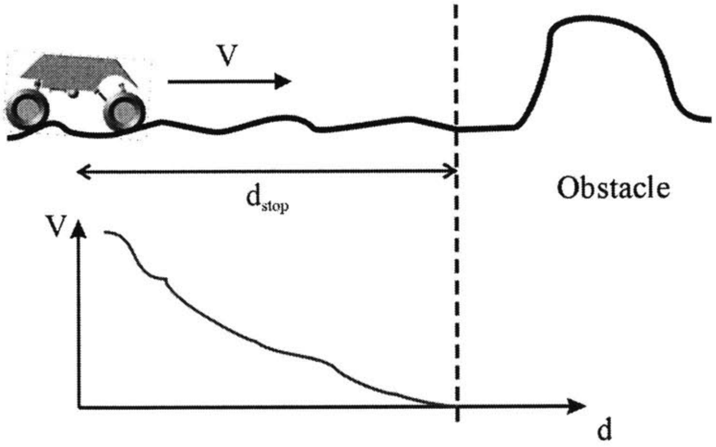

Figure 4.1. Schematic of the emergency braking simulation.

The maneuver consists of applying a braking force to the rear wheels such that they lock up and the robot skids. The friction force generated by the skidding tires slows the vehicle to a stop. In simulation, this is implemented by using a proportional controller to set the angular velocity of the rear wheels to zero throughout the maneuver. The vehicle begins the maneuver with an initial velocity V_i. The braking torque is immediately applied, which causes the simulated robot to skid to a stop. The stopping distance is recorded. Typical ADAMS run time for this model on a Pentium III 1000 MHz machine with 512 Mb RAM is about 30 seconds.

4.2.2 Constant-Speed Turning

Constant-speed turning is a fundamental maneuver in high-speed motion on uneven terrain. Trajectory tracking algorithms often employ constant-speed turning under closed-loop control. In a reactive behavior algorithm, a constant-speed turn would be used to quickly avoid a short-range obstacle. See Figure 4.2 for a schematic of this maneuver. On a smooth surface with perfect knowledge of the system parameters, the control command could be applied to result in a prescribed constant-radius turn path.

Due to system and environment uncertainty, the actual path would deviate from the desired path. Therefore, the sensitivity and uncertainty of turning performance to system needs to be investigated.

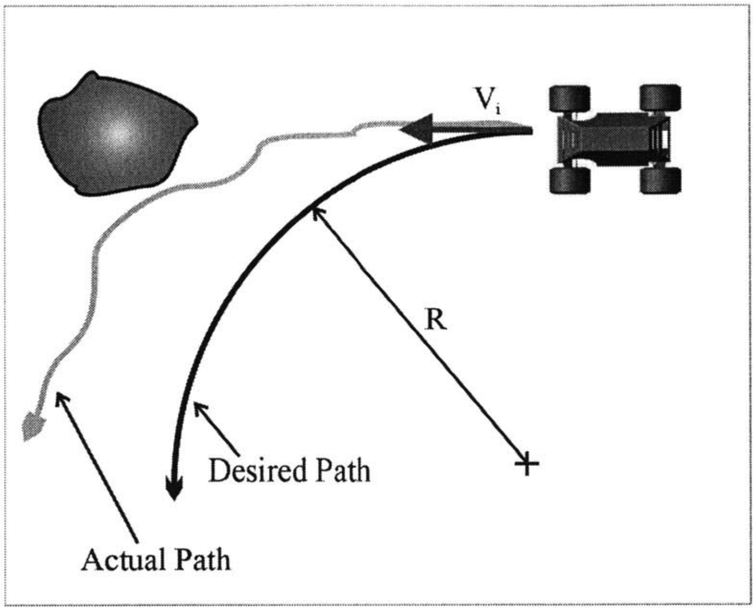

Figure 4.2. Schematic of the high-speed turn simulation.

The high-speed turn is executed by rotating the robot's front wheels while maintaining initial velocity V_i with a proportional controller. The steering angle θ of the front wheels is stepped to the max angle θ_{max} for fixed time. The steering command is a cubic approximation to a step function, shown in Figure 4.3.

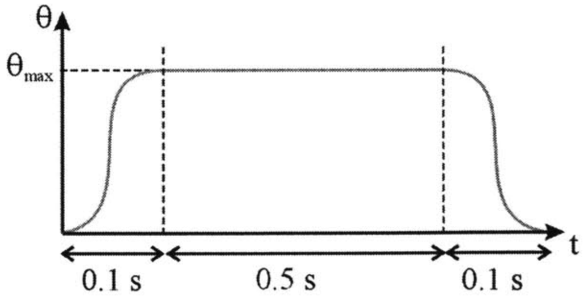

Figure 4.3. Open-loop command for constant radius turn.

The steering command was designed to result in a 90° heading change after a constant radius turn at V_i = 4 m/s. The function is defined for a fixed time so that all paths have approximately the same length. The deviation of an actual rough-terrain path from this "nominal" path is then measured as the performance metric. The j^{th} normalized root-mean-square (RMS) path error is defined as

$$E(j)=\frac{1}{S(j)}\sqrt{\frac{1}{N}\sum_{i=1}^{N}\left(x_{j,i}-\overline{x}_i\right)^2+\left(y_{j,i}-\overline{y}_i\right)^2} \tag{4.1}$$

where $S(j)$ is the length of the j^{th} path, $[x_{j,i}, y_{j,i}]$ is the i^{th} coordinate of the path, $[\overline{x}_i, \overline{y}_i]$ is the i^{th} coordinate of the nominal path, and N is the number of points in the path. The RMS error is normalized by the path-length to formulate an error per unit distance traveled along the turn. Typical ADAMS run time for this model on a Pentium III 1000 MHz machine with 512 Mb RAM is about 45 seconds.

4.3 Sensitivity Analysis

Sensitivity analysis can be used to quantify the relative importance of system parameters in predicting high-speed motion of mobile robots in rough terrain. End users of model-based control and planning algorithms could use this information to optimize modeling strategies for physical systems by appropriately distributing modeling effort.

The system under consideration consists of a mobile robot operating on uneven terrain at high speeds, as discussed in previous chapters. The system parameters of interest include the mass properties of the robot body and tires, stiffness and damping properties of the suspension and tires, ground friction, and terrain roughness. Ground friction was chosen as a representative tire-terrain interaction parameter because of its simplicity, and terrain roughness was selected to describe the geometric nature of the terrain. Terrain roughness is defined in the fractal sense, as described in Section 2.3.2. A summary of the parameters studied in this analysis are presented in the Table 3.1.

Table 4.1. Model Sensitivity Parameters

Parameter	Name	Description
M_v	Body Mass	Mass of the vehicle (without wheels)
I_v	Body Inertias	Inertia of the vehicle (without wheels)
CG_v	Body Center of Mass	Position of the center of mass of the vehicle (no wheels)
M_t	Wheel Mass	Mass of a single wheel
I_t	Wheel Inertias	Inertia of a wheel
K_t	Tire Stiffness	Linear stiffness of the compliant tire
B_t	Tire Damping	Linear damping of the compliant tire
K_v	Suspension Stiffness	Linearized stiffness of the compliant suspension element
B_v	Suspension Damping	Linearized damping of the compliant suspension element
μ	Ground Friction	Coefficient of friction between the tires and ground
D	Terrain Roughness	Fractal dimension of the rough terrain

Several assumptions are made to simplify the analysis and reduce the parameter space. The inertia, center of mass coordinates, and stiffness and damping properties are lumped as single parameters. For example, the stiffness of all independent suspensions are considered as a single parameter, as are the three body center of mass coordinates. The spring and damper values are also assumed linear.

The sensitivity analysis is studied in simulation, using the validated simulation model presented in Chapter 2, and the parameter values of the physical system introduced in Chapter 3.

4.3.1 Sobol Method

Since the maneuvers investigated here are complex and substantially excite the robot dynamics, it is likely that the system parameters interact nonlinearly to affect the resulting motion. Therefore, it is desirable to employ a sensitivity method that makes no assumptions about the model structure. It is also desired to estimate the sensitivity, including nonlinear interaction effects, with a minimal amount of computation. Several sensitivity methods have been developed, including one-at-a-time, sampling, local, variance-based, and graphical methods. A review of sensitivity methods can be found in [Frey, et al, 2002; Saltelli, et al, 2000]. The method selected for this analysis is a variance-based scheme known as the Method of Sobol [Sobol, 1993]. It decomposes functional output variance into components based on Sobol's functional description. The factor sensitivity is then computed from the "partial variances." This method allows models with nonlinear interactions and uses Monte Carlo methods to estimate the total sensitivity of a factor.

The total sensitivity estimate using the Sobol method is more efficient than a full-factorial (brute force) approach for a large number of factors [Saltelli, et al, 2000]. The total number of model evaluations N needed to estimate all the total sensitivity indices using the Sobol method is

$$N = n(k+1) \tag{4.2}$$

where n is the number of samples used to estimate an integral, and k is the number of parameters. In order to estimate the all interactions and nonlinear effects using a full-factorial approach with r levels, the number of model evaluations is

$$N = r^k . \tag{4.3}$$

For good accuracy with the Sobol method, approximately n = 1000 samples should be used. In order to estimate nonlinear effects including interactions with the full factorial approach, at least r = 3 levels should be used. For k = 11 parameters, the total number of model evaluations for each method is

$$N_{Sobol} = 12000$$

$$N_{factorial} = 177147$$

The Sobol method is substantially more efficient in estimating nonlinear and interaction effects than the full-factorial approach for large parameter sets, and makes the analysis computationally feasible.

The Sobol method is based on Sobol's functional decomposition [Sobol, 1967]. For details regarding this method, see Appendix B. The function input factor space is defined over the unit cube, i.e. the region

$$\Omega^k = \left(\mathbf{x} \mid 0 \le x_i \le 1; \quad i = 1, \ldots, k\right). \tag{4.4}$$

where k is the number of parameters, also called factors. The function $f(\mathbf{x})$ is decomposed into summands of increasing dimensionality as follows:

$$f(x_1, \ldots, x_k) = f_o + \sum_{i=1}^{k} f_i(x_i) + \sum_{1 \le i < j \le k} f_{ij}(x_i, x_j) + \cdots + f_{1,2,\ldots,k}(x_1, \ldots, x_k). \tag{4.5}$$

Sobol bases this decomposition on a general representation using multiple integrals, and has shown that it is unique. The variance-based sensitivity indices are derived very naturally from the scheme. The total variance D of $f(\mathbf{x})$ is

$$D = \int_{\Omega^k} f^2(\mathbf{x}) d\mathbf{x} - f_o^{\,2}. \tag{4.6}$$

The partial variances due to each term in (4.5) are computed as

$$D_{i_1,\ldots,i_s} = \int_0^1 \cdots \int_0^1 f^2_{i_1,\ldots,i_s}\left(x_{i_1}, \ldots, x_{i_s}\right) dx_{i_1}, \ldots, dx_{i_s}. \tag{4.7}$$

The sensitivity index for each term in (4.5) is then defined to be

$$S_{i_1,\ldots,i_s} = \frac{D_{i_1,\ldots,i_s}}{D}. \tag{4.8}$$

The sensitivity indices compute the relative importance of a factor, or interaction of factors, as compared to the whole. A complete characterization of the system would require computation of $2^k - 1$ sensitivity indices. However, the total sensitivity index can be defined as the sum of all sensitivity indices involving the factor in question. The total sensitivity index is defined as

$$TS(i) = 1 - \frac{D_{\sim i}}{D} \quad i = 1, \ldots, k \tag{4.9}$$

where $D_{\sim i}$ is the variance compliment to x_i. The total sensitivity index estimates the overall effects of the i^{th} factor, including first and higher order terms. The integrals required to compute the total sensitivity indices are estimated using Monte Carlo integration [Press, et al, 1992]. A total of $k+1$ Monte Carlo integral computations are required, with n model evaluations per integral. For details regarding Monte Carlo estimation of the indices, see Appendix B.

4.3.2 Sobol' Method Validation

The Sobol' method for sensitivity analysis has been validated using a simplified analytical function for the braking maneuver. An analytical model has been derived for the distance required to stop a vehicle by locking the rear wheels. The analytical model assumes a rigid suspension, rigid wheels, flat ground, and continuous ground contact. A diagram of this model is given in Figure 4.4.

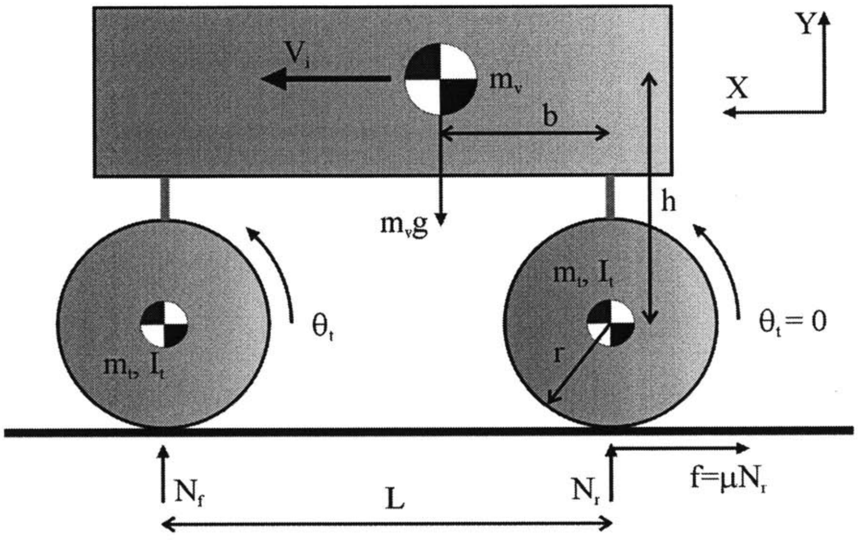

Figure 4.4. Schematic of analytical model for emergency braking.

Appendix B provides a derivation of the stopping distance using this model. The stopping distance is derived as

$$x_{stop} = \frac{V_o^2}{2\mu g\left(m_v + 4m_t\right)}\left(m_v + 4m_t + \frac{2I_t}{r^2}\right)\left(L + \mu\left(r + h\right)\right) \tag{4.10}$$

where V_o is the initial velocity, and μ is the friction coefficient between the tires and ground. The closed form solution depends nonlinearly on several vehicle parameters.

A comparable rigid simulation model was created in ADAMS based on the model described in Chapter 2. Here, the rigid suspension and tires are approximated with stiff linear springs and dampers. The terrain is flat, and rear wheel control is achieved using the method described in Section 4.2.1.

Sobol's method was used to compute total sensitivity in two ways: by evaluating the stopping distance with equation (4.10), and by using the simulation model explained above. Empirical sensitivity indices computed with the analytical and simulation models were then compared. The factors investigated include the vehicle mass, m_v; tires mass, m_t; tire inertia, I_t; and friction coefficient, μ. Upon investigation of equation (4.10), the mass terms drop out of the equation when the angular inertial term is negligible, which is the case here. The resulting function depends only on the initial velocity, friction coefficient, and geometry of the vehicle. Therefore, it is expected that the sensitivity of the mass terms is negligible compared to the total sensitivity of the friction coefficient The sensitivity indices were computed using $n = 1000$ samples per Monte Carlo estimate (see Appendix D). A total of $N = 5000$ model evaluations were required per analysis. The range for each factor was set to 20% of the mean, and the initial velocity was taken as $V_o = 4 \quad m/s$. The total sensitivity indices are plotted in Figure 4.5 for both the analytic and simulation models.

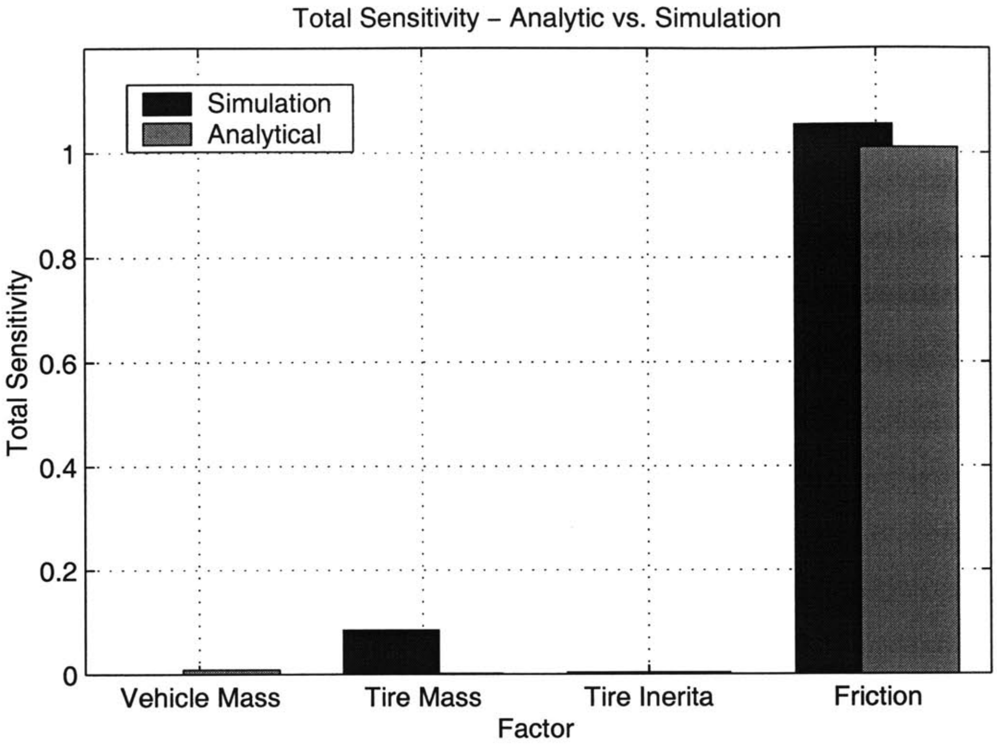

Figure 4.5. Analytic vs. simulation stopping distance total sensitivity estimates.

The results indicate that friction is the most sensitive factor for this model, and that the other factors have negligible sensitivities, as expected. It is also evident that the sensitivity estimates from both models closely match, validating the use of Sobol's method for a simulation-based model. Error in the simulation model estimates is due to inaccuracy of the Monte Carlo integration method.

Convergence of the analytical Sobol' sensitivity indices were investigated as a function of samples per Monte Carlo estimate. Sobol's method was run one hundred times at different Monte Carlo sample sizes. The statistics for each index were computed and plotted for all sample sizes. The statistical boxplots for each index are presented in Figure 4.6. The analytical values for each index are plotted as solid lines.

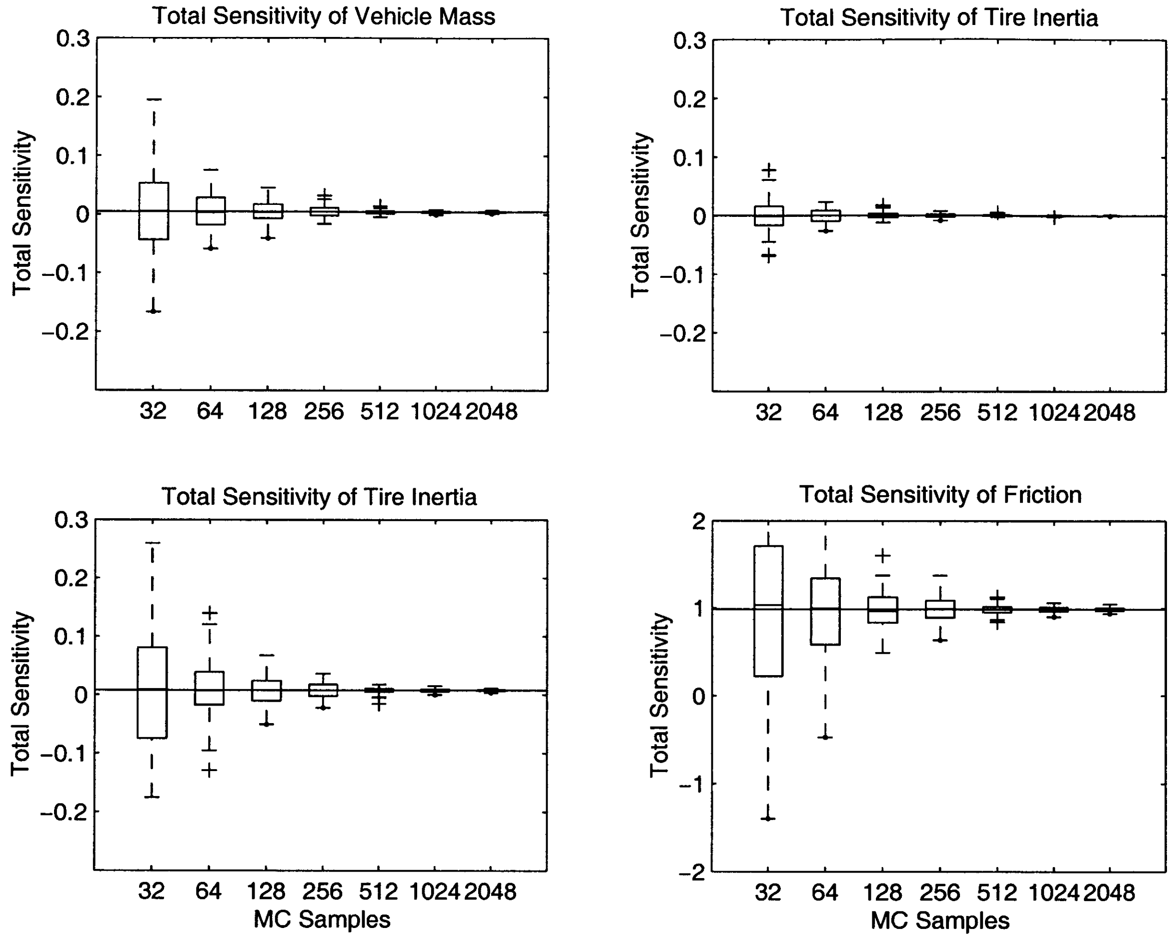

Figure 4.6. Convergence of total sensitivity indices with Monte Carlo sample size.

The results indicate that even at 1000 samples, some error exists. This error leads to the small differences between the simulation and analytical index values plotted in Figure 4.5. However, it is apparent that increasing the sample size beyond 1000 would not dramatically improve accuracy. For practical purposes, a sample size of $n = 1000$ samples was chosen for this analysis, and for the high-speed turn and braking analyses.

4.3.3 Results

Total sensitivity indices of the eleven factors introduced in Section 4.3 were estimated for both the braking and turning maneuvers discussed in Sections 4.2.1 and 4.2.2, respectively. For each maneuver, the Monte Carlo sample size was chosen to be $n = 1000$ for accuracy and computational feasibility. For $k = 11$ factors, a total of $N = 12000$ simulations were run per analysis, requiring approximately 100 hours of computer time on 1000 MHz Pentium III machines. The initial velocity was set to $V_o = 4$ m/s for both maneuvers, and the range for each parameter was taken to be 20% of the mean value. The total sensitivity indices computed for the braking maneuver are presented in Figure 4.7.

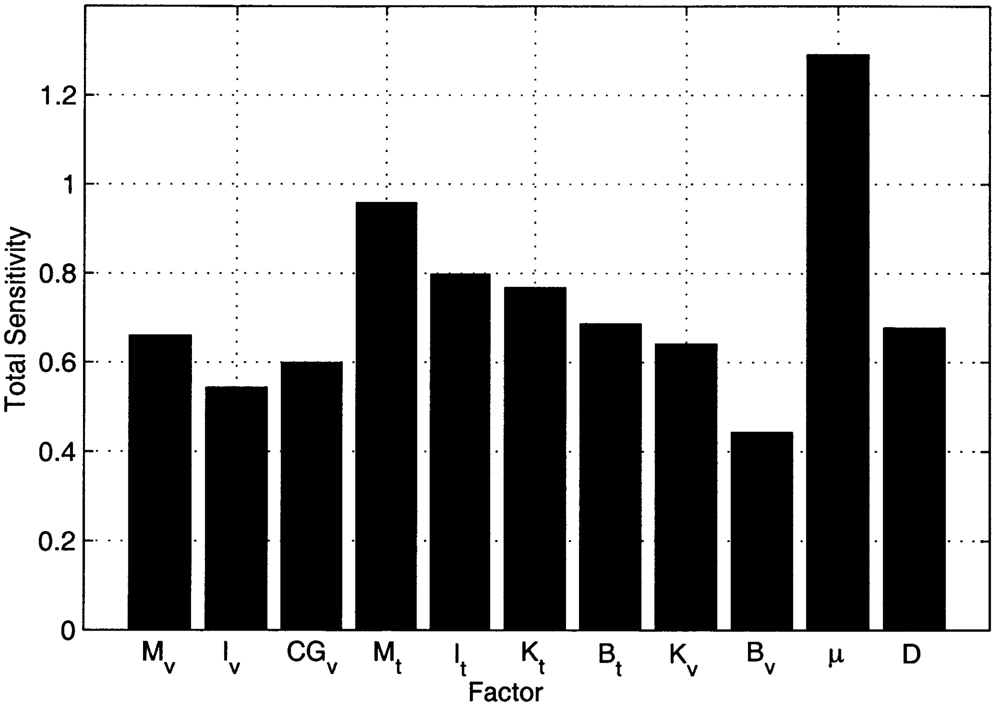

Figure 4.7. Plot of the emergency braking total sensitivity indices.

The total sensitivity indices indicate that tire-ground friction is significantly more sensitive than the other factors. This is expected, as the friction force generated by the sliding tires is the dominant force decelerating the vehicle. Terrain roughness also slows the vehicle with energy absorption through the suspension and tires. This effect is observed in the relatively high sensitivity of the physical tire parameters. Tire mass shows high sensitivity, due to tire ballistic motion through the rough terrain. Tires of lesser mass, for constant suspension stiffness, more closely track undulations in the terrain, while heavier tires tend to remain airborne for a longer time, on average. This effectively limits the friction force acting to decelerate the robot. Tire damping is least sensitive, as variations in the damping value have negligible effects on stopping distance.

In addition, changes in the terrain roughness are only moderately sensitive. This is due to the range assigned for the roughness factor.

The total sensitivity indices computed for the high-speed turning maneuver are presented in Figure 4.8.

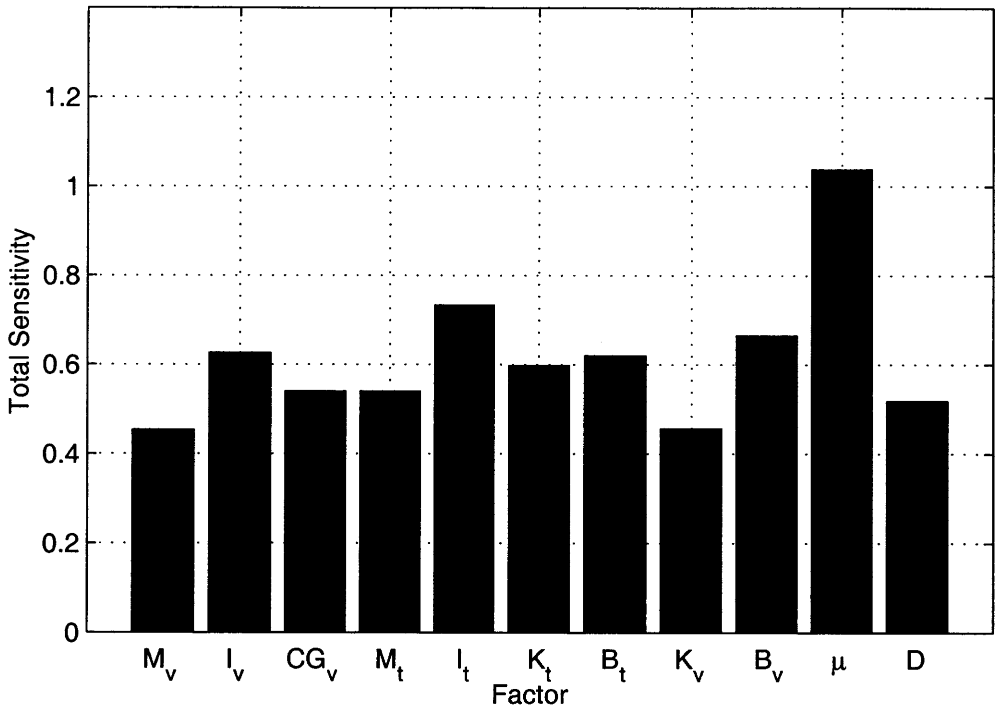

Figure 4.8. High-speed turning total sensitivity indices.

These results again indicate that tire-ground friction is the most sensitive factor. This result is expected because the ground forces generated by the tire are the dominant forces acting to turn the vehicle. The other factors are approximately equally sensitive. The finite precision of the estimates limits comparison of the secondary factors. Overall, it is reasonable to conclude that the tire-terrain interaction parameters are most sensitive in affecting the performance of high-speed maneuvers in rough terrain.

4.4 Uncertainty Analysis

Uncertainty analysis seeks to answer the question: Given uncertainty in the input of a system, what is the uncertainty in output? Here the inputs are system parameters such as inertia and ground friction, and the output is robot response. Planning and control algorithms would use knowledge of system output uncertainty in robust planning and control algorithms. High-speed reactive behaviors will employ this information in the form of vehicle safety margins and maneuver risk assessment.

The analysis presented here investigates the effects of uncertainty on high-speed turning and emergency braking. The same system parameters used for the sensitivity analysis are used in this analysis (see Section 4.3). For this analysis, a normal distribution is assumed for each of the system parameters. This is because physical measurements of such parameters are typically described by normal distributions. The standard deviation of the distributions is prescribed to represent a parameter uncertainty level, and a point in the parameter space is randomly sampled from the distribution. The parameter input sample is randomly sampled to represent noisy physical measurement of the parameters. The simulation model is evaluated for each sample, and an output distribution is formed from the results of many samples. The output uncertainty is measured from the statistics of these distributions. The following sections discuss the methodology and results of this analysis.

4.4.1 Method

The uncertainty analysis method presented here is as follows:

1. Prescribe a normal distribution for each system model parameter with nominal values $\overline{\mathbf{x}}_{in}$ and standard deviation σ_{in}. This is the input parameter space.
2. Randomly sample a set from the input parameter space.
3. Evaluate the simulation model using the parameter set.
4. Repeat Steps 2) and 3) n times to generate an output distribution with n points.
5. Estimate the output distribution 99% confidence interval.
6. Repeat Steps 2) through 5) for six different input standard deviations.
7. Compare the output distributions and plot the input vs. output uncertainty.

In this analysis, the uncertainty of any of the parameter is

$$u = \frac{3\sigma_i}{\overline{x}_i} \tag{4.11}$$

where σ_i is the standard deviation, and $\bar{x}_i$ is the mean of the i^{th} parameter. The uncertainty is taken to be 3-sigma (99% confidence interval) divided by the parameter mean. All parameters are then defined to have the same uncertainty level, which take on the discrete values $u = [0.02, 0.05, 0.1, 0.2, 0.3, 0.5]$. An example of a two dimensional distribution of $n = 1000$ points for the first two parameters listed in Table 4.1 with $u = 0.20$ is presented in Figure 4.9

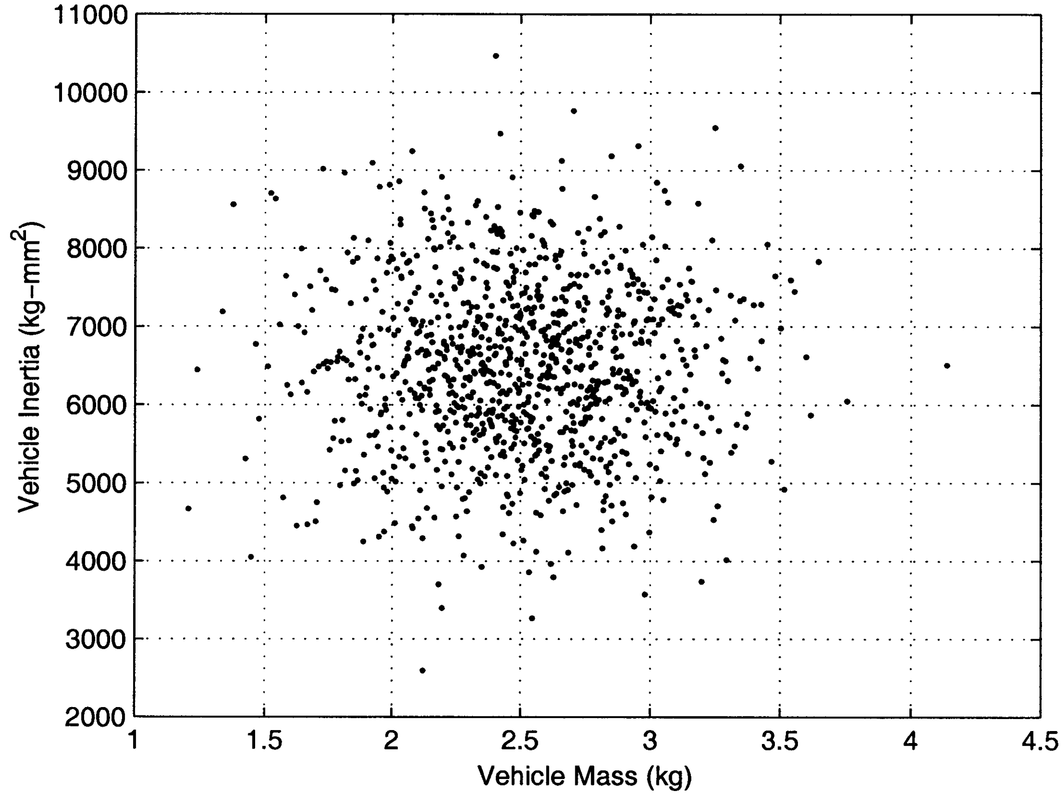

Figure 4.9. Scatter plot of normally distributed mass and inertia parameters.

The high-speed maneuver is simulated for every parameter sample at each uncertainty level, the functional output evaluated, and the resulting distributions are compiled. The 99% confidence output interval is then plotted for the each input uncertainty.

4.4.2 Results

The uncertainty for the emergency braking and constant-speed turning maneuvers was studied in simulation. For both maneuvers, the input parameter space was sampled $n = 1000$ times at six different uncertainty levels, $u = [0.02, 0.05, 0.1, 0.2, 0.3, 0.5]$. A total of 6000 model evaluations per maneuver were computed in simulation, requiring approximately 50 hours of total computer time on a 1000 MHz Pentium III machine. The initial velocity for each trial was V_o = 4 m/s.

The resulting distributions in stopping distance for the braking maneuver are presented for each uncertainty level in Figure 4.10.

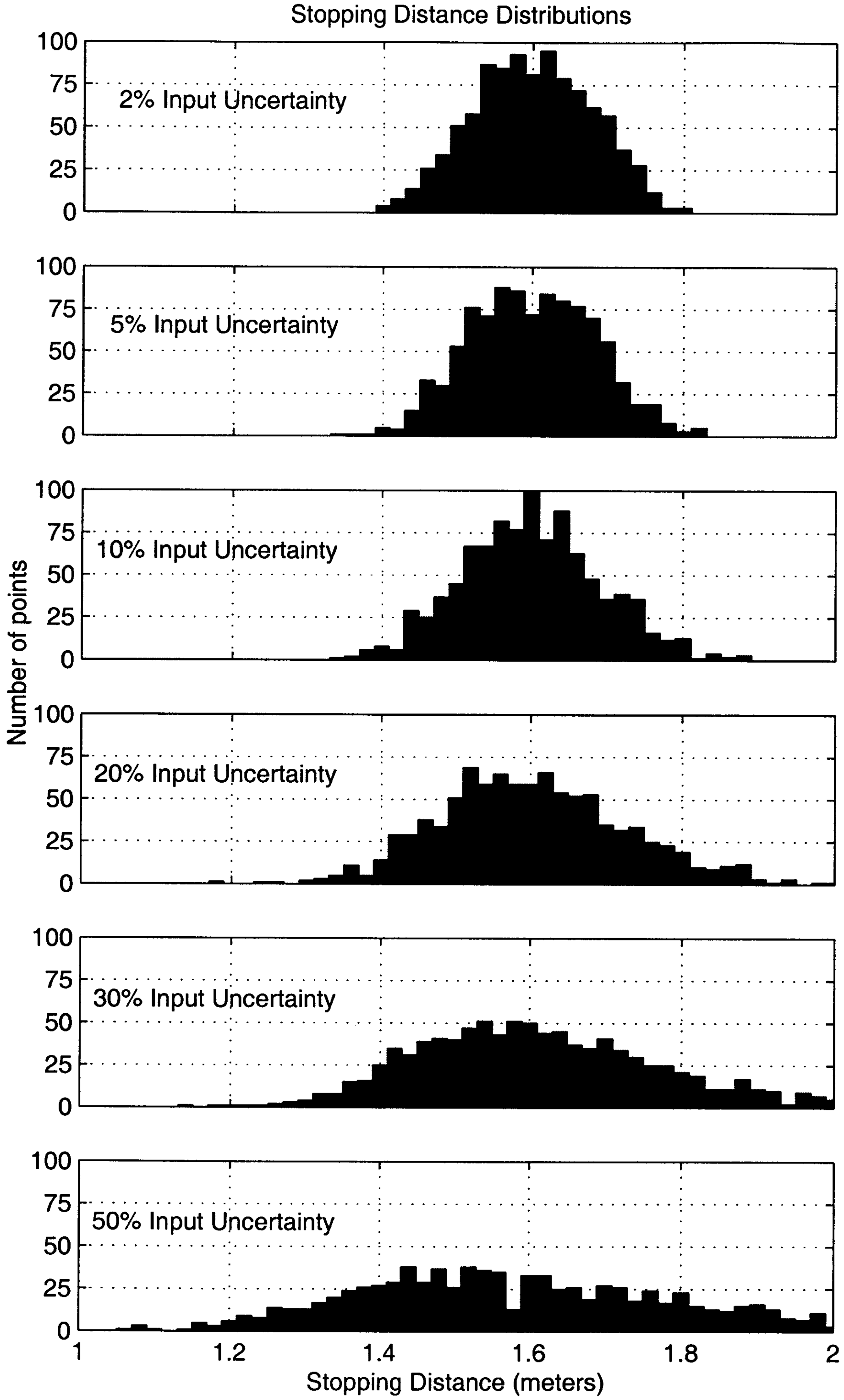

Figure 4.10. High-speed braking stopping distance distributions

The stopping distance distributions are normally distributed. The output normal distributions indicate that the emergency braking maneuver can be approximated as a linear system for the range of values studied here. Although the variance increases with input uncertainty as expected, the distribution width does not approach zero as the input uncertainty vanishes. This is captured in the following figure (Figure 4.11), which plots 3σ (99% confidence) of each distribution as a function of input uncertainty.

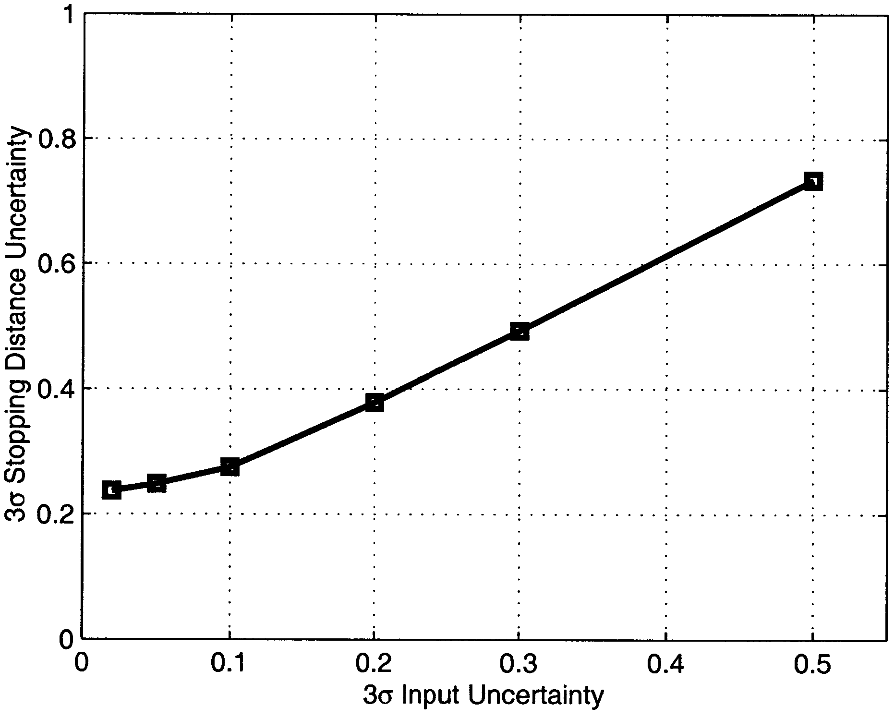

Figure 4.11. Plot of the emergency braking stopping distance uncertainty.

The curve indicates that as system parameter uncertainty approaches zero, the width of the predicted stopping distance distribution approaches a finite-valued asymptote. This can be explained by the statistical nature of the terrain model. In this analysis, the maneuvers were simulated on level, rough terrain generated using fractal techniques. Each sample from the input parameter space contains a new terrain roughness (fractal number), and a new terrain is generated for each model evaluation. The process used to build the fractal terrain generates different terrains even for the same roughness. Therefore, stochastic terrain models such as fractal terrains pose a fundamental limit on braking motion prediction, regardless of the uncertainty in the system model. Extrapolating the curve to zero input uncertainty, the stopping distance in this case can be predicted with maximum accuracy of about 0.25 meters.

In addition to the braking maneuver, a constant-speed turning uncertainty analysis was also performed. The results from the analysis are presented below. To illustrate the variation in turn paths, the trajectories for $n = 1000$ samples with input uncertainty $u = 0.20$ are plotted with the desired, or nominal path. The trajectory plot is shown in Figure 4.12.

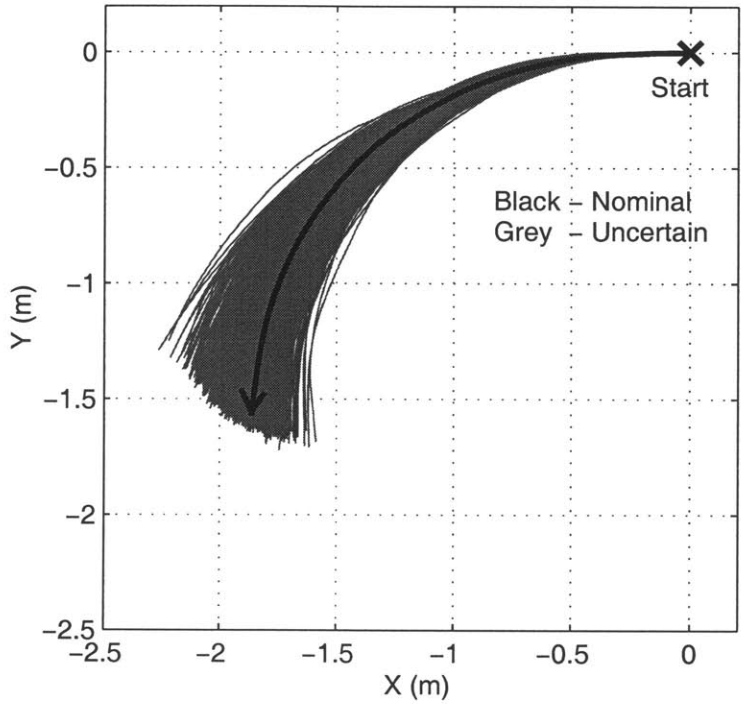

Figure 4.12. Uncertain turn trajectories; n = 1000, u = 0.02.

The uncertain trajectories vary about the nominal path. The resulting distributions in scaled root-mean-square path error for each input uncertainty level are presented in Figure 4.13.

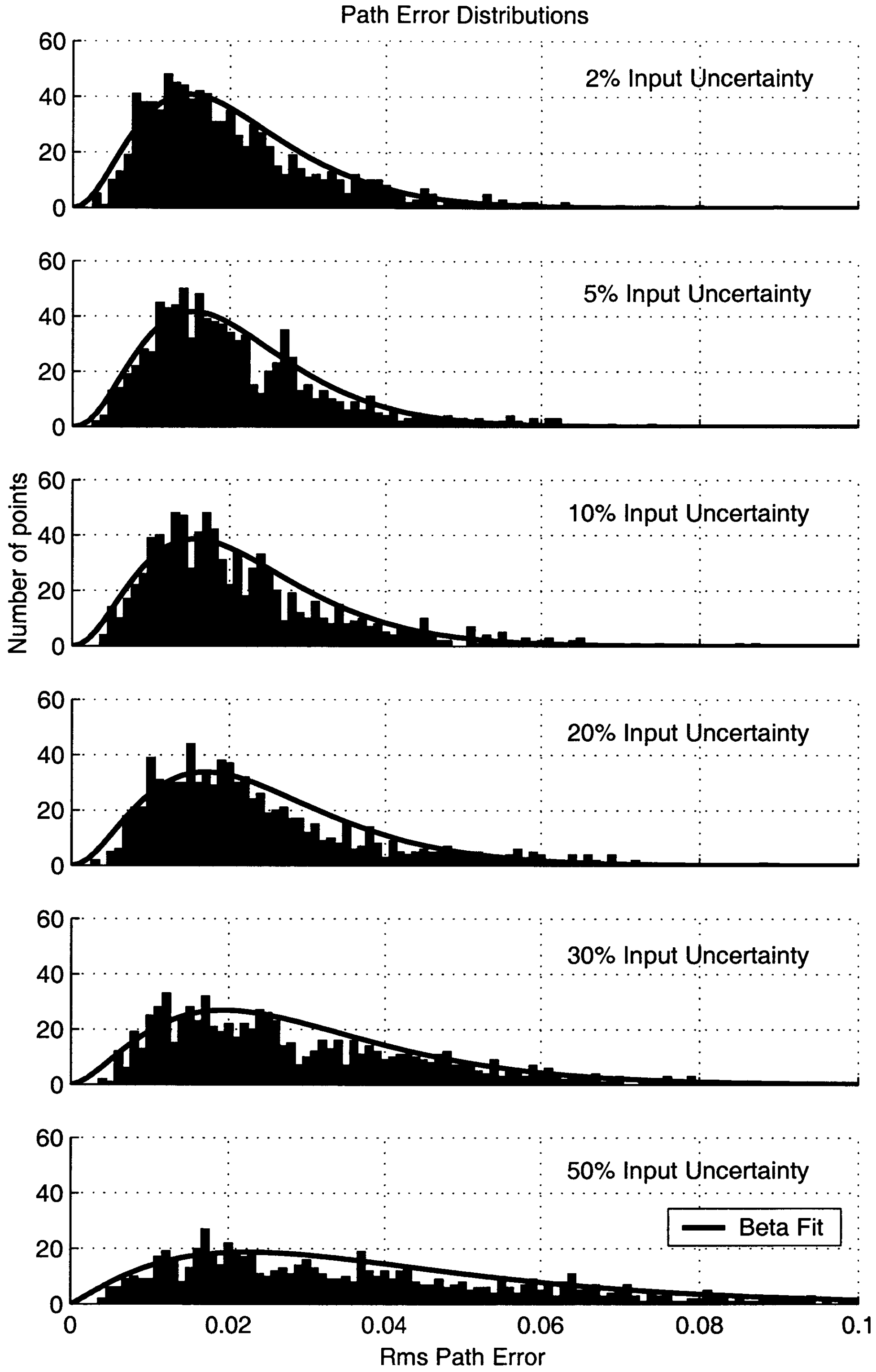

Figure 4.13. High-speed turning path error distributions.

The path error was fit-tested with several different random distributions. The beta random variable was found to best fit the data. This indicates that the turning path error nonlinearly transforms the input normal distributions to output beta distributions. For more information on beta random variables, see [Hahn, et al, 1994]. The fitted Beta distributions are superimposed on the output distributions. As the input uncertainty increases, the distributions tend to increase in width and decrease in peak magnitude. However, the distribution width does not tend toward zero as the input uncertainty vanishes. This is the same phenomenon observed for the braking maneuver. It is captured in Figure 4.14, which plots input uncertainty versus the 99% confidence interval computed from the fit Beta distributions.

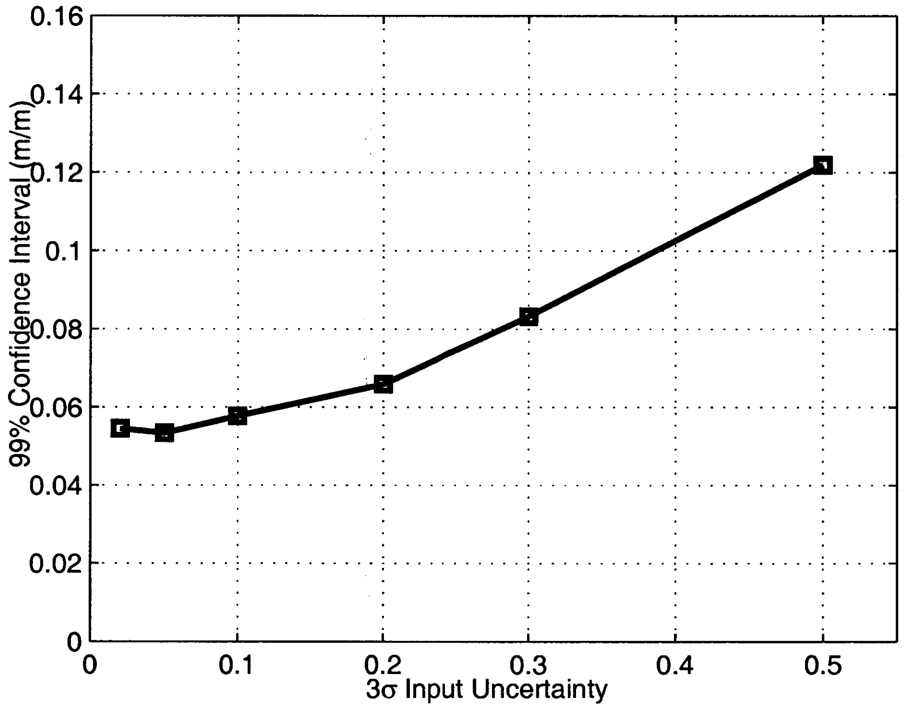

Figure 4.14. High Speed turning path error uncertainty.

The curve indicates that as the system parameter uncertainty approaches zero, the output uncertainty approaches a finite asymptote. Similar behavior was observed for the braking maneuver. Again, the terrain model stochastically changes the terrain shape from sample to sample. Therefore, stochastic terrain models such as fractal terrains pose a fundamental limit on predicting turning motion, regardless of system model uncertainty.

Extrapolating the curve to zero input uncertainty, the path error in this case can be predicted with maximum accuracy of about 0.055 m/m. A deterministic terrain model would not exhibit this property, but would be difficult to realize in natural, uneven terrain.

4.5 Summary

This chapter presented an initial sensitivity and uncertainty analysis for high-speed motion of mobile robots in rough terrain. Constant-speed turning and emergency braking were investigated in simulation using the model discussed in Chapter 2. The method of Sobol was used to estimate the total sensitivity of stopping distance and turn path error to several system parameters. Sobol's method is an efficient technique for estimating sensitivities of many factors, and accounts for interaction and nonlinear effects. The results indicate that tire-terrain interaction parameters, in this case ground friction, are significantly more sensitive than vehicle dynamic parameters and terrain geometry. Uncertainty in predicting high-speed mobile robot motion was also studied in simulation with the same turning and braking maneuvers. The results indicate that prediction uncertainty decreases with system parameter uncertainty. However, it was observed for both maneuvers that prediction uncertainty approaches a finite value as the parameter uncertainty goes to zero. This behavior is due to stochastic nature of the terrain model implemented in this analysis.

CHAPTER

5

CONCLUSIONS AND SUGGESTIONS FOR FUTURE WORK

5.1 Contributions of this Work

This work presented a dynamic model for studying high-speed mobile robots operating in rough terrain, and has investigated the sensitivity and prediction uncertainty of high-speed motion to system parameters.

A simulation-based dynamic model was presented, which includes a tire-ground interaction model, and geometric terrain model. A general, 15 degree-of-freedom vehicle model was introduced. Tire-ground forces were computed with the Magic Formula tire model, and uneven terrain was created from sparse elevation data using a fractal-technique known as the Mid Point Displacement method. The model was implemented in simulation using the ADAMS software package

Experimental validation of the model was presented. A high-speed tele-operated mobile robot was built and used for model validation. The mobile robot was commanded in simulation and experiment to traverse bump and ramp obstacles at various speeds. Vertical and longitudinal acceleration data was then compared. The results indicate that the simulation model accurately predicts high-speed motion over uneven terrain. Small discrepancies between simulation and experiment data were attributed to differences in the velocity control techniques and saturation of the sensor.

A sensitivity analysis of high-speed motion of mobile robots in rough terrain was presented. Constant-speed turning and emergency braking maneuvers were studied in simulation on rough terrain. The method of Sobol' was used to investigate the sensitivity of stopping distance and turning path to uncertainty in system parameters, including mass properties, suspension and tire mechanical properties, and terrain properties. The method was validated using a simplified analytical model. The results from both maneuvers indicate that tire-terrain parameters (the friction coefficient in this case) are substantially more sensitive than all other system parameters. This is justified by the importance of the tire forces in executing high-speed maneuvers.

An uncertainty analysis for prediction of high-speed motion of mobile robots in rough terrain was also presented. For this investigation, constant-speed turning and emergency braking maneuvers were studied in simulation on rough terrain. System parameters were randomly sampled from a normal distribution of prescribed standard deviation, and the model was evaluated. The results indicated that for both maneuvers, the prediction uncertainty decreased with the uncertainty in the system parameters, as expected. However, the prediction uncertainty approached a finite limit as system parameter uncertainty went to zero. This is explained by the stochastic nature of the fractal-based terrain model used in this work.

5.2 Suggestions for Future Work

Over the course of this work, several issues were studied. However, the study was introductory at best, due the complexity of the systems and analysis. For this reason, a more thorough extension of this work would prove worthwhile.

The model validation study should be extended to include out-of-plane motion. This work included only planar motions, but for completeness, maneuvers incorporating yaw or roll dynamics should be investigated. Suggested maneuvers include a hard turn on flat terrain, and a laterally-offset positive obstacle. In addition, a complex motion on unstructured terrain would provide a very convincing argument for the accuracy of the simulation model. The analysis could also be extended by randomly varying the system parameters in simulation according to a measured distribution, and generating a simulation data band rather than a single curve per experiment.

Work should also continue toward developing a more complete and thorough sensitivity analysis of high-speed motion in rough terrain. The presented maneuvers should be studied over a range of velocities and terrain roughness. It would also be practical to examine the sensitivity over various input parameter ranges. A capstone study would examine the sensitivity of system parameters for complex motion on rough terrain under closed-loop control.

The prediction uncertainty analysis was limited in that only a single velocity and roughness were studied. This investigation should be expanded to include more maneuver velocities, different degrees of roughness, and in the case of the turning maneuver, different turn radii. It would also be instructive to individualize the parameter uncertainties based on the physical system. This study should be extended to include other important high-speed behaviors such as ballistic motion. An important aspect to study is the effect of terrain grid spacing on prediction uncertainty. Finally, a good conclusion to the uncertainty analysis would be to study a complex motion on rough terrain under closed-loop control.

REFERENCES

ADAMS version 12.0 Documentation, MSC Software, Inc. 2002.

Arakawa, K. and Krotkov, E. "Fractal Surface Reconstruction for Modeling Natural Terrain." *IEEE Conference on Computer Vision and Pattern Recognition*, June 1993.

Arakawa, K., and Krotkov, E. "Estimating Fractal Dimension from Range Images of Natural Terrain." Technical Report CMU-CS-91-156, School of Computer Science, Carnegie Mellon University, Pittsburgh, PA, July 1991.

Arakawa, K., and Krotkov, E. "Estimating Fractal Dimension from Irregularly Spaced Data." *Proceedings of the 1993 IEEE/RSJ International Conference on Intelligent Robots and Systems*, Yokohama, Japan, July 1993.

Bakker, E., Lidner, L., and Pacejka, H. B. "A New Tire Model with an Application in Vehicle Dynamics Studies." SAE Paper 890087, 1989.

Bakker, E., Nyborg, L., and Pacejka, H. B. "Tire Modeling for Use in Vehicle Dynamics Studies." SAE Paper 870421, 1987.

Ben Amar, F. "Steering Behaviour and Control of Fast Wheeled Robots." *Tenth IEEE Conference on Intelligent Robots and Systems*, Grenoble, France, 1997.

Bratley, P., and Fox, B. L. "Algorithm 659: Implementing Sobol's Quasirandom Sequence Generator." *ACM Transactions on Mathematical Software*, Vol. 14, No. 1, March 1988.

Brayton, R. K., Gustavson, F. G., and Hatchel, G. D. "A New Efficient Algorithm for Solving Differential-Algebraic Systems using Implicit Backward Differentiation Formulas." *Proceedings of the IEEE*, Vol. 60, No. 1, 1972.

Brenan, K. E. Campbell, S. I., and Petzold, L. R. *Numerical Solution of Initial Value Problems in Differential-Algebraic Equations.* Society for Industrial & Applied Mathematics, Philadelphia, PA, 1996.

Campos, J., Davis, L., Lewis, F. L., Ikenaga, S., Scully, S., and Evans, M. "Active Suspension Control of Ground Vehicle Heave and Pitch Motions." *Proceedings of the 7th IEEE Mediterranean Control Conference on Control and Automation*, Israel, June 1999.

Chalasani, R. M., "Ride Performance Potential of Active Suspension Systems – Part I: Comprehensive Analysis Based on a Quarter-Car Model." *Proceedings of the Symposium on Simulation and Control of Ground Vehicles and Transportation Systems*, Anaheim, CA, Dec 1986.

Chalasani, R. M., "Ride Performance Potential of Active Suspension Systems – Part II: Comprehensive Analysis Based on a Full-Car Model." *Proceedings of the Symposium on Simulation and Control of Ground Vehicles and Transportation Systems*, ASME AMD, Anaheim, CA, Dec 1986.

Cunningham, J., Roberts, J., Corke, P., and Durrant-Whyte, H. "Automation of Underground LHD and Truck Haulage." *Proceedings of Australian IMM Annual Conference*, 1998.

DARPA Strategic Plan, 2003. http://www.darpa.mil/body/pdf/DARPAStrategicPlan2003.pdf

De Vries, E. J. H. "Motorcycle Tyre Measurements and Models." *Proceedings of the 15th Symposium on Dynamics of Vehicles on Road and Tracks, IA VSD*, Budapest, August 1997.

DeSantis, R.M. "Path-Tracking for Car-like Robots with Single and Double Steering." *IEEE Transactions on Vehicular Technology*, Vol. 44, No. 2, 1995.

Durrant-Whyte, H. F. "An Autonomous Guided Vehicle for Cargo Handling Applications." *International Journal of Robotics Research*, vol. 15, no. 5, Oct. 1996.

Eicker, P. J. "The Embudito Mission: A Case Study of the Systematics of Autonomous Ground Mobile Robots." Sandia National Laboratories, 2001.

Elbeheiry, E. M., Karnopp, D. C., Elaraby, M. E., and Abdelraaouf, A. M. "Suboptimal Control Design of Active and Passive Suspensions Based on a Full Car Model." *Vehicle System Dynamics*, Vol. 26, 1996.

Fischer, D., Borner, M., and Isermann, R. "Control of Mechatronic Semi-Active Vehicle Suspensions." *Proceedings of the 2nd IFAC Conference on Mechatronic Systems,* Berkeley, CA, December 2002.

Frey, H. C., and Patil, S. R. "Identification and Review of Sensitivity Analysis Methods." *Risk Analysis.* Vol. 22, No. 3, 2002.

Gear, C. V. *Numerical Initial Value Problems in Ordinary Differential Equations.* Prentice-Hall, New Jersey, 1971.

Gear, C. W. "The Simultaneous Solution of Differential Algebraic Systems." *IEEE Transactions of Circuit Theory*, CT-18, No. 1, 1971.

Gerhart, G., Goetz, R., and Gorsich, D. "Intelligent Mobility for Robotic Vehicles in the Army after Next." *Proceedings of the SPIE Conference on Unmanned Ground Vehicle Technology*, Vol. 3693, 1999.

Gillespie, T. D. *Fundamentals of Vehicle Dynamics.* Society of Automotive Engineers, Warrendale, PA, 1992.

Gim, G. "Vehicle Dynamic Simulation with a Comprehensive Model for Pneumatic Tires." PhD Thesis, University of Arizona, 1988.

Golombek, M. P. "Mars Pathfinder Mission and Science Results." *Proceedings of the 29th Lunar and Planetary Science Conference*, 1998.

Gonthier, Y., and Papadopoulous, E. "On the Development of a Real-time Simulator for an Electro-Hydraulic Forestry Machine." *Proceedings of IEEE International Conference on Robotics and Automation*, 1998.

Gordon, T. J., and Sharp, R. S. "On Improving the Performance of Automotive Semi-active Suspensions Through Road Preview." *Journal of Sound and Vibration*, Vol. 217, No. 1, 1998.

Hahn, G. J., and Shapiro, S. S. *Statistical Models in Engineering*. John Wiley and Sons, New York, 1994.

Iagnemma, K., Golda, D., Spenko, M., and Dubowsky, S. "Experimental Study of High-Speed Rough-Terrain Mobile Robot Models for Reactive Behaviors." *Proceedings of the International Symposium on Experimental Robotics*, Italy, 2002.

Ikenaga, S., Lewis, F. L., Campos, J, and Davis, L. "Active Suspension Control of Ground Vehicles Based on a Full-Vehicle Model." *Proceedings of the American Control Conference (ACC)*, Chicago, IL, June 2000.

Julier, S. J. "On the Role of Process Models in Autonomous Land Vehicle Navigation Systems." *IEEE Transactions on Robotics and Automation*, Vol. 19, No. 1, February 2003.

Keller, J., Crownover, R., and Chen, R. "Characteristics of Natural Scenes Related to the Fractal Dimension." *IEEE Transactions on Pattern Analysis and Machine Intelligence*, Vol. 9, No. 5, 1987.

Kelly, A., and Stentz, A. "An Approach to Rough Terrain Autonomous Mobility." *International Journal of Autonomous Robots*, February 1997.

Langer, D., Rosenblatt, J.K., and Hebert, M. "An Integrated System for Autonomous Off-Road Navigation." *Proceedings of the IEEE International Conference on Robotics and Automation*, Vol. 1, May 1994.

Leal, J., Scheding, S., and Dissanayake, G. "Stochastic Simulation in Surface Reconstruction and Application to 3D Mapping." *Proceedings of the 2002 IEEE International Conference on Robotics and Automation*, Washington, D. C, May 2002.

Mandelbrot, B. B. *The Fractal Geometry of Nature*. Freeman and Company, 1977.

Mathews, J. H., and Fink, K. D. *Numerical Methods using Matlab*. 3rd edition. Prentice Hall, New Jersey, 1999.

Maurice, J. P. "Short Wavelength and Dynamic Tyre Behaviour under Lateral and Combined Slip Conditions." Ph.D. Thesis, Delft University of Technology, The Netherlands, 1999.

Meriam, J. L., and Kraige, L. G. *Engineering Mechanics: Dynamics.* 4th edition, Wiley, New York, 1997.

Mortenson, M. E. *Geometric Modeling.* Wiley, New York, 1985.

Mucka, P. "The Influence of Quarter Car Model Parameters on Quality of Active Suspension." *Journal of Mechanical Engineering*, Vol. 51, No. 3, 2000.

National Institute of Standards and Technology Virtual Museum, 2003. http://museum.nist.gov/exhibits/timeline/printerFriendly.cfm?itemId=38

Ohmiya, K. "Fractal Dimensions of Terrain Profiles." *Proceedings of the 10th International Conference of the ISTVS*, Kobe, Japan, August 1990.

Olin, K.E. and Tseng, D.Y. "Autonomous Cross-Country Navigation: An Integrated Perception and Planning System." *IEEE Intelligent Systems*, Vol. 6, No. 4, 1991.

Osborn, J. F. "Applications of Robotics in Hazardous Waste Management." *Proceedings of the SME 1989 World Conference on Robotics Research*, 1989.

Pacejka, H. B. "The Tire as a Vehicle Component." *XXVI FSITA Congress*, Prague, June 1996.

Pai, K. D., and Reissell, L. M. "Multiresolution Rough Terrain Motion Planning." *IEEE Transactions on Robotics and Automation*, Vol. 14, No. 1, February 1998.

Peng, H., and Tomizuka, M. "Preview Control for Vehicle Lateral Guidance in Highway Automation." *ASME Journal of Dynamic Systems, Measurement, and Control*, Vol. 155, 1993.

Pentland, A. "Fractal-Based Description of Natural Scenes." *IEEE Transactions on Pattern Analysis and Machine Intelligence*, Vol. 6, No. 6, 1984.

Pham, H., and Hedrick, J. K. "A Robust Optimal Lateral Vehicle Control Strategy." *Proceedings of the 1996 IEEE International Conference on Control Applications*, Dearborn, MI, September 1996

Press, W. H., Teukolsky, S. A., Vetterling, W. T., and Flannery, B. P. *Numerical Recipes in C: The Art of Scientific Computing.* 2nd ed, Cambridge University Press, 1992.

Rzepniewski, A. "Motion Planning for Kinematically Reconfigurable and High-Speed Mobile Robots in Rough Terrain." M.S. Thesis, Massachusetts Institute of Technology, Cambridge, MA, 2001.

Saltelli, A., Chan, K., and Scott, E. M., editors. *Sensitivity Analysis.* Wiley, New York, 2000.

Scheding, S., Dissanayake, G., Nebot, E. M., and Durrant-Whyte, H. F. "An Experiment in Autonomous Underground Navigation of an Underground Mining Vehicle." *IEEE Transactions on Robotics and Automation*, Vol. 15, February 1999.

Shabana, A. A. *Theory of Vibration: An Introduction.* Springer-Verlag, New York, 1996.

Shiller, Z., and Gwo, Y. "Dynamic Motion Planning of Autonomous Vehicles." *IEEE Transactions on Robotics and Automation*, Vol. 7, No. 2, April 1991.

Shino, M., Miyamoto, N., Wang, Y. Q., and Nagai, M. "Traction Control of Electric Vehicles Considering Vehicle Stability." *Proceedings of the 6th International Workshop on Advanced Motion Control*, 2000.

Shoemaker, C. M., and Borenstein, J. A. "Overview and Update of the Demo III Experimental Unmanned Vehicle Program." *Proceedings of the SPIE Conference on Unmanned Ground Vehicle Technology II*, Vol. 4024, 2000.

Sloyom, S., and Rantzer, A. "ABS Control – A design Model and Control Structure." In *Nonlinear and Hybrid Control in Automotive Applications*, Spring Verlag, 2002.

Sobol', I. M. "On the Distribution of Points in a Cube and the Approximate Evaluation of Integrals." *USSR Comput. Maths. Math. Phys.* Vol. 7, 1967.

Sobol', I. M. "Sensitivity Analysis for Non-Linear Mathematical Models." *Math. Model. Comput. Exp.* Vol. 1, 1990.

Spenko, M. "Planning and Control of a High-Speed Rough-Terrain Autonomous Vehicle." Ph.D. Thesis Proposal, Massachusetts Institute of Technology, Cambridge, MA, 2003.

TACOM Mission, 2003. http://www.tacom.army.mil/what_do.htm

Talukder, A., Manduchi, R., Castano, K., Owens, L., Matthies, L., Castano, A., and Hogg, R. "Autonomous Terrain Characterisation and Modeling for Dynamic Control of Unmanned Vehicles." *IEEE IROS 2002*, Switzerland, September 2002.

Van Bokhoven, W. M. G. "Linear Implicit Differentiation Formulas of Variable Step and Order." *IEEE Transactions on Circuits and Systems*, Vol. 22, No. 2, 1975.

Voss, R. "Random Fractal Forgeries." In *Fundamental Algorithms for Computer Graphics.* R. Earnshaw, Editor, Springer-Verlag, Berlin, 1985.

Voss, R.F. "Random fractals: Self-affinity in Noise, Music, Mountains and Clouds." *Physica D (Non-linear Phenomena): Fractals in Physics*, Vol. 88, 1989.

Wielenga, T. "The Effect of Numerical Stiffness on Mechanism Simulations." *Proceedings of the 1986 International Computers in Engineering Conference*, Vol. 1, 1986.

Zegelaar, P. W. A. "The Dynamic Response of Tyres to Brake Torque Variations and Road Unevenesses." Ph.D. Thesis, Delft University of Technology, The Netherlands, 1998.

APPENDIX

A

PARAMETER IDENTIFICATION

This Appendix presents the methods and results of the experimental parameter identification of the mobile robot described in section 3.2.1. The system parameters include robot body and wheel masses, robot body center of mass, robot body moment of inertias, wheel moment of inertias, effective suspension stiffness and damping, and tire stiffness and damping normal to the road surface.

A.1 Mass Properties

The robot body mass, center of mass, moments of inertia, and wheel mass and moment of inertia were determined experimentally. The robot body and wheel masses were measured using a digital scale. The masses are presented in Table A.1.

Table A.1. Mass properties.

Component	Mass (kg)
Body	2.31
Wheels (each)	0.196

A.1.1 Center of Mass

The body center of mass was computed by elevating part of the robot, measuring the normal force at the wheel axles with a scale, measuring the inclination angle, and solving the equations of static equilibrium. To compute the location in 3-axis, three configurations are needed: the front two wheel axles elevated at two different heights, and the side two wheel axles elevated. These configurations are shown in Figure A.1

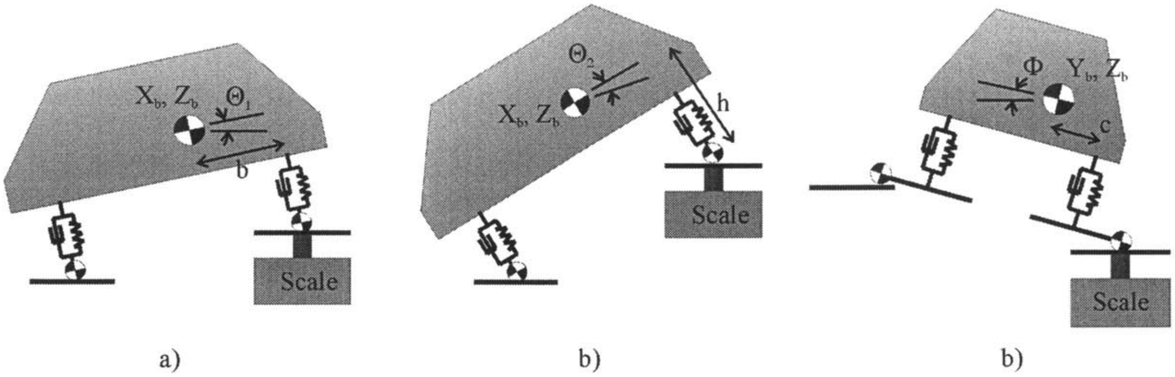

a) b) b)

Figure A.1. Schematic of experiment configurations to determine a) the longitudinal, b) vertical, and c) transverse center of mass coordinates.

The three static equilibrium equations to be solved are then

$$\begin{bmatrix} -mg\cos\Theta_1 & mg\sin\Theta_1 & 0 \\ -mg\cos\Theta_2 & mg\sin\Theta_2 & 0 \\ 0 & -h\tan\Phi & 1 \end{bmatrix} \begin{bmatrix} b \\ h \\ c \end{bmatrix} = \begin{bmatrix} -m_{s,1}gL\cos\Theta_1 \\ -m_{s,2}gL\cos\Theta_2 \\ w\left(1-m_{s,3}g/mg\right) \end{bmatrix} \tag{A.1}$$

where m is the mass of the robot without wheels, $m_{s,1}$, $m_{s,2}$, $m_{s,3}$ are the measured scale masses for each configuration, L is the wheelbase of the robot, w is the tip-tip axle width, Θ_1 and Θ_2 are the pitch inclination angles for the first two configurations, and Φ is the roll inclination angle for the last configuration. The longitudinal, vertical, and transverse center of mass coordinates b, h, and c are computed by solving equation (A.1). The inclination angles were measured using an inclinometer. The resulting values are given in Table A.2.

Table A.2. Center of mass coordinates.

Center of Mass Coordinate	Distance (m)
b	0.122
h	0.12
c	0.067

A.1.2 Moment of Inertias

The moment of inertia of the robot body and wheels were experimentally determined by hanging them from a metallic cable, and measuring the frequency of angular oscillation of the component. Figure A.2 shows a schematic of the experimental setup to measure the body moment of inertias.

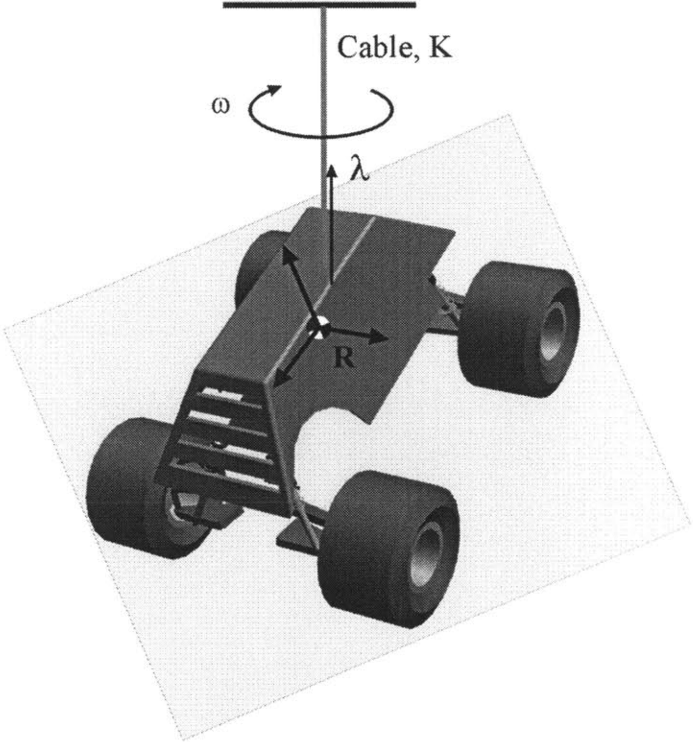

Figure A.2. Schematic of the moment of inertia experiments.

The body oscillates about the axis $\boldsymbol{\lambda}$ in the robot inertial frame $\boldsymbol{R}$ with an angular frequency ω. The cable has rotational stiffness K. The rotation axis in the robot frame is defined as

$$\boldsymbol{\lambda} = l\mathbf{i} + m\mathbf{j} + n\mathbf{k}\,. \tag{A.2}$$

The moment of inertia about the $\boldsymbol{\lambda}$ axis can be computed with the following relation [Meriam, et al, 1997]:

$$I_\lambda = I_{xx}l^2 + I_{yy}m^2 + I_{zz}n^2 - 2I_{xy}lm - 2I_{xz}nl - 2I_{yz}mn \tag{A.3}$$

The moment of inertia about the λ axis can be computed by measuring the period of oscillation T of the hanging body about the axis of the cable:

$$T = 2\pi\sqrt{I_\lambda / K}\,. \tag{A.4}$$

where K is the linear rotational stiffness of the cable. The stiffness was measured using a simple proof mass of calculable rotational inertia. Rotational damping is neglected. It is then possible to compute the inertias in the robot frame by measuring the moment of inertia about six arbitrary axis of rotation. These axes are defined by hanging the robot body from six different cable mount locations. Combining equations (A.3) and (A.4), the equation for the body inertia is then

$$\begin{bmatrix} l_1^2 & m_1^2 & m_1^2 & -2l_1m_1 & -2l_1n_1 & -2m_1n_1 \\ l_2^2 & m_1^2 & m_1^2 & -2l_1m_1 & -2l_1n_1 & -2m_1n_1 \\ l_3^2 & m_1^2 & m_1^2 & -2l_1m_1 & -2l_1n_1 & -2m_1n_1 \\ l_4^2 & m_1^2 & m_1^2 & -2l_1m_1 & -2l_1n_1 & -2m_1n_1 \\ l_5^2 & m_1^2 & m_1^2 & -2l_1m_1 & -2l_1n_1 & -2m_1n_1 \\ l_6^2 & m_1^2 & m_1^2 & -2l_1m_1 & -2l_1n_1 & -2m_1n_1 \end{bmatrix} \begin{bmatrix} I_{xx} \\ I_{xx} \\ I_{xx} \\ I_{xx} \\ I_{xx} \\ I_{xx} \end{bmatrix} = \begin{bmatrix} K\left(T_1/2\pi\right)^2 \\ K\left(T_1/2\pi\right)^2 \\ K\left(T_1/2\pi\right)^2 \\ K\left(T_1/2\pi\right)^2 \\ K\left(T_1/2\pi\right)^2 \\ K\left(T_1/2\pi\right)^2 \end{bmatrix} \tag{A.5}$$

The robot body was hung from each of the four wheel axles and two arbitrary positions on the body. The direction of the axis of rotation was determined from the geometry of the mount points relative to the center of mass. The period of oscillation was then measured for each configuration. Equation (A.5) was then solved for the inertia values. The resulting inertia tensor is

$$I_v = \begin{bmatrix} 0.0220 & -0.0002 & 0.0022 \\ -0.0002 & 0.0065 & 0.0030 \\ 0.0022 & 0.0030 & 0.0230 \end{bmatrix} kg \cdot m^2\,. \tag{A.6}$$

Similarly, the inertia tensor of an individual wheel was determined to be

$$I_w = \begin{bmatrix} 0.0003 & 0 & 0 \\ 0 & 0.0003 & 0 \\ 0 & 0 & 0.0004 \end{bmatrix} kg \cdot m^2 \tag{A.7}$$

A.2 Suspension Properties

The effective spring and damping relations for each independent suspension were determined experimentally. The methodology and results are presented below.

A.2.1 Suspension Stiffness

The stiffness of each independent suspension was measured experimentally. The four-bar suspension was modeled as a parallel, four-bar mechanism mounted on the vehicle chassis with revolute joints and torsion spring-damper. Figure A.3 shows a diagram of this model. The wheel is mounted at the end of the four-bar mechanism.

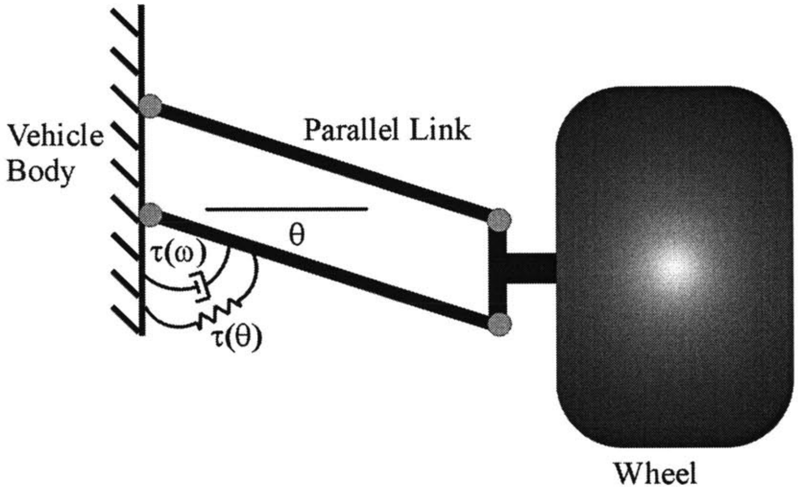

Figure A.3. Schematic of the suspension system model.

The functional relationship for the torsion spring was determined experimentally by loading the suspension at the wheel mount point with a known force, and measuring the resulting angle, θ with an optical encoder. A diagram of the experimental setup is shown in Figure A.4.

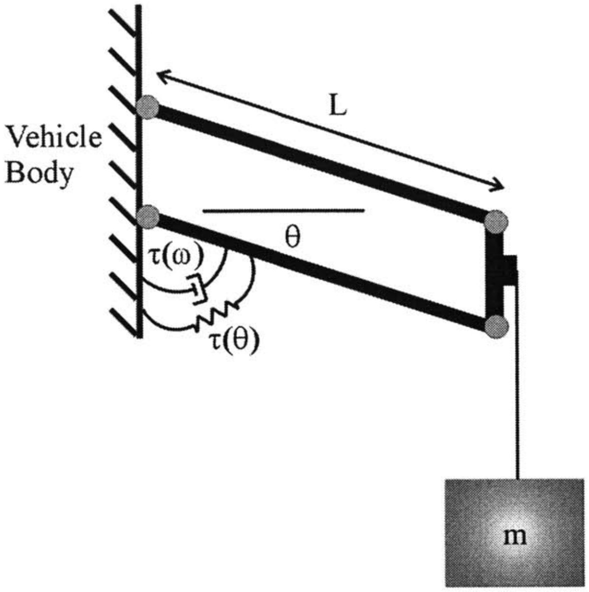

Figure A.4. Schematic of the suspension stiffness experiment.

Several different masses were statically hung at the tip of the suspension, and the angular displacements were measured. Neglecting the mass of the suspension, the spring-torque equation for static equilibrium is

$$\tau(\theta) = mgL\cos\theta \tag{A.8}$$

The experiment was repeated three times for each suspension. The resulting data is presented in Figure A.5, Figure A.6, Figure A.7, and Figure A.8.

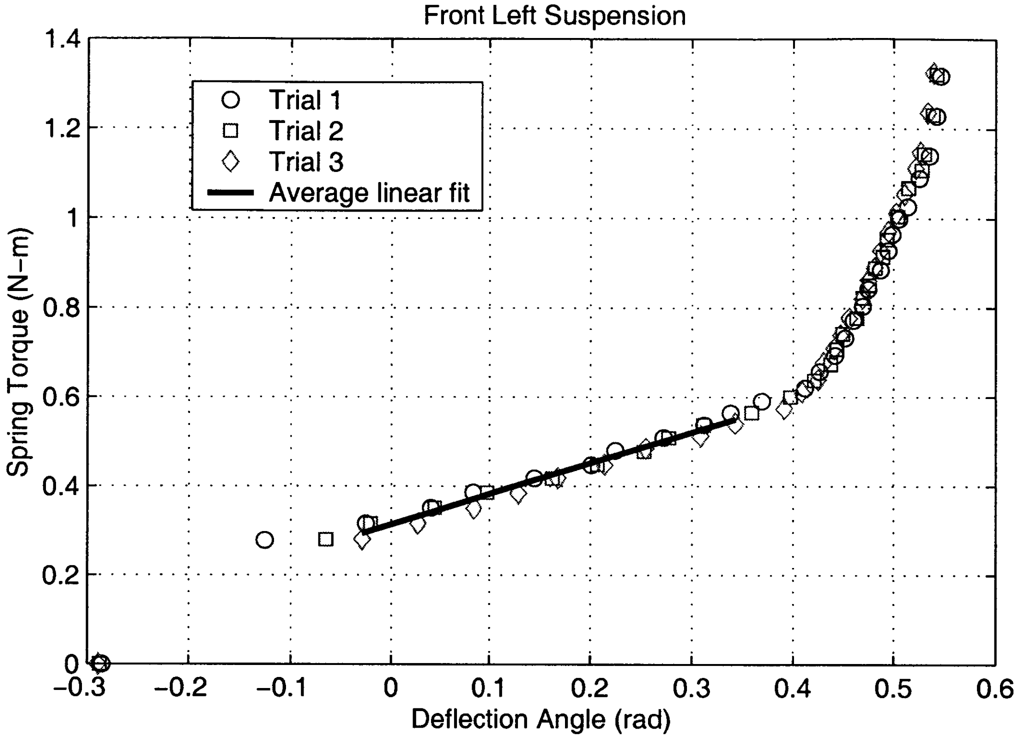

Figure A.5. Spring torque curve for the front left suspension assembly.

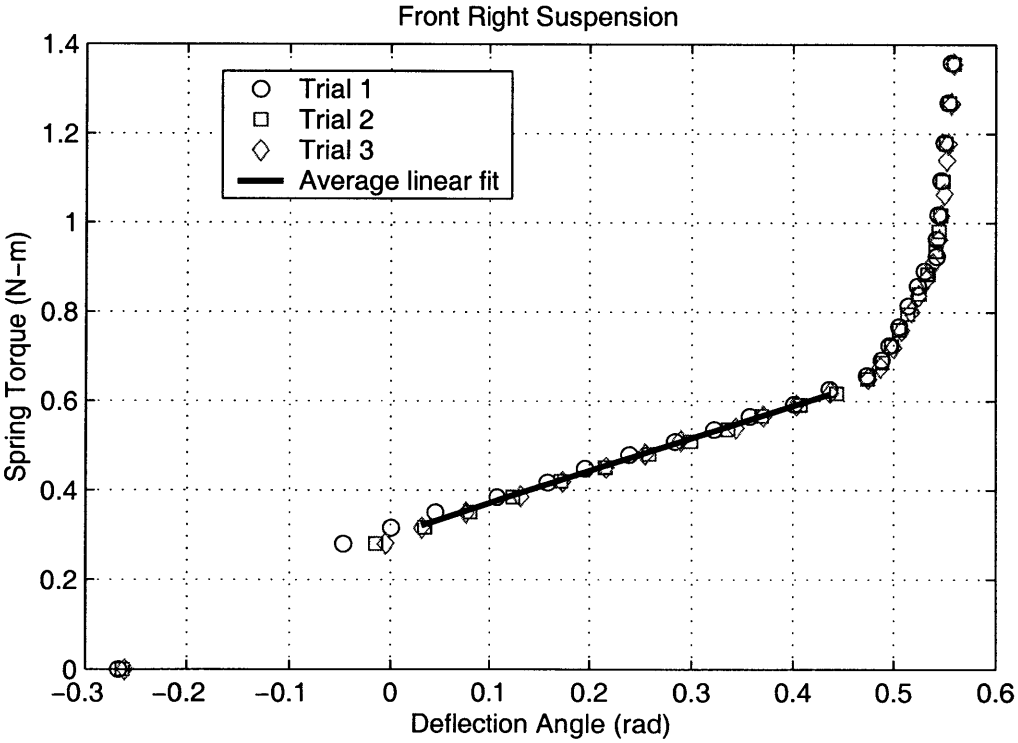

Figure A.6. Spring torque curve for the front right suspension assembly.

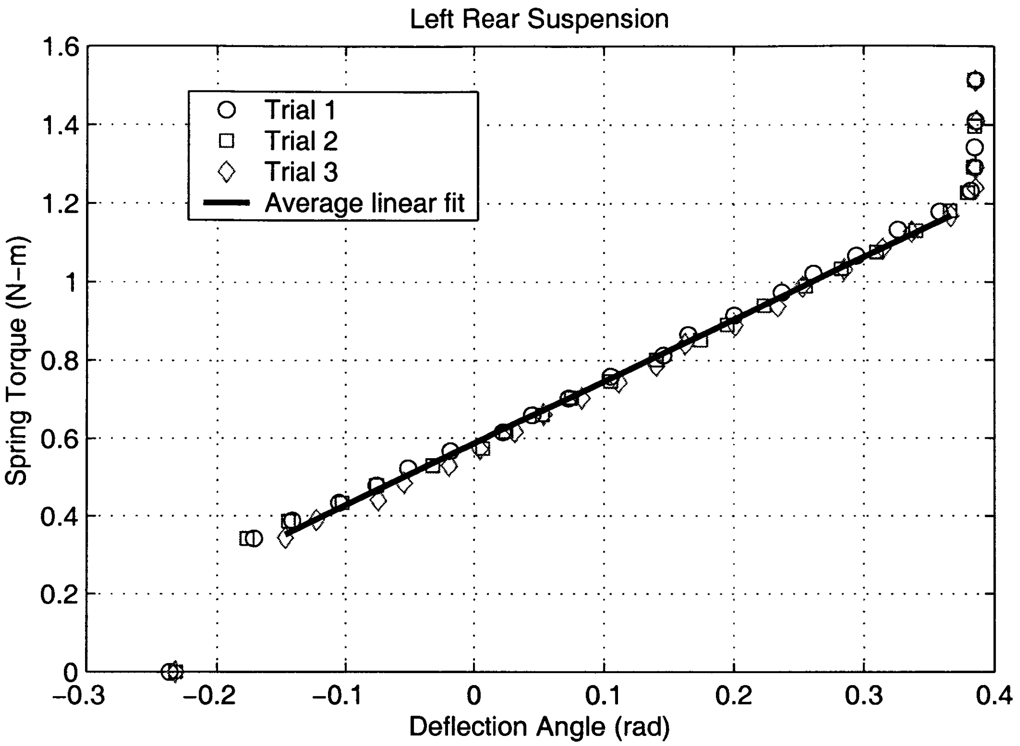

Figure A.7. Spring torque curve for the rear left suspension assembly.

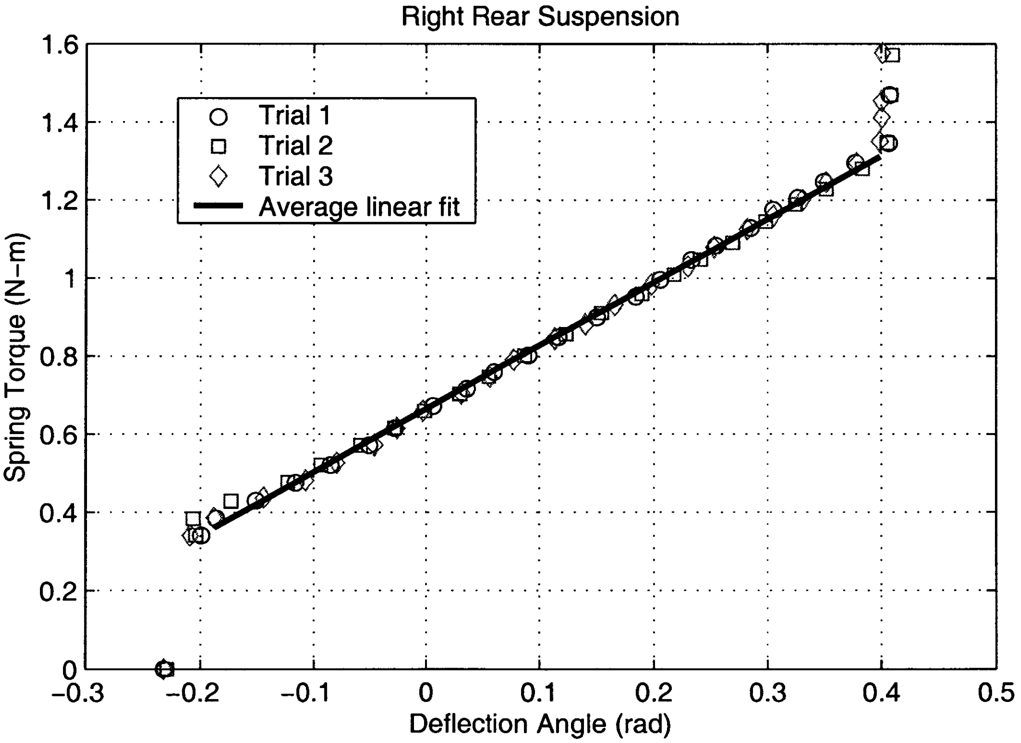

Figure A.8. Spring torque curve for the rear right suspension assembly.

The torsion stiffness curves are very linear through the range of motion. The nonlinearity at large displacements is due to bending of the suspension links after the spring reached full compression. Table A.3 summarizes the linear stiffness coefficients for each of the suspensions.

Table A.3. Suspension assembly spring coefficients.

Suspension	Linear Stiffness K (N·m/rad)
Front Left	0.69
Front Right	0.73
Rear Left	1.59
Rear Right	1.62

A.2.2 Suspension Damping

The functional relation for the suspension damping as depicted in Figure A.3 was determined experimentally. The suspension is overdamped, so techniques such as logarithmic decrement are not applicable. The setup is shown in Figure A.4, with the spring removed. A mass was hung at the axle tip, the system released from rest, and the angle $\theta(t)$ was measured for the duration of the motion. This was repeated several times for different hanging masses. The dynamic equation of motion for the system is

$$\tau\left(\dot{\theta}\right) = ml\cos\theta\left(g - L\cos\theta\ddot{\theta} + L\sin\theta\dot{\theta}^2\right) \qquad \text{(A.9)}$$

where $\tau\left(\dot{\theta}\right)$ is the torsion damping. The angle θ was measured with an optical encoder for all t, while the angular velocity $\dot{\theta}$ and angular acceleration $\ddot{\theta}$ were computed using centered difference formulas [Mathews, et al, 1999]. The torque was computed for each mass trial at the maximum angular velocity so that the acceleration term goes to zero. The torque-velocity curves were generated using this method, and are shown for each suspension in Figure A.9, Figure A.10, Figure A.11, and Figure A.12.

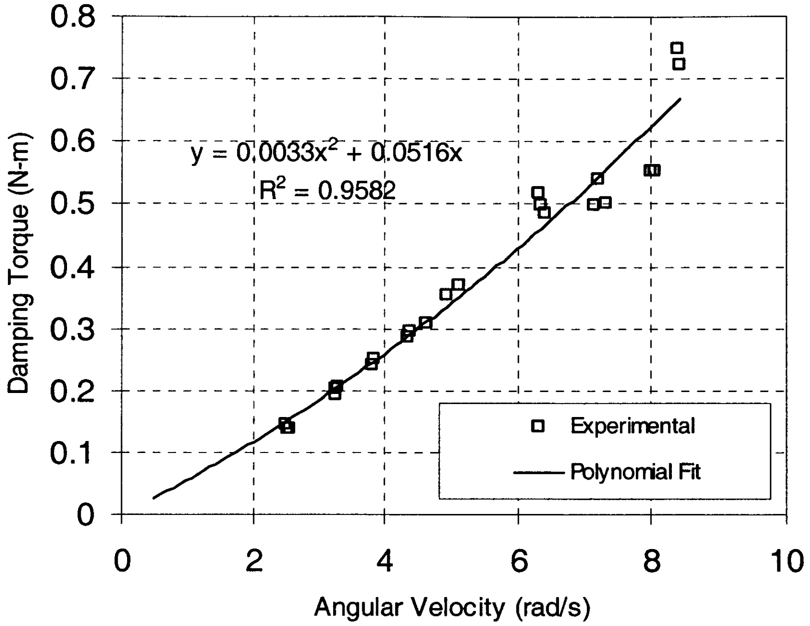

Figure A.9. Damping torque curve for the front left suspension assembly.

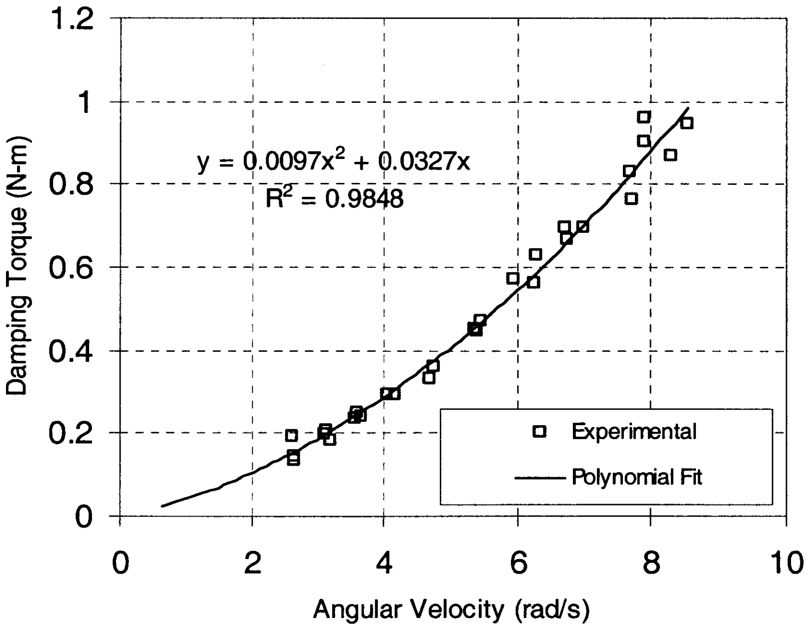

Figure A.10. Damping torque curve for the front rear suspension assembly.

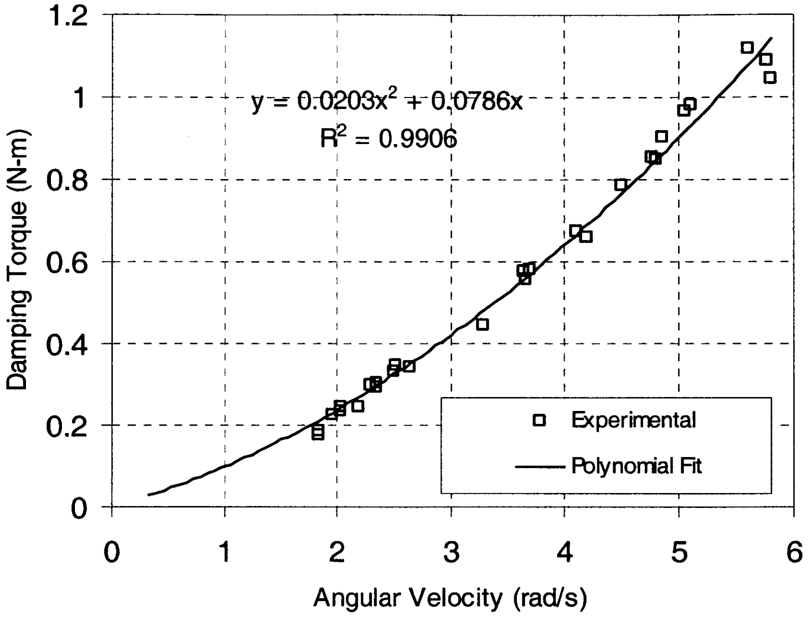

Figure A.11. Damping torque curve for the rear left suspension assembly.

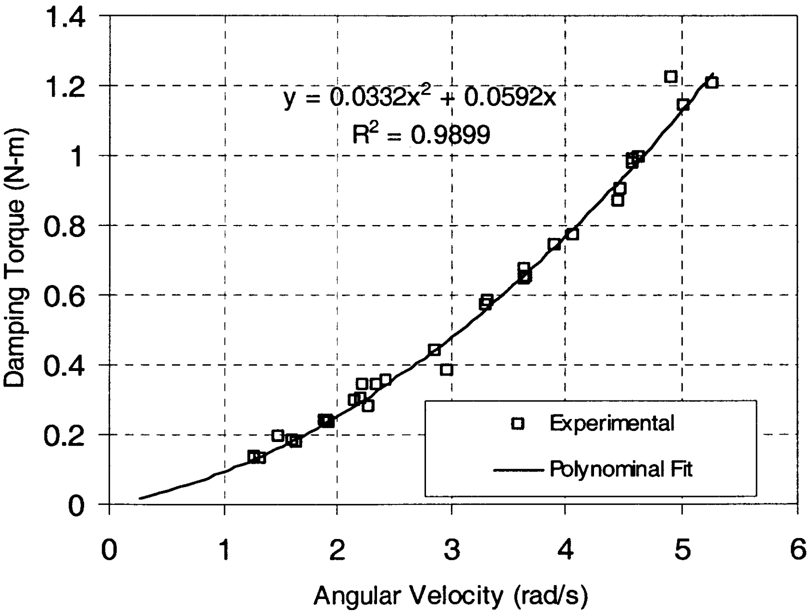

Figure A.12. Damping torque curve for the rear right suspension assembly.

A.3 Tire Properties

The stiffness and damping properties normal to the road surface for two tires were determined experimentally. The methodology and results are presented below.

A.3.1 Tire Stiffness

Tire stiffness normal to the surface was determined experimentally for two of the tires. The wheel was placed on a flat surface with the suspension spring and damper removed, and the axle was loaded with several hanging masses. The tire deflection was determined by measuring the suspension state with an optical encoder. The displacement was then computed from the geometry. A diagram of this setup is shown in Figure A.13.

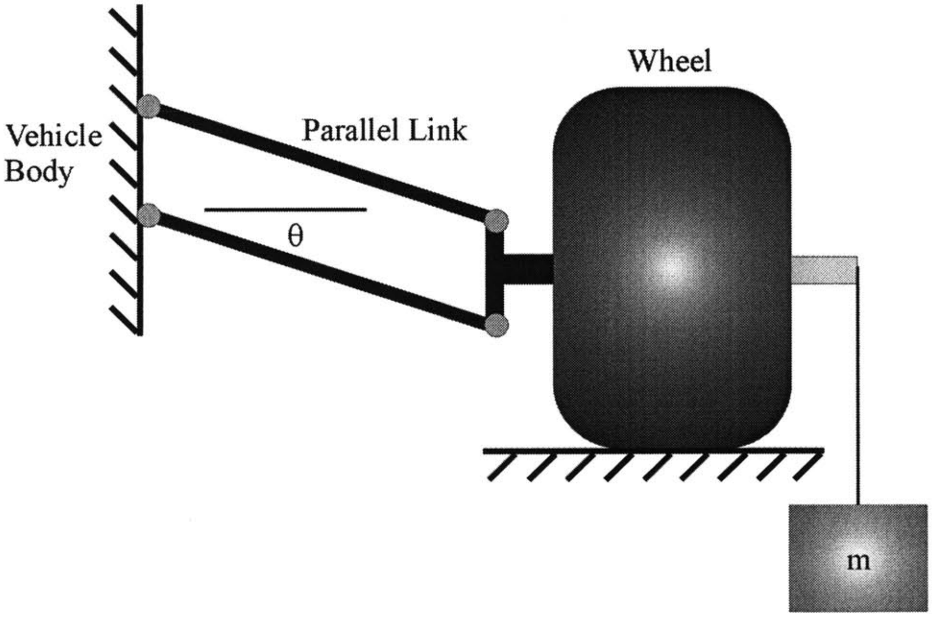

Figure A.13. Schematic of the tire stiffness experiment.

The resulting data is presented in Figure A.14 and Figure A.15 for the front left and rear right tires, respectively.

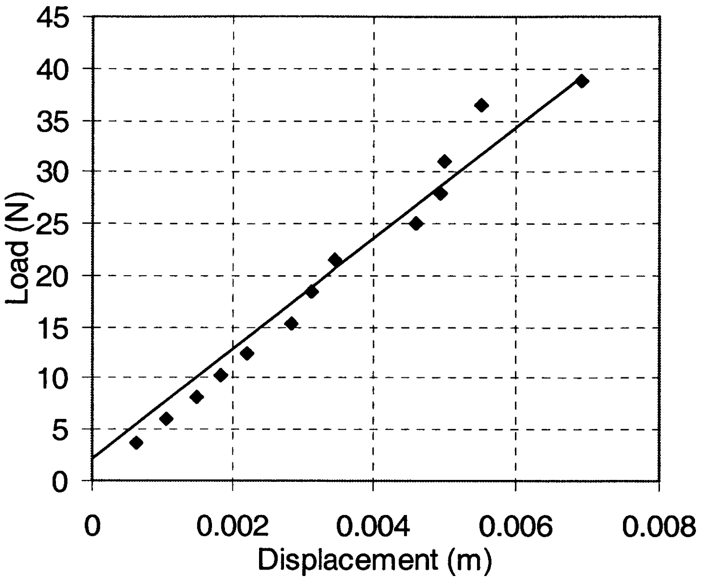

Figure A.14. Front left tire stiffness curve.

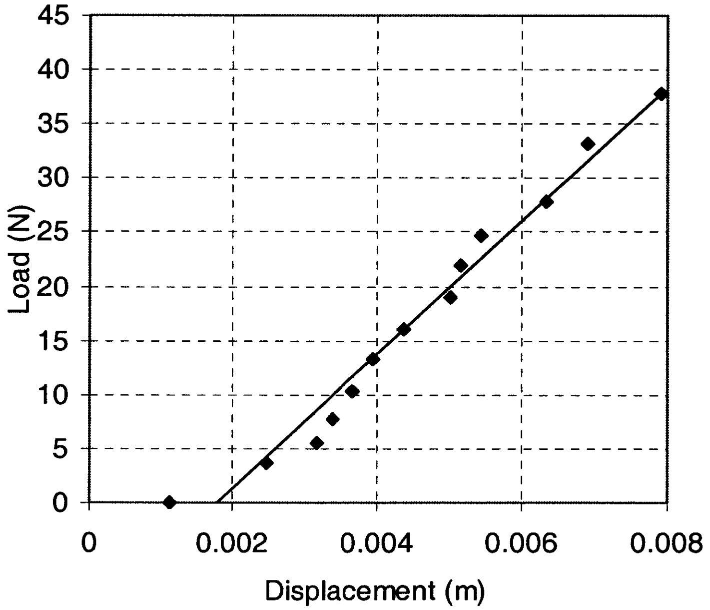

Figure A.15. Rear right tire stiffness curve.

The stiffness values are summarized in Table A.4.

Table A.4. Summary of the tire stiffness coefficients.

Tire	Stiffness (N/m)
Front Left	5344
Rear Right	6183

A.3.2 Tire Damping

The tire damping was determined from the dynamic response of the tire and hung mass to an impulse input. The tire and hanging mass as shown in Figure A.13 were released from a height above the surface. The underdamped dynamic response was recorded with an optical encoder, and the vertical tire displacement was computed from the geometry. This procedure was repeated for several hung masses. The damping coefficient was then computed using logarithmic decrement [Shabana, 1996] for each trial, and averaged. The logarithmic decrement is

$$\delta = \ln \frac{x_i}{x_{i+1}} \tag{A.10}$$

where x_i and x_{i+1} are successive peak amplitudes. The damping factor is computed from the logarithmic decrement by

$$\zeta = \frac{\delta}{\sqrt{(2\pi)^2 + \delta^2}}. \tag{A.11}$$

The damping coefficient is then computed from the damping factor, measured spring coefficient and sprung mass:

$$b = 2\zeta\sqrt{km} \tag{A.12}$$

The resulting damping coefficients for the front left tire and rear right tire are given in Table A.5.

Table A.5. Summary of the tire damping coefficients.

Tire	Damping Coefficient (N·s/m)
Front Left	17.3
Rear Right	18.9

A.4 Accelerometer and Datalogger Specifications

The technical specifications for the Crossbow CXL04M3 three-axis accelerometer and the Pace Scientific XR440-M Pocket Logger are presented in Table A.6 and Table A.7, respectively.

Table A.6. Specifications for the Crossbow CXL04M3 accelerometer.

Specification	Value	Units
Input Range	±4	g
Sensitivity	500	mV/g
Non-linearity	0.2	% FS
Noise	10	mg rms
Bandwidth	DC-100	Hz

Table A.7. Specifications for the Pace Scientific XR440-M Pocket Logger.

Specification	Value	Units
Resolution	12	bits
Memory Capacity	86016	readings
Size	4.7 x 2.4 x 0.93	% FS
Max Sampling Rate	200	Hz

APPENDIX

B

METHOD OF SOBOL

This appendix presents a detailed discussion of the method of Sobol. A derivation of the sensitivity indices is presented. A quasi-random sampling strategy is discussed. Finally, the derivation of the analytical stopping distance equation of Section 4.3.2 is presented.

B.1 Sobol Method Sensitivity Indices

The derivation of Sobol's variance-based sensitivity indices can be found in [Saltelli, et al, 2000]. The input factor space for k factors is defined as a k-dimensional unit cube:

$$\Omega^k = \left(\mathbf{x} \mid 0 \le x_i \le 1; \quad i = 1, \dots, k\right). \tag{B.1}$$

The function $f(\mathbf{x})$ is decomposed into summand of increasing dimension:

$$f(x_1, \dots, x_k) = f_o + \sum_{i=1}^{k} f_i(x_i) + \sum_{1 \le i < j \le k} f_{ij}(x_i, x_j) + \cdots + f_{1,2,\dots,k}(x_1, \dots, x_k). \tag{B.2}$$

In order for this to be true, f_o must be constant, and

$$\int_0^1 f_{i_1,\dots,i_s}\left(x_{i_1}, \dots, x_{i_s}\right) dx_{i_k} = 0 \quad if \quad 1 \le k \le s \tag{B.3}$$

which says that the integral of each summand over any of its variables is zero. The consequence is that all the summand functions are orthogonal, and that

$$f_o = \int_{\Omega^k} f(\mathbf{x}) d\mathbf{x}. \tag{B.4}$$

Sobol has showed this decomposition is unique, and the terms can be evaluated with integrals. The formulas for the first and second order terms are

$$f_i\left(x_i\right)=\int_0^1\cdots\int_0^1 f\left(\mathbf{x}\right)d\mathbf{x}_{\sim i}-f_o,$$

$$f_i\left(x_i\right)=\int_0^1\cdots\int_0^1 f\left(\mathbf{x}\right)d\mathbf{x}_{\sim ij}-f_i\left(x_i\right)-f_j\left(x_j\right)-f_o.$$

where $d\mathbf{x}_{\sim i}$ denotes integration over all variables except x_i. The total variance D is defined to be

$$D=\int_{\Omega^k} f^2\left(\mathbf{x}\right)d\mathbf{x}-f_o^2 \tag{B.5}$$

while partial variances are determined from each term of the decomposition:

$$D_{i_1,\ldots,i_s}=\int_0^1\cdots\int_0^1 f_{i_1,\ldots,i_s}^2\left(x_{i_1},\ldots,x_{i_s}\right)dx_{i_1},\ldots,dx_{i_s}. \tag{B.6}$$

By squaring and integrating the decomposition over Ω^k, the partial variances are shown to sum to the total variance:

$$D=\sum_{i=1}^{k}D_i+\sum_{1\le i<j\le k}D_{ij}+\cdots+D_{1,2,\ldots,k}. \tag{B.7}$$

The sensitivity indices are defined to be the partial variance divided by the total variance:

$$S_{i_1,\ldots,i_s}=\frac{D_{i_1,\ldots,i_s}}{D}. \tag{B.8}$$

The total sensitivity indices are defined to measure the individual influence of all factors, including interaction effects between the factors. The total sensitivity for the i^{th} factor is

$$TS\left(i\right)=1-\frac{D_{\sim i}}{D}=1-S_{\sim i} \tag{B.9}$$

where $S_{\sim i}$ is the sum of all the terms $S_{i_1,\ldots,i_s}$ that do not include the index *i*. The total sensitivity does not provide a complete characterization of the system, but gives a more reliable estimate than the first-order indices.

The integrals need to compute the total sensitivity indices are estimated numerically using Monte Carlo integration. For details on Monte Carlo integration, see [Press, et al, 1992]. The computational formulae for f_o, D, and $D_{\sim i}$ are given as follows:

$$\hat{f}_o = \frac{1}{n}\sum_{m=1}^{n} f(\mathbf{x}_m) \tag{B.10}$$

$$\hat{D} = \frac{1}{n}\sum_{m=1}^{n} f(\mathbf{x}_m) - \hat{f}_o^{\,2}, \tag{B.11}$$

$$\hat{D}_{\sim i} = \frac{1}{n}\sum_{m=1}^{n} f\left(\mathbf{x}_{(\sim i)m}^{(1)}, x_{im}^{(1)}\right) f\left(\mathbf{x}_{(\sim i)m}^{(1)}, x_{im}^{(2)}\right) - \hat{f}_o^{\,2}. \tag{B.12}$$

The superscripts (1) and (2) indicate that two different data sampling matrices are being used for **x**.

The sampling strategy employed in the Monte Carlo estimation is called Quasirandom Sampling, which was first developed by Sobol [Bratley, et al, 1988]. The method generates sequences of sub-random numbers using a deterministic process. It has been shown that the Monte Carlo estimates converge at $1/n$ with this sampling technique, where n is the number of sample points used. This is much faster than the $1/\sqrt{n}$ convergence of random sampling schemes. Figure B.1 shows a comparison of quasirandom and random sequences for illustration.

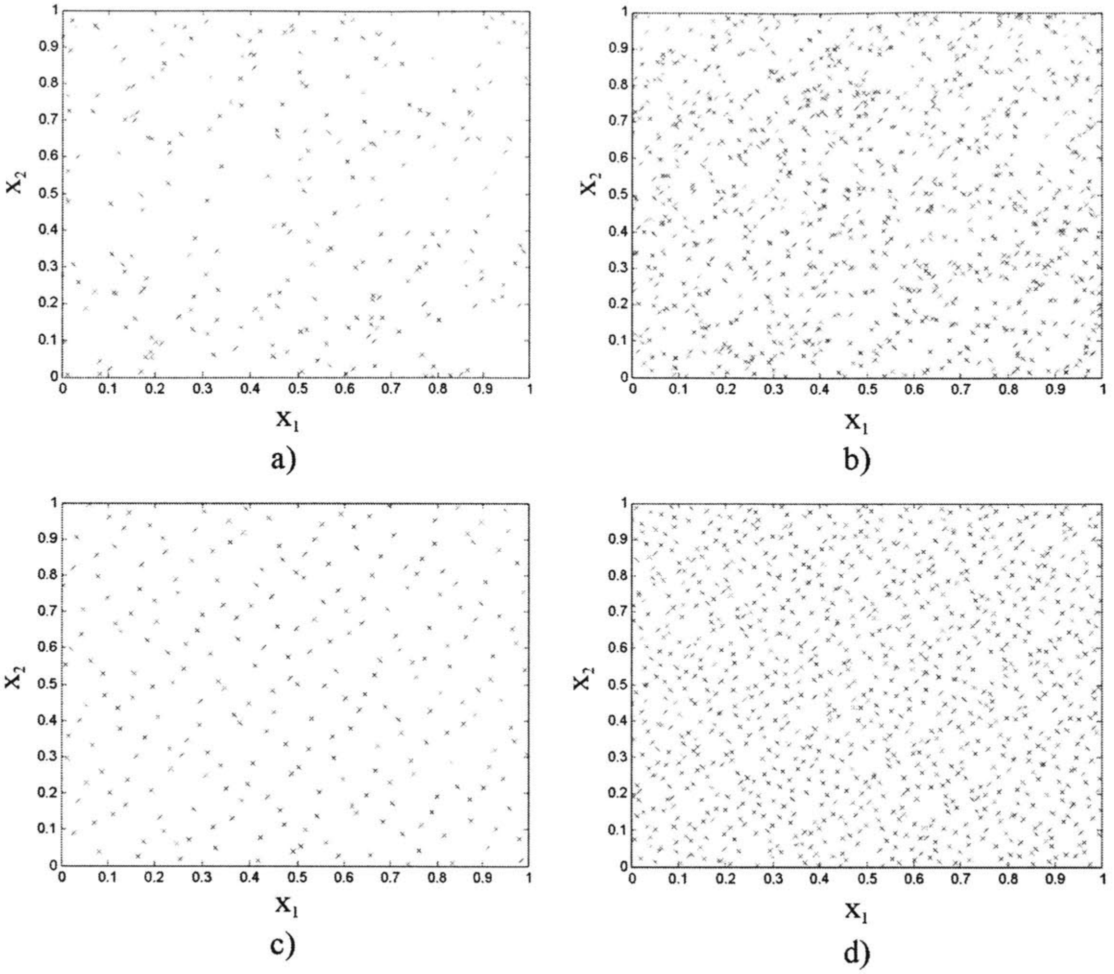

Figure B.1. A comparison of random and quasirandom sequences; a) random, n = 256; b) random, n = 1024; c) quasirandom, n=256; d) quasirandom, n=1024.

B.2 Analytical Stopping Distance

The analytical equation for stopping distance during emergency braking on flat ground as presented in 4.3.2 was derived using Lagrange's method. A free-body diagram of the dynamic model is presented in Figure B.2.

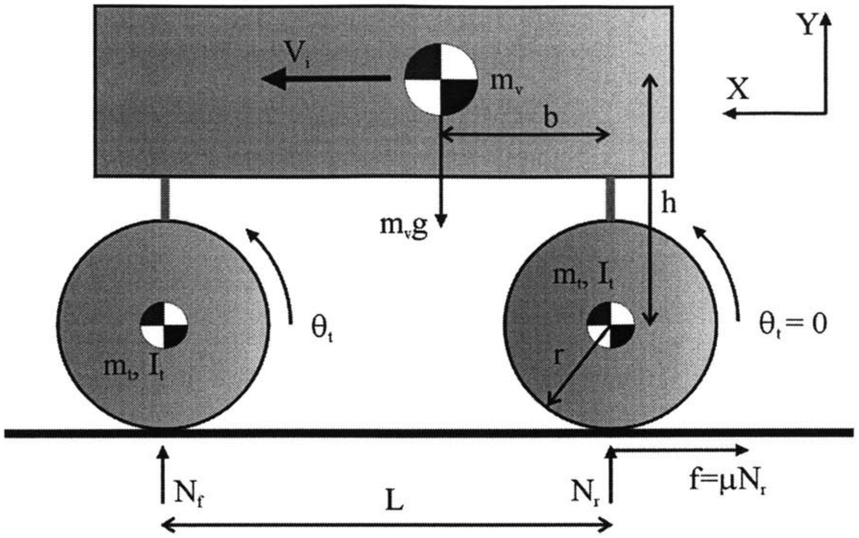

Figure B.2. Free body diagram for the analytical model of emergency braking.

The differential equation of motion was derived using Lagrange's method. The coenergy of the system is

$$T^* = \frac{1}{2}\left(m_v + 4m_t + 2\frac{I_t}{r^2}\right)\dot{x}^2 . \tag{B.13}$$

The potential energy of the system is constant, and the generalized force is

$$F = -\mu N_r . \tag{B.14}$$

The normal force on the rear tires is determined from the constraint of continuous ground contact. Summing the forces in the vertical direction, and summing the moments about the center of mass, the normal force was found to be

$$N_r = \frac{g(L-b)(m_v + 4m_t)}{L + \mu(r+h)} . \tag{B.15}$$

The equation of motion is then

$$\left(m_v + 4m_t + 2\frac{I_t}{r^2}\right)\ddot{x} = -\frac{\mu g(L-b)(m_v + 4m_t)}{L + \mu(r+h)} \tag{B.16}$$

or

$$m_{eff}\ddot{x} = -F_{eff} \tag{B.17}$$

This equation can be solved by integrating twice. The resulting solution for $x(t)$ is

$$x(t) = -\frac{1}{2}\frac{F_{eff}}{m_{eff}}t^2 + V_i t. \qquad \text{(B.18)}$$

The time to stop is found by differentiating this equation, setting the velocity to zero, and solving for the time. The stopping time is plugged back into equation (B.18) to get the stopping distance. The final simplified equation for the stopping distance is

$$x_{stop} = \frac{V_i^2\left(m_v + 4m_t + 2\frac{I_t}{r^2}\right)L + \mu(r+h)}{2\mu g(L-b)(m_v + 4m_t)}. \qquad \text{(B.19)}$$